UNIVERSITY OF OKLAHOMA

GRADUATE COLLEGE

EXPANDING IN-SITU SURFACE WATER QUALITY MONITORING TECHNIQUES FOR OPTICALLY COMPLEX INLAND WATERS UTILIZING SMALL UNOCCUPIED AERIAL SYSTEMS (SUAS)

A DISSERTATION

SUBMITTED TO THE GRADUATE FACULTY

in partial fulfillment of the requirements for the

Degree of

DOCTOR OF PHILOSOPHY

By

BRANDON K. HOLZBAUER-SCHWEITZER

Norman, Oklahoma

2021

EXPANDING IN-SITU SURFACE WATER QUALITY MONITORING TECHNIQUES FOR OPTICALLY COMPLEX INLAND WATERS UTILIZING SMALL UNOCCUPIED AERIAL SYSTEMS (SUAS)

A DISSERTATION APPROVED FOR THE

SCHOOL OF CIVIL ENGINEERING AND ENVIRONMENTAL SCIENCE

BY THE COMMITTEE CONSISTING OF

Dr. Robert Nairn, Chair

Dr. Thomas Neeson

Dr. Yang Hong

Dr. Jason Vogel

Dr. Xiangming Xiao

© Copyright by BRANDON K. HOLZBAUER-SCHWEITZER 2021

All Rights Reserved.

To those who supported me in my academic ventures, I dedicate this dissertation to you.

I would first like to thank the University of Oklahoma and my advisor, colleague, and friend Dr. Robert W. Nairn, for providing such an intensive, fulfilling, and enlightening academic experience. Doc, you are an incredible human being. I have never met someone with your work ethic, dedication to their students and craft, that also knows how to set it all aside, crack a beer and lend an ear. You shaped me as a scientist, educator, and man, and I hope someday to make a fraction of the contribution you have made. Thank you for this opportunity.

This completed dissertation would not have been possible without my wife, best friend, and lifetime companion, Heather. You reminded me to eat, sleep, and near the end, you kept me from losing what little mind I had left. I know this is not why we came to OK, but I cannot express the gratitude I have for the unwavering support you have shown me. Honestly, Heather, I do not know where I would be with you. I love you.

To my Mother, Grandma Kathy, Papa Jim, and Bomma. All of you have given me more than I could ever ask for. I am quite certain the mental, emotional, and sometimes financial assistance you have provided throughout my life has sculpted me into the student, husband, and man I am today. I am eternally grateful for each of you.

Dad, Grandpa Rich, Papa Greg, Aunt Ellie, Uncle Augie, Nana Fay, Tim, Matty, Jessie, Katie, Kate, and Eric. I know you all have been with me every step of the way. Please know I think about each of you frequently and wish you all could be here today. I miss you.

To everyone else who has been there along this decade-long journey, I made it! Thank you for continuing to check in on me, and reminding me that, yes, after ten years, I am still in school. I appreciate y'all.

Finally, I would like to thank all past and current CREW members, who, over the past six years, assisted in collecting a tremendous amount of environmental data. Without you, the information contained within this dissertation would not exist. I will be there for each of you as you have been there for me, and I look forward to seeing what our futures bring.

Table of Contents

List of Figures and Tables

Abstract

Remote sensing is described as the art and science of interpreting information (e.g., reflectance) collected from a target object (e.g., vegetation) using technology (e.g., satellites, occupied aircraft, and small unoccupied aerial systems (sUAS)) that does not need to contact the object. Remote sensing has been used to evaluate crop health (e.g., agriculture), assess land reclamation efforts (e.g., mining), and, recently to estimate surface water quality (e.g., chlorophyll-a, total suspended solids, and Secchi disk depth). By collecting information contained within the visible electromagnetic spectrum (e.g., visible reflectance), relationships (e.g., linear and nonlinear) have been developed capable of reliably estimating various water quality parameters in large optically deep (bottom substrate does not impact reflectance) waterbodies (ODWs). With the advent and continued improvement of sUAS, waterbodies otherwise too small for satellite applications are becoming more accessible. However, these smaller inland waters can be characterized as optically shallow waters (OSWs) (bottom substrate contributes to measured spectra), complicating the modeling process and accurate retrieval of water quality parameters, which are not well documented. Furthermore, because sUAS platforms, sensors, regulations, and target objects vary considerably across the literature, a desperate need exists to establish a standard operating procedure.

Therefore, the focus of this doctoral research relates to describing optically complex shallow inland waters in terms of the dependency between sUAS-derived multispectral reflectance and various in-situ water quality parameters or optically active constituents (OACs) (e.g., chlorophyll-a, total suspended solids, turbidity, Secchi disk depth, and metal concentrations). Additional examinations included addressing the site-specific nature of surface water quality models by

validating models in waters of different geologic origins. An evaluation of the impact operational parameters (e.g., flight speed) on the accuracy of sUAS-derived imagery was also completed. Thus, this dissertation's four chapters provide an in-depth understanding of light and water interactions while demonstrating the environmental applications of sUAS technology for monitoring and evaluating aquatic ecosystems.

Briefly, the results of these efforts revealed: (Chapter 2) approximately 50 percent of the variability in in-situ water quality data could be described by sUAS-derived multispectral reflectance; (Chapter 3) ordinary least squared regression models capable of predicting particulate iron, and total lithium, manganese, nickel, lead, sulfur, and zinc concentrations with moderate confidence (R^2_{adj} between 0.74 and 0.81) and low error (mean percent difference < 5.13), respectively, were developed; (Chapter 4) more accurate estimations of water quality parameters occurred in ODWs versus OSWs; and (Chapter 5) development of a standard operating procedure for environmental monitoring via sUAS must consider the variety of platforms, sensors, operational limitations and conditions, target objects, and tradeoffs identified.

Chapter 1: Introducing the Dissertation

Remote sensing is the science and art of obtaining and interpreting information about an object on the Earth's surface without physical contact. The information collected is typically reflected electromagnetic (EM) radiation (e.g., reflectance) within the visible portion (e.g., blue, green, and red) of the EM spectrum. The visible portion of the EM spectrum ranges from approximately 350 to 750 nanometers (nm) and contains all colors perceptible by the human eye. The equipment used for remote sensing studies typically consists of two main components, the platform (e.g., satellites, (un)occupied aerial, terrestrial, or aquatic vehicles) and the sensor (e.g., digital, multispectral, or hyperspectral cameras). Historically, environmental remote sensing studies used passive satellite-derived multispectral data (e.g., relies on wavelengths emitted from the sun as the energy source). Multispectral reflectance has demonstrated uses in forestry (e.g., invasive species mapping), agriculture (e.g., estimating crop productivity), and water resources (e.g., monitoring ocean surface water quality). However, with the continued advancement of remote sensing technologies, there appear to be almost countless unexplored applications.

Recently, the remote estimation of surface-water quality has become of increasing interest to environmental professionals. An ability to collect moderate-resolution (e.g., 10s of meters per pixel) satellite-derived data across large areal extents (e.g., 185 X 180 kilometers per image) has provided scientists with the opportunity to estimate water quality in large optically deep waters (ODWs) (e.g., bodies of water where the substrate and emergent aquatic vegetation do not influence measured reflectance). Unfortunately, due to considerable limitations (e.g., low spatial, spectral, and temporal resolutions, complex optical properties and bathymetry, mixed pixels, cloud cover, impractical deployment costs, and minimal research efforts), the widespread

application of traditional remote sensing technologies in optically shallow waters (OSWs) has not yet been achieved. The introduction and continued advancement of small Unoccupied Aerial System (sUAS) technologies may address some remote sensing limitations. The motivation for this research stemmed from the need to describe the advantages of sUAS technologies relative to satellite technology, develop an additional innovative tool for monitoring inland waters, improve environmental disaster response time and accuracy, and minimize the cost, labor, and time required to perform intensive field monitoring efforts to quantify the success of environmental remediation projects.

The focus of this doctoral research relates to describing OSWs in terms of the dependency between sUAS-derived multispectral reflectance and various in-situ water quality parameters or optically active constituents (OACs) (e.g., chlorophyll-a, total suspended solids, turbidity, Secchi disk depth, and metal concentrations). This dissertation aimed to develop an in-depth understanding of light and water surface interactions to demonstrate the environmental application of sUAS technology for monitoring and evaluating aquatic ecosystems negatively impacted by human activities. Thus, the overarching hypothesis of this dissertation was that applying sUAS-derived multispectral imagery collected at relatively fine temporal and spatial resolutions will improve in-situ monitoring efforts in small optically complex inland waters, will provide novel monitoring techniques for mining-impacted ecosystems, and will allow for a minute examination of the sources of remote sensing interferences (e.g., optical depth) or spectral error. The four dissertation chapters demonstrate the current effectiveness of remote sensing via sUAS in full-scale OSWs and ODWs with emphasis on estimation of novel OACs (e.g., metal concentrations) while presenting methods to identify interference or error sources with

sUAS data and an assessment of operational conditions to begin the development of a standard operating procedure. Furthermore, each chapter was developed and formatted as stand-alone papers to submit to a peer-reviewed scientific journal.

Beginning with the effectiveness of sUAS for estimating traditional OACs (e.g., chlorophyll-a) in OSWs (e.g., shallow, clear, and productive pond), Chapter 2 is presented. Chapter 2, "Using sUAS-Derived Multispectral Imagery and Linear Models as Tools for Monitoring Optically Shallow Surface Waters," illustrates how scaled-down traditional environmental remote monitoring technologies (e.g., sUAS relative to satellite) in terms of size, cost, and complexity were unable to estimate traditional water quality parameters accurately in OSWs utilizing only sUAS-derived multispectral imagery. Due to this ineffectiveness, different types of water (e.g., optically deep mine waters) and new OACs (e.g., in-situ metal concentrations) were assessed in Chapter 3. Chapter 3, "Using sUAS for the Development and Validation of Surface Water Quality Models in Optically Deep Mine Waters," demonstrates novel spectral monitoring techniques for mining-impacted surface waters utilizing spectral data from two different platforms. Results suggested sUAS could be used to describe in-situ metal concentrations in surface waters (e.g., oxidation ponds) with prominent optical properties (e.g., abundant suspended iron-oxyhydroxide solids).

Thus, to focus more on the light and water surface interactions measured via sUAS and assess the effectiveness at a different scale, Chapter 4, "In-situ Manipulations of Aquatic Optical Depth and its Effect on sUAS-Derived Spectral Reflectance," presents a controlled experiment evaluating these issues. Here mesocosm OSWs were converted to ODWs not only to demonstrate how in-situ water quality could readily be estimated in ODWs but to prove further that substrate in OSWs impacts the spectral signature measured, which could be quantified via sUAS.

Environmental scientists, monitors, and professionals rely on standard operating procedures for reliable, repeatable, accurate, and communicable results. Applying sUAS for remote environmental monitoring applications should be no different. Thus, the need for a standardized method was apparent. Chapter 5, “The Effects of Mission Parameters on the Accuracy and Efficiency of sUAS-Derived Multispectral Imagery and Operations,” establishes a baseline for such a method to be developed. This chapter emphasizes how altering mission parameters (e.g., flight speed and altitude) impacts the sUAS-derived spectra. This study revealed that efficient missions (e.g., short flight times) did not produce the most accurate spectra. More importantly, changes in solar conditions could account for approximately 60 percent of the measurement error. This study not only emphasized the need for the development of a standard method but also identified tradeoffs associated with remote sensing via sUAS.

Chapter 2: Using sUAS-Derived Multispectral Imagery and Linear Models as Tools for Monitoring of Optically Shallow Surface Waters

This chapter was submitted as a manuscript to Environmental Monitoring and Assessment.

Abstract:

Collecting high-resolution spectral data across large areal extents with small Unoccupied Aerial Systems (sUAS) provides environmental monitors with the tools to estimate water quality in large optically deep bodies of water. The purpose of this study was to illustrate how scaled-down traditional environmental remote monitoring technologies (e.g., sUAS relative to satellite) in terms of size, cost, and complexity were unable to estimate traditional water quality parameters accurately (e.g., chlorophyll-a, total suspended solids, Secchi disk depth, and turbidity), in optically shallow surface waters utilizing only sUAS-derived multispectral imagery. Linear regression analyses revealed that spectral band or band ratios could accurately describe approximately 50 percent of the water quality parameters variability yet still produce statistically significant (p-value < 0.05) results. Additionally, various reflectance extraction techniques were evaluated, and remote sensing limitations in optically shallow waters were verified. Verification of the developed models revealed low accuracy, moderate precision, and a rejection of the primary hypothesis that sUAS could describe water quality in optically shallow waters. Furthermore, a novel, simple multispectral scattering correction based on the suspended sediment's physical properties within the bulk of the waterbody was developed. Currently, sUAS technologies are far from replacing traditional in-situ environmental monitoring and should only be used as a tool to supplement typical monitoring efforts. However, as technologies continue to improve, sUAS can substantially decrease the time, money, human-hours, and laboratory analyses required to sufficiently characterize environmental problems.

Keywords:

Regression, Interpolation, Chlorophyll-a, Spectral Reflectance, Multispectral Correction

2.1 Introduction

2.1.1 Environmental Remote Sensing

The ability to collect high-resolution data across large areal extents, coupled with advancing sensor and computing technologies, equips analysts with the tools to monitor water quality in large optically deep bodies of water (e.g., bodies of waters where the substrate and emergent aquatic vegetation do not influence measured reflectance) (Doxaran et al. 2002; Williams et al. 2002; Cannizzaro and Carder 2006; Jensen 2007; Hadjimitsis and Clayton 2009; O'Neill et al. 2011; Flener 2013; Wu et al. 2014; Su and Chou 2015; Kubiak and Kotlarz 2016; Su 2017; Zeng et al. 2017; Abdelmalik 2018; Ehmann et al. 2018; Becker et al. 2019). These ecosystems have been negatively impacted via urbanization, eutrophication, sedimentation, land conversion, water withdrawal, point and non-point source pollution, and invasive species (MA 2005). Unfortunately, monitoring programs are typically field-based and are labor-, cost-, and time-intensive. Moreover, significant legal, political, and institutional obstacles can impede effective monitoring by public agencies that collect most of the data (Biber 2013). Additionally, these "spot" monitoring events rarely capture the temporal and spatial variability present in many natural phenomena, such as algae blooms.

2.1.2 Environmental Remote Sensing via sUAS

Recently small Unmanned Aerial System (sUAS) technologies have addressed some of the satellite limitations (Whitehead and Hugenholtz 2014; Su and Chou 2015; Zeng et al. 2017; Ehmann et al. 2018). The Federal Aviation Administration (FAA) defines sUAS as an unoccupied aircraft weighing less than 55 pounds on takeoff, including any payload (FAA 2016). Some features of sUAS that are attractive to the scientific community relative to traditional remote

sensing methods (e.g., satellites) include, 1) lower deployment costs; 2) ability to collect data autonomously, removing the "human" component of flight and image acquisition; 3) navigability, allowing for low-altitude flights in complex natural environments; and 4) user-defined missions, allowing the analyst to determine how frequently (temporal resolution), and at what altitude (spatial resolution) to fly sUAS missions (Whitehead and Hugenholtz 2014; Zeng et al. 2017; Becker et al. 2019).

Incorporating sUAS, however, is not a complete solution for all traditional remote sensing limitations, but can provide a significant contribution to the collection of environmental data, particularly for inland ponds, rivers, and reservoirs that are too small for satellite spatial resolutions (e.g., Landsat 7 ETM+) (Whitehead and Hugenholtz 2014; Elarab et al. 2015; Su and Chou 2015; Ehmann et al. 2018; Becker et al. 2019). Typical in-situ environmental monitoring provides information on multiple parameters at a single geographic point, and traditional remote sensing provides detailed spatial information on select parameters. Coupling sUAS technologies with spatial models can potentially provide a powerful tool for monitoring and estimating surface water quality (Dekker et al. 1996; Su 2017; Becker et al. 2019).

2.1.3 Environmental Remote Sensing in Optically Shallow Waters

Within the bulk of a water body, optically active constituents (OACs) modify the EM energy, the sum of which represents the inherent optical properties (IOPs) of the water body (Mobley 1994; Dekker et al. 1996; Jensen 2007; Palmer et al. 2015). The apparent optical properties (AOPs) (e.g., diffuse attenuation coefficient (K_d)) depend on the IOPs and the geometry of the light field (e.g., solar zenith angle) (Buiteveld et al. 1994). Considerable variability exists in the optical properties of water, which are dependent on a variety of OACs. Therefore, optical properties of natural

waters have significant spatial and temporal variations and seldom resemble the properties of "pure" water (Mobley 1994; Jensen 2007). In order to obtain information on the OACs (e.g., Chlorophyll-a (Chl-a)), colored dissolved organic matter (CDOM), or total suspended sediment (TSS)) within a water body, the water leaving radiance in the visible and near-infrared (NIR) portions of the electromagnetic (EM) spectrum is of most interest (Dekker et al. 1996; Jensen 2007; Palmer et al. 2015; Dörnhöfer and Oppelt 2016). Gordon (2005) defines water leaving radiance as the radiance (or EM energy) that is backscattered out of the water and travels to the top of the atmosphere (or multispectral (MS) sensor in this case).

In optically deep waters, the OACs and the water's surface represent the primary sources of EM radiation leaving the waterbody. However, in optically shallow waters, the backscattered EM radiation includes energy signals not only from the OACs and the water's surface, but also from radiation that has been reflected from the bottom substrate. The EM radiation reflected from the bottom of optically shallow water bodies provides information about the bottom substrate and the waterbody's bathymetry (Mouw et al. 2015; Dörnhöfer and Oppelt 2016). Several studies (Lee et al. 1998; Cannizzaro and Carder 2006; Li et al. 2017; Zeng et al. 2017) have determined how bottom reflectance in optically shallow waters affects the reflected energy signal retrieved from the water's surface. However, the fact that bottom properties (e.g., substrate composition and water depth) often vary independently from the properties of the water column, the empirically derived models developed in optically deep waters cannot be applied to optically shallow systems (Mouw et al. 2015; Arabi et al. 2020).

Despite the demonstrated effectiveness of spatial water quality models in optically deep water bodies, a literature gap exists. Many studies have reviewed the limitations associated with

collecting remote sensing data over optically shallow inland water bodies (Dekker et al. 1996; Whitehead and Hugenholtz 2014; Mouw et al. 2015; Palmer et al. 2015; Dörnhöfer and Oppelt 2016; Hardin et al. 2018; Kislik et al. 2018; Wu et al. 2019), yet few describe the processes, successes, or lack thereof when attempting to estimate surface water quality in optically shallow waters utilizing sUAS-derived MS imagery. Studies that have successfully developed predictive water quality models (Lee et al. 1998; Cannizzaro and Carder 2006; Volpe et al. 2011) are limited in application due to the tremendous amounts of input data required (e.g., hyperspectral (HS) measurements, bathymetric maps, empirical absorption coefficients, backscattering estimates, and extensive calibration and validation) and site-specificity (Arabi et al. 2020). Therefore, the purpose of this paper is to illustrate how scaled-down traditional environmental remote monitoring technologies (e.g., sUAS-derived MS reflectance) was unable to accurately describe various in-situ OACs (e.g., Chl-a, TSS, Secchi Disk Depth (SDD) and turbidity) in an optically shallow body of water. The experimental hypothesis evaluated was coupling various bands or band transformations from sUAS-derived multispectral imagery and in-situ surface water quality data will allow for the development of statistical models capable of predicting (e.g., within the 75 percent confidence interval) concentrations of traditional OACs (e.g., Chl-a, turbidity, TSS, and SDD) in optically shallow surface waters.

2.2 Materials and Methods

2.2.1 Study Site Background

The abandoned Tri-State Mining District (TSMD) (Figure 2.1A) includes approximately 6500 km^2 within southeastern Kansas, southwestern Missouri, and northeastern Oklahoma, where underground mining for lead and zinc ores took place from the mid-1800s to the late 1960s.

Within the Oklahoma portion of the TSMD is the Tar Creek Superfund Site, which became a concern when artesian waters began to flow through abandoned mine shafts and boreholes in 1979. Substantial degradation of receiving waters occurred due to elevated ecotoxic metals concentrations in artesian flowing discharges and runoff/leachate from waste materials left on the surface. In 1980, the Tar Creek Task Force was established to investigate the impacts of mine drainage on the local water resources. As a result of the findings, the Tar Creek Superfund Site was added to the National Priorities List (NLP) on September 8, 1983.

This study took place at the Mayer Ranch Passive Treatment System (MRPTS) within the Tar Creek Superfund Site. MRPTS is a ten-cell passive treatment system operated in two parallel treatment trains (Figure 2.1B) designed to promote natural biogeochemical processes to improve water quality from artesian mine discharges in specific process units (Nairn et al. 2010). After retention of elevated iron, zinc, lead, cadmium, arsenic, and other contaminant concentrations, in all other units, the final process unit is a polishing pond (Cell 6 (C6)). C6 serves as an ecological buffer between treated mine drainage and the receiving stream while promoting further settling of solids and photosynthetic oxygenation (Nairn et al. 2010). Although part of a mine drainage PTS, at this point in treatment, ecotoxic metal concentrations are negligible. However, elevated levels of calcium, magnesium, sulfate, and alkalinity similar to the artesian source waters were present (Nairn et al. 2010). This unit (e.g., C6) was selected for study because of its proximity to other historical field locations, and the optical properties of the water body were yet to be studied.

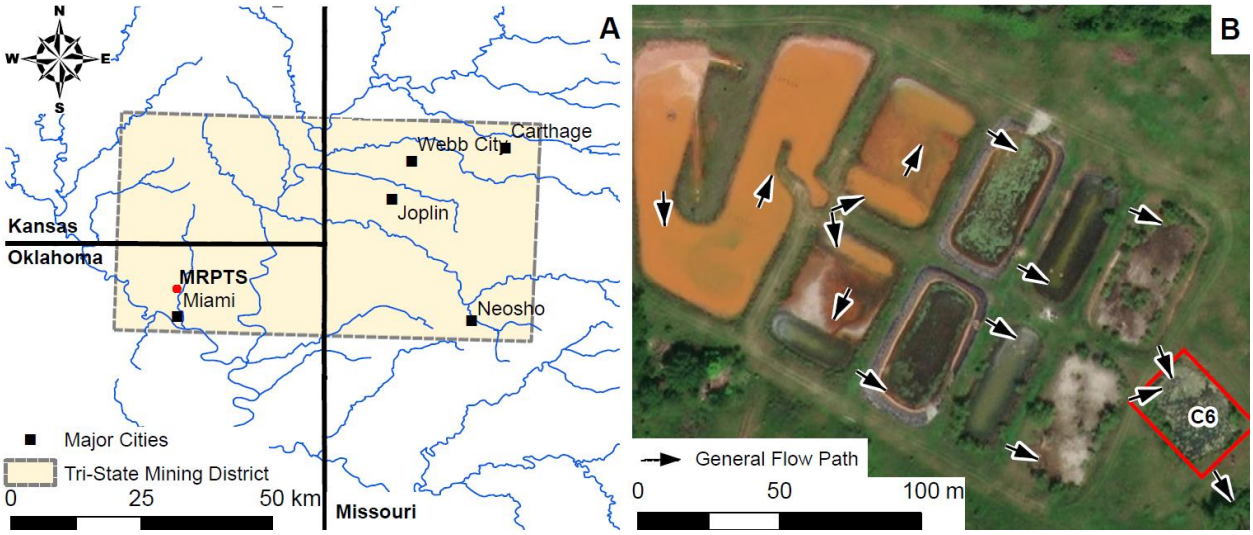

Figure 2.1 Generalized extent of TSMD within Oklahoma, Kansas, and Missouri; red dot represents the location of MRPTS (A); MRPTS displaying all ten process units, highlighting study pond (e.g., C6) with red box; white and black arrows represent the generalized flow path through the system (B).

2.2.2 sUAS Configuration

An Aerial Technologies International (ATI) AgBot, paired with the MicaSense RedEdge MS sensor, was used in this study. The AgBot is a 5-kilogram, vertical take-off, and landing, dual battery sUAS, capable of flying for over 25 minutes at speeds of approximately 18 m s^{-1}. The MicaSense RedEdge sensor simultaneously captures five discrete EM bands, with center points in the blue band (475 nm), green band (560 nm), red band (668 nm), rededge band (717 nm), and NIR band (840 nm). Additionally, the RedEdge sensor lens has a 5.5-millimeter (mm) focal length that produces uncompressed 16-bit, 1,280 X 960-pixel, TIFF format, raw digital number (DN) MS imagery. This sensor can produce extremely fine spatial resolutions (e.g., cm per pixel), making the data ideal for examining minute changes in spectral reflectance. The sUAS was equipped with a two-axis gimbal that adjusts the sensor to collect imagery at nadir (e.g., directly below the sensor) to ensure proper sensor orientation during flight. Collecting MS imagery over water bodies with

respect to nadir minimizes geometric distortions and impacts of sun glint, creating an image that is more consistent in terms of scale and illumination conditions (Green et al. 2017).

2.2.3 Mission Planning and Flight Control

Throughout the study, MS imagery was collected utilizing the ATI AgBot's capability of flying autonomously. Autonomy removed the human aspect of flight and allowed for the same mission to be repeated multiple times. Flight plans were developed using Mission Planner V1.3.37 (ArduPilot 2020) before entering the field, with the option of altering the mission while in the field (Figure 2.2). Typical mission parameters used for MS data collection included a flight speed of approximately 6 m s^{-1}, an altitude of approximately 50 m AGL, a nadir viewing angle, with at least 75 percent side and overlap to ensure proper image mosaicking and high-quality data. When these parameters were used, the spatial resolution of each pixel was approximately 6.82 cm.

Throughout the mission, the pilot-in-command (PIC) maintained visual contact of the sUAS and monitored air traffic frequencies. The PIC was prepared to abandon the mission should any risk be observed (e.g., increased wind speeds or occupied aircraft enters airspace). For further risk avoidance, a visual observer maintained consistent visual contact. Finally, monitoring the ground control station identified any issues with the sUAS's inertial navigation system (INS), global positioning system (GPS), or autopilot.

Figure 2.2 Example sUAS flight path (yellow lines) used for MS image collection, with waypoints (green numbered markers), and the mission extent (red polygon).

2.2.4 Multispectral Image Processing

Typical sUAS missions at MRPTS required approximately 690 individual images (138 sets of images per band) to cover the developed field (Figure 2.2). The raw DN 16-bit TIFF images were stitched together to create a mosaic of the study site. Post-processing was completed using the manufacturer-recommended Atlas Image Processing Software. Raw MS imagery was uploaded to the cloud-based image processing software, and approximately one day later, the products were available for download. Limited by the software's proprietary nature, once uploaded, the imagery was orthorectified, mosaicked, and radiometrically corrected using a calibrated reflectance panel. This “black-box” processing did not allow for customization in terms of digital image processing. However, the simplicity, reliability, and repeatability of the products provided were desirable for this study. Products available for download from the software included:

reflectance as DNs, a digital surface model (DSM), and a Normalized Difference Vegetation Index (NDVI) layer. Once downloaded, the reflectance surfaces were converted from DNs to percent spectral reflectance by multiplying each pixel in the surface by a factor of (1/32768) (MicaSense 2019). The reflectance values were scaled by a factor of 32,768, allowing the data to be stored in a 16-bit format.

2.2.5 Multispectral Reflectance Extractions

Reflectance values were extracted from the pixel that corresponded to the in-situ sampling location (e.g., pixel-by-pixel), similar to the technique demonstrated by Su (2017). For further analysis and to manage imperfect pixels, water fluidity, and GPS offset, a buffer-by-buffer extraction was performed, much like a study completed by Su and Chou (2015), who created a 1-m buffer around the in-situ sampling location. The mean and median reflectance values were extracted and examined for relationships with measured water quality parameters. Finally, to resemble traditional monitoring efforts, where water quality parameters are measured at a single location and applied to the entire water body, a composite buffer extraction was completed. For this technique, all the reflectance values within the 1-m buffers were compiled and extracted as mean values for each of the five bands (e.g., blue, green, red, rededge, and NIR). In other words, for all the buffers created in the previous analysis, the means were extracted so that each sUAS mission had a single reflectance value for each band that was applied to the entire pond.

2.2.6 Simple Multispectral Scatter Correction

Attempts were made to address scattering caused by suspended particles (e.g., TSS) within the bulk of the waterbody. A novel, simple multispectral scattering correction (SMSC) was developed.

Reasons to develop this metric included, (1) no literature could be cited that addressed adjusting sUAS-derived MS reflectance for such phenomena (Nansen 2018), (2) the purposefully streamlined methodology did not include all of the variables in the radiative transfer model, and (3) more traditional environmental data was incorporated into the historically complex optical models used to describe surface water quality. The development of the SMSC was based on theories from multiple disciplines of science, which were simplified and modified for this application (Wentworth 1922; Kanick et al. 2012; Platt and Collins 2015). Several assumptions were required to develop this metric including, (1) particle sizes, (2) particle shapes, (3) a simplified EM energy scatter theory based on wavelength, and (4) scattering efficiency of the suspended material, which was based on the assumed cross-sectional area of the particles.

2.2.7 In-situ Surface Water Sampling

Ten in-situ grab surface-water-quality samples were collected from C6 at MRPTS across ten individual sUAS missions in the summer of 2018 (June – August) (e.g., 100 in-situ samples total) (Figure 2.3). Samples were collected from the shoreline with a 3.6-m swing-arm sampling pole within the bulk (e.g., middle) of the water column. By collecting a sample from the middle of the "detectable" water column, the water gathered should have been more representative of the spectral signature measured. The idea was that the MS sensor would not detect any spectral signature from materials below the sampling location if the pond's bottom substrate were not visible. To assess substrate visibility and minimize benthic material resuspension, SDD was measured from the shoreline with the same sampling pole after completing the sUAS missions. Another important sampling parameter typically referred to as the time window is the time from the end of the sUAS mission to completing the in-situ sampling event. The larger the time

window, the higher chance that the relationships could be negatively impacted due to temporal variations in water quality and changes to the solar zenith angle (Olmanson et al. 2013; Wu et al. 2014; Bonansea et al. 2015; Kubiak and Kotlarz 2016; Su 2017). The time windows maintained for this study never exceeded 75 minutes. Additional laboratory water quality analyses were completed following EPA-approved methods (Table 2.1), except for the Chl-a extraction procedure adapted from Chen et al. (2006) utilizing a hot ethanol extraction technique.

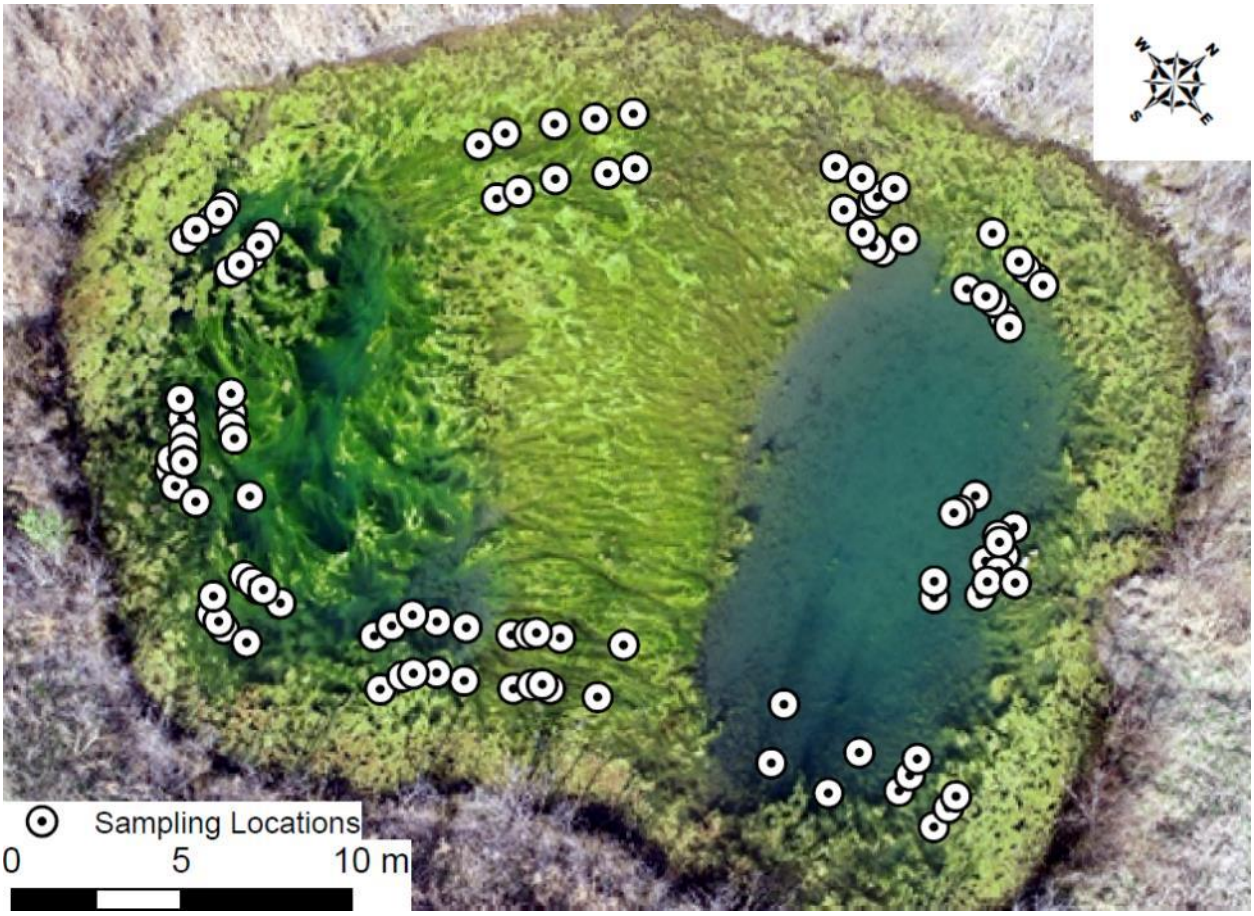

Figure 2.3 Study pond (e.g., C6) displaying clustered sampling locations (e.g., ten), each cluster corresponds to a shoreline location where samples were collected once per mission for a total of ten missions throughout the sampling period.

Table 2.1 Water quality analytical methods utilized in this study.

Water Quality Parameter	Analytical Method
Chl-a	Chen et al. 2006
TSS	EPA 160.2 (1999)
Turbidity	EPA 180.1 (1993)

2.2.8 Descriptive Statistics, Statistical Analyses, and Data Transformations

Data distributions were examined with the Kolmogorov-Smirnov Test and various theoretical distributions (e.g., normal). Accepting the null hypothesis (p-value > 0.05) indicates the experimental data was not significantly different from the reference distribution. Evaluation of the F-test statistic provided insight as to whether the explanatory variables contributed to the developed models. Rejecting the null hypothesis (p-value < 0.05) of this test suggests the added variables improved the model's fit relative to an intercept-only model (e.g., regression coefficients equal zero). Further efforts examined the multicollinearity, tolerance, and variance inflation factor (VIF) among the independent variables. The presence of multicollinearity can cause several issues related to regression, mainly when tolerance is below 0.2 and the reciprocal (e.g., VIF) is ten or greater (Miles 2005). Outliers were identified and removed using the interquartile range (IQR) of each variable. All descriptive statistical analyses were completed using various R statistical software packages and the Real Statistics Resource Package in Microsoft Excel. Before any regression testing, the larger dataset was randomly split into calibration and verification datasets.

Single variable (e.g., band or band ratio) Geographically Weighted Regression (GWR), a form of local linear regression, was employed to examine the relationship, if any, between in-situ MS reflectance and water quality parameters. GWR was pursued because it can model the spatial

variation of natural relationships. Additionally, various data transformation techniques (e.g., logarithmic and exponential) were explored and applied to every extraction procedure. The developed models were then evaluated in terms of the strength of the relationship between the variables (e.g., correlation coefficient (R)), the independent variable's ability to explain variance in the dependent variable (e.g., $R^2_{adj.}$), and the significance of the independent variable(s). Calibration models were verified with the randomly selected verification dataset that was not significantly different (p-value > 0.05) than the calibration dataset. The randomly divided verification dataset was used as the input to the selected calibration models. Examination of the verified models occurred in terms of residual sum of squares (RSS), Akaike Information Criterion corrected for small sample sizes (AICc), bias, and root-mean-square error (RMSE).

Unfortunately, developing the composite buffer dataset and models required an agglomeration of the buffer-by-buffer datasets. Therefore, no model verification could be completed with this dataset. Instead, a novel scattering correction technique was applied, and the models were reevaluated to determine its effects. To further demonstrate the utility of remote monitoring for optically shallow waters, a series of surface water quality maps were generated using a second-order Local Polynomial Interpolation (LPI).

2.3 Results and Discussion

The spectral data collected in this study were subjected to variable environmental conditions. Examination of the raw pixel-by-pixel reflectance dataset distribution revealed an arcsine distribution to be the best fit (p-value = 1.00). However, this fit was unrealistic, so the dataset was examined for outliers. The results of this analysis suggested that several samples be removed from the raw pixel-by-pixel dataset. Therefore, the dataset then had a remaining sample number

(n) of 99, 71, and 51 for reflectance and Chl-a, turbidity and SDD, and TSS, respectively. Summary statistics for these data are presented in Table 2.2.

Further analysis of the "cleaned" dataset revealed a positively skewed logistic distribution fit all reflectance bands (Figure 2.4) (p-value > 0.05), except the red band. The red band did not follow this distribution due to fundamental EM interactions with water. Water preferentially absorbs longer wavelengths of light (e.g., red). Sixty-three percent of the measured reflectance in the red band below the mean caused an unequal distribution in the tails of the dataset. Outliers were not considered for any extraction technique except pixel-by-pixel because the extraction techniques were used to minimize variability (e.g., water fluidity, sun-glint, and imperfect pixels) in the datasets (Figure 2.5).

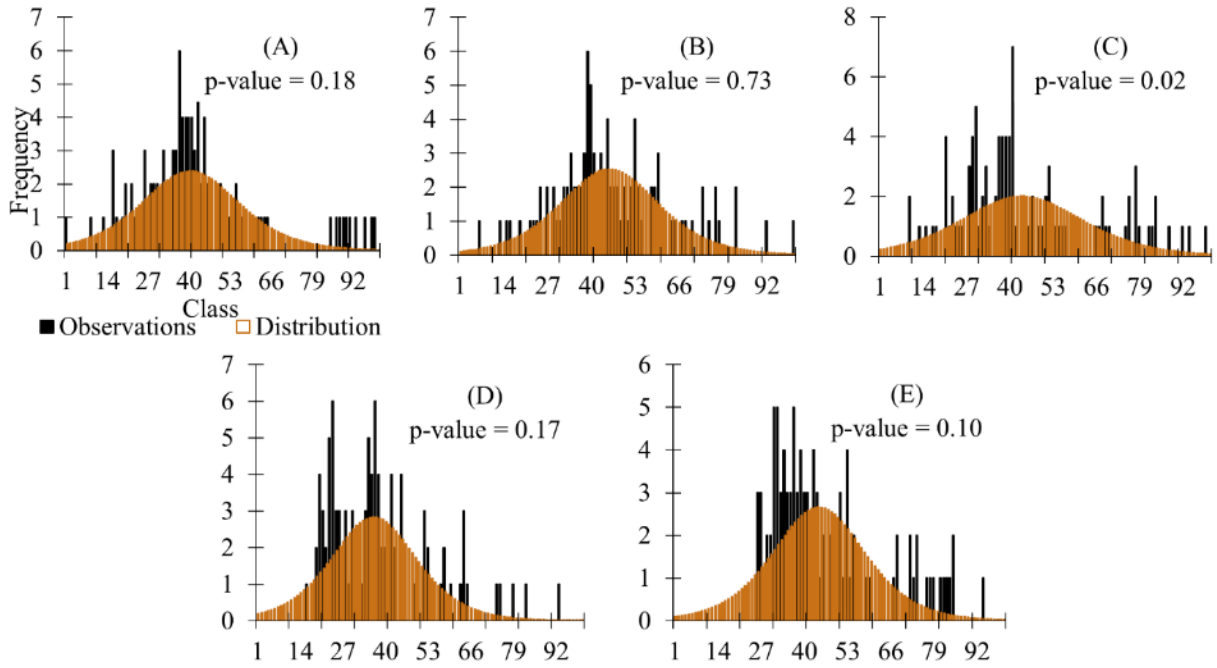

Figure 2.4 Observed MS distribution (black bars) versus theoretical logistic distribution (orange bars) for (A) blue band, (B) green band, (C) red band, (D) rededge band, and (E) NIR band; all plots have the same axes and legend as plot (A); p-values were results from Kolmogorov-Smirnov Test.

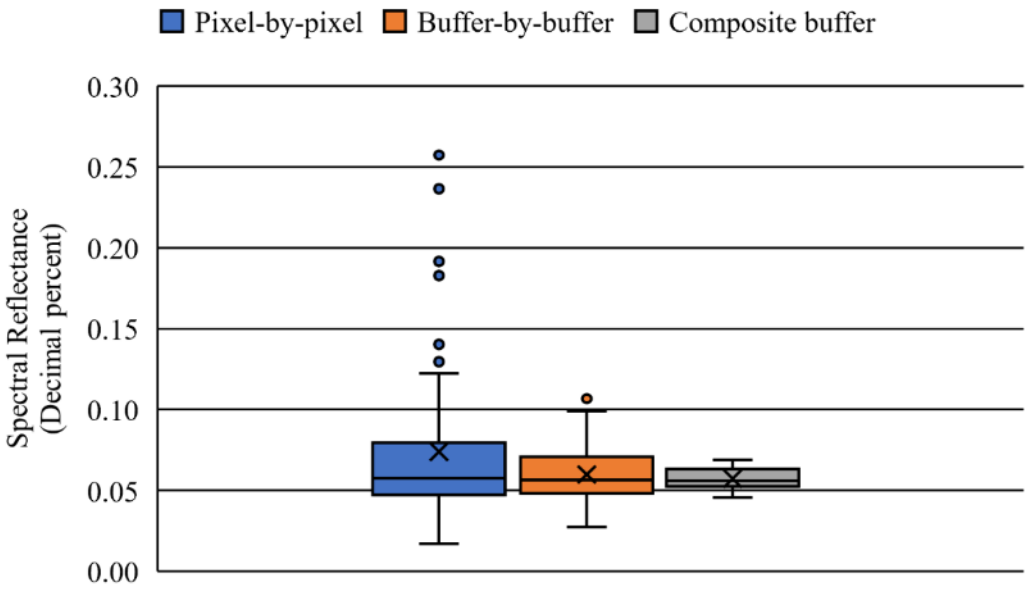

Figure 2.5 Box and whisker plots for selected MS band (green); filled circles above the third quartile represent outliers present in the datasets; the median is represented with a horizontal line and the mean is the "x" within the box.

Table 2.2 Selected descriptive statistics for MS reflectance bands (decimal percent) and in-situ water quality parameters (units listed) with turbidity symbolized as (Turb).

Parameter	Blue	Green	Red	RedEdge	NIR	Chl-a ($\mu g\ L^{-1}$)	Turb (NTU)	SDD (m)	TSS ($mg\ L^{-1}$)
n	99	99	99	99	99	99	71	71	51
Mean	0.037	0.058	0.043	0.052	0.068	5.55	8.94	0.77	4.48
Median	0.035	0.055	0.039	0.049	0.059	4.46	7.99	1.00	3.25
Minimum	0.011	0.017	0.017	0.022	0.037	0.36	3.61	0.35	0.50
Maximum	0.072	0.114	0.084	0.128	0.137	20.20	17.67	1.25	14.38
Variance	1.63E-4	3.28E-4	2.40E-4	4.69E-4	6.13E-4	18.18	13.00	0.10	11.73
Standard Deviation	0.013	0.018	0.015	0.022	0.025	4.26	3.61	0.32	3.43

2.3.1 Multispectral Reflectance

The collection of reflectance data over this optically shallow inland water body was subjected to interferences from water transparency and depth (e.g., optically shallow waterbody), type and morphology of benthic substrate, presence of and scattering caused by OACs, and the typical

algal phenotype (e.g., filamentous versus colonial). Independent variables (e.g., reflectance bands) also exhibited multicollinearity with a mean R^2 of 0.89, a tolerance of 0.11, and a variance inflation factor (VIF) of 9.27. Correlations among the independent variables and the optical heterogeneity made the development of predictive statistical models complex, specifically in developing linear regression models and assessing the significance of the independent variable's ability to explain the dependent variable's variance. Additionally, when evaluating regression models, strong autocorrelation between reflectance bands existed. The presence of collinearity and autocorrelation between independent variables, along with the weakness of the relationships, suggests that additional explanatory variable(s) (e.g., bottom albedo and bathymetry, hyperspectral reflectance, and other empirically derived IOPs) would assist in developing descriptive statistical models.

2.3.2 In-Situ Water Quality

Throughout the study period, the observed mean Chl-a concentrations within C6 were representative of a mesotrophic trophic classification (e.g., 2.5 – 8 μg Chl-a L^{-1}) (OECD 1982). Further examination of water quality on an individual mission basis supported this trophic classification. Therefore, a trophic status-based statistical analysis, with demonstrated effectiveness, could not be completed (Arango and Nairn 2020). In theory, the variability (Table 2.2) of in-situ OAC concentrations across the study period should have assisted in model development by providing a more comprehensive range of reflectance and concentrations to the model. However, due to the nature of the algae (e.g., benthic and planktonic filamentous algae) (Figure 2.3) and the inherent spatial heterogeneity of C6 (e.g., presence of aquatic vegetation, physical depth, and water clarity), this was not the case. The relatively low TSS values suggest the

substrate was not disturbed during sampling; however, TSS outliers were present in the dataset. The outliers that were removed via IQR contained considerable amounts of algae, of which the large masses were selectively removed before filtration. However, substantial quantities of floating filamentous algae persisted, contributing to the overall TSS concentration. This phenomenon was not translated to the in-situ determination of turbidity because the measurements were completed with water removed from the water body (e.g., transferred to a 10 mL sample cell). Grayson et al. (1996) mention turbidity values are dependent on the properties of the suspended material (e.g., heterogeneous filamentous algae and suspended sediment) and characteristics of the turbidity instrument. As suspended particles within a solution increase in size, the symmetrical distribution of scattered light concentrates in a forward direction relative to the incident source (Sadar 1998). Overall, the in-situ water quality measured throughout the study period was representative of an optically shallow mesotrophic mid-latitude lacustrine ecosystem.

2.3.3 Development and Calibration of Linear Models

When examining the linear relationships between untransformed spectral reflectance and in-situ water quality data, no correlations were observed (R = -0.14 to 0.13). Several data transformation techniques were applied to examine the observed relationships. The transformation techniques enhanced the relationships between some of the variables while also modifying the directionality of some of the relationships. Like nearly all remote sensing water quality studies, no one data transformation, band, or band ratio could describe the entire water quality dataset (Cheng et al. 2013). Overall, 80 single variable (e.g., band or band ratio) models were evaluated for each extraction technique (e.g., pixel-by-pixel, mean and median buffer-by-buffer, and composite

buffer) for a total of 320 models. From these models, a subset of the most predictive (e.g., highest $R^2_{adj.}$) for each water quality parameter and extraction technique was selected for model verification (Table 2.3). All the selected models displayed a significantly (p-value < 0.05) better fit than an intercept-only model. Therefore, the null hypothesis of the F-test was rejected, and the alternative hypothesis was accepted. However, the $R^2_{adj.}$ values reported in Table 2.3 reflect low to moderate predictability, with only seven of the twelve selected models capable of describing over 50 percent of the OAC variability.

Generally, the statistical relationships between in-situ water quality and spectral reflectance improved with larger extraction areas. However, unlike other studies, a single type of extraction technique did not produce the most robust relationships for all water quality parameters (Arango and Nairn 2020). For the extraction techniques applied in this study, each produced at least one model with the highest $R^2_{adj.}$ value for at least one of the water quality parameters. Chl-a and TSS, turbidity, and SDD could most readily be estimated with the composite buffer, mean buffer-by-buffer, and pixel-by-pixel extraction technique, respectively (Table 2.3).

Furthermore, for each extraction technique, the band or band ratio producing the most robust (e.g., highest $R^2_{adj.}$) relationship for each water quality parameter was different. For some parameters (e.g., TSS), the band ratio was composed of one similar band (e.g., NIR) across extraction methods. In other cases, the water quality parameter (e.g., turbidity) did not consistently exhibit strong relationships with any single band or band ratio (Cheng et al. 2013).

Table 2.3 Dependent (Y) and independent (X) variables and adjusted coefficient of determination (R2adj.) for linear models grouped by extraction technique. All models were significant at p-value < 0.05 when evaluated with the F-test statistic.

Analyte (Y)	Pixel-by-Pixel		Buffer-by-Buffer		Composite Buffer	
	Band(s) (X)	$R^2_{adj.}$	Band(s) (X)	$R^2_{adj.}$	Band(s) (X)	$R^2_{adj.}$
Chl-a	Blue:Rededge	0.34	Rededge	0.29	Blue:NIR	0.54
TSS	NIR:Green	0.15	NIR:Blue	0.53	NIR:Rededge	0.89
Turbidity	Red	0.28	NIR:Blue	0.59	Rededge:NIR	0.52
SDD	Rededge	0.60	Green:Red	0.15	Red:Blue	0.54

Additionally, attempts were made to evaluate indices that had already been developed and cited in the literature. One index evaluated for Chl-a was the Normalized Difference Chlorophyll Index (NDCI) which used reflectance from the green (560 nm) and rededge (710 nm) bands to estimate Chl-a concentrations in surface waters (Watanabe et al. 2018). A similar index was tested to evaluate turbidity (e.g., Normalized Difference Turbidity Index (NDTI)) in surface waters using the red (660 nm) and green (560 nm) bands (Lacaux et al. 2007). These models, developed using satellite-derived MS imagery, produced weak statistical relationships ($-0.33 > R < 0.28$) when employed in optically shallow waters with sUAS-derived MS imagery collected at similar band center points. The rededge band can be strongly correlated with in-situ Chl-a concentrations in surface waters (Ha et al. 2017). This band has also been shown to be an optimal Chl-a estimator ($R^2 = 0.92$) in turbid waters when used in various combinations (e.g., band ratio or indices) (Cheng et al. 2013). The weaker relationships observed relative to Cheng et al. (2013) and other studies resulted from several factors. The first is related to the sensor's spectral resolution (e.g., MS versus HS). Additionally, the ability to visually observe submerged vegetation and bottom substrate likely caused a shift in rededge peak reflectance by approximately 20 nm (Turpie 2013) and increased overall reflectance within the visible spectrum by roughly 20 percent (Zeng et al.

2017). Overall, the most useful band ratio to estimate in-situ water quality parameters, specifically Chl-a, TSS, and turbidity, included the NIR band. Work completed by Gurlin et al. (2011), who found that NIR:Red ratio models could accurately estimate Chl-a concentrations in turbid waters with a mean absolute error of 1.2 mg m^{-3}, supported these observations. Additionally, Su (2017) stated that a positive relationship should exist between NIR:Blue ratio and turbidity. The results of this study support this statement, where a strong positive relationship (R = 0.77) between turbidity and the NIR:Blue ratio was observed.

2.3.4 Verification of Linear Models

Table 2.4 outlines pixel-by-pixel GWR outputs for each water quality parameter. The predictability of the calibrated and verified models (Tables 2.3 and 2.4, respectively) was similar in magnitude but varied depending on the water quality parameter. Based on the R^2 values of the calibrated models, it is unlikely any overfitting was carried through to the verification stage. Although the observed relationships were weak, the calibration and verification datasets were not statistically different, suggesting the reported models were representative of the datasets. Even though the reported models' predictability was low, the independent variables significantly contributed to the models' overall success. This significant contribution was a promising result and consistent with current literature (Su and Chou 2015; Avdan et al. 2019; Wu et al. 2019). To demonstrate the application for remote environmental monitoring with sUAS in a series of surface water quality maps were generated using LPI (Figures 2.6 – 2.9).

Table 2.4 Evaluation metrics for verified pixel-by-pixel models; RMSE = Root Mean Square Error RSS = Residual Sum of Squares; AICc = Akaike Information Criterion corrected.

Analyte	$R^2_{adj.}$	RMSE	Bias	RSS	Sigma	AICc
Chl-a	0.30	1.86 µg L^{-1}	1.05 µg L^{-1}	0.50	0.26	7.98
TSS	0.02	3.90 mg L^{-1}	-0.15 mg L^{-1}	12.55	3.90	133.04
Turbidity	0.57	1.42 NTU	1.08 NTU	1.38	0.13	-39.78
SDD	0.21	1.53 m	0.95 m	0.53	0.18	-16.96

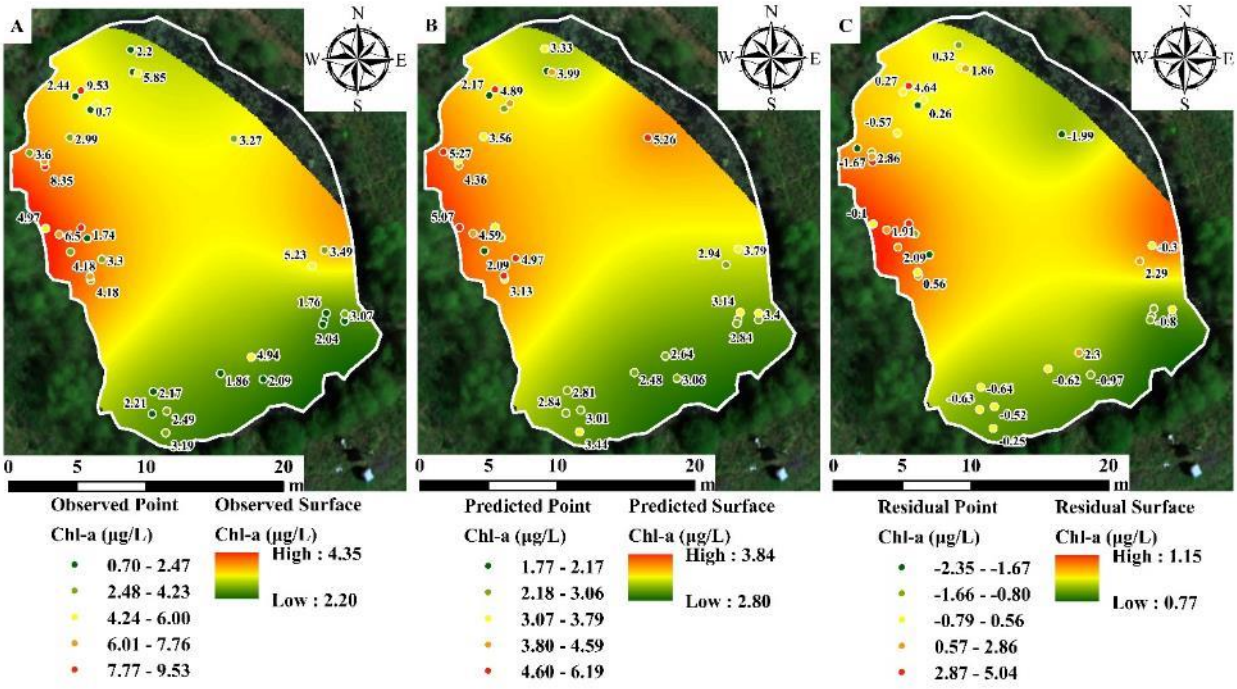

Figure 2.6 Observed (A) and Geographically Weighted Regression (GWR) predicted (B) Chlorophyll-a (Chl-a) concentration (µg L^{-1}) surface maps with resulting residual surface (C); verification point data are labeled, and all surfaces were extrapolated with Local Polynomial Interpolation.

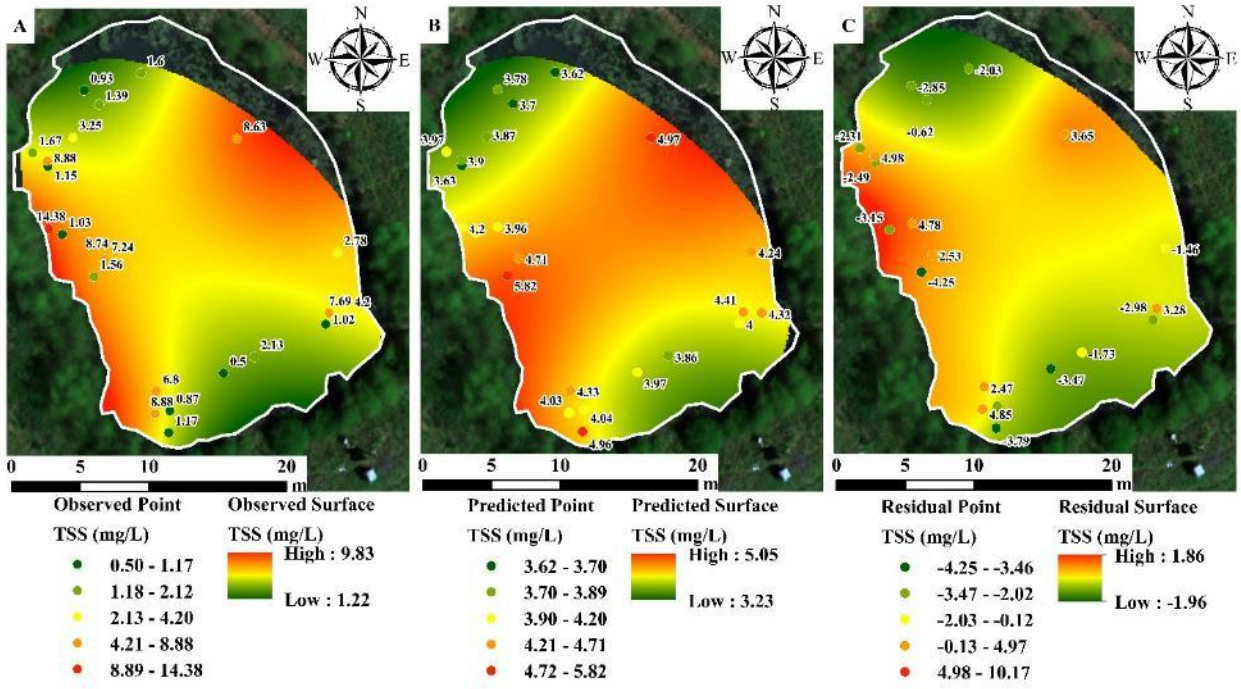

Figure 2.7 Observed (A) and Geographically Weighted Regression (GWR) predicted (B) Total Suspended Solids (TSS) concentration (mg L^{-1}) surface maps with resulting residual surface (C); verification point data are labeled, and all surfaces were extrapolated with Local Polynomial Interpolation.

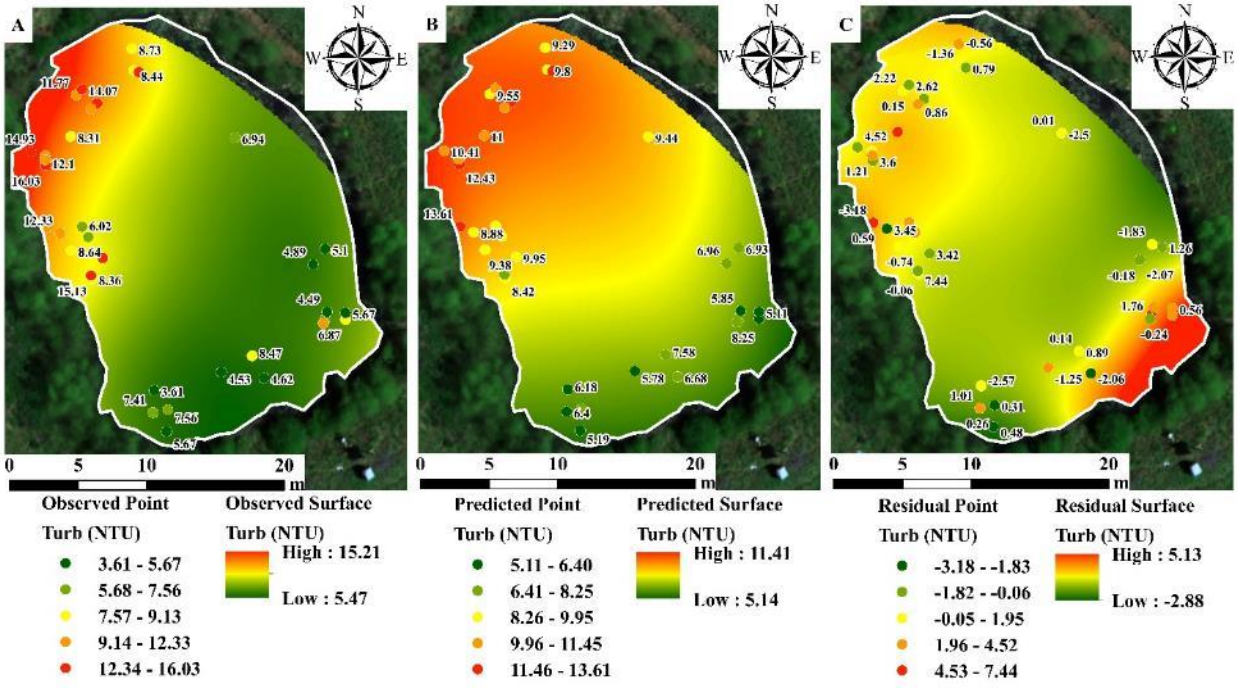

Figure 2.8 Observed (A) and Geographically Weighted Regression (GWR) predicted (B) Turbidity (Turb) (NTU) surface maps with resulting residual surface (C); verification point data are labeled and, all surfaces were extrapolated with Local Polynomial Interpolation.

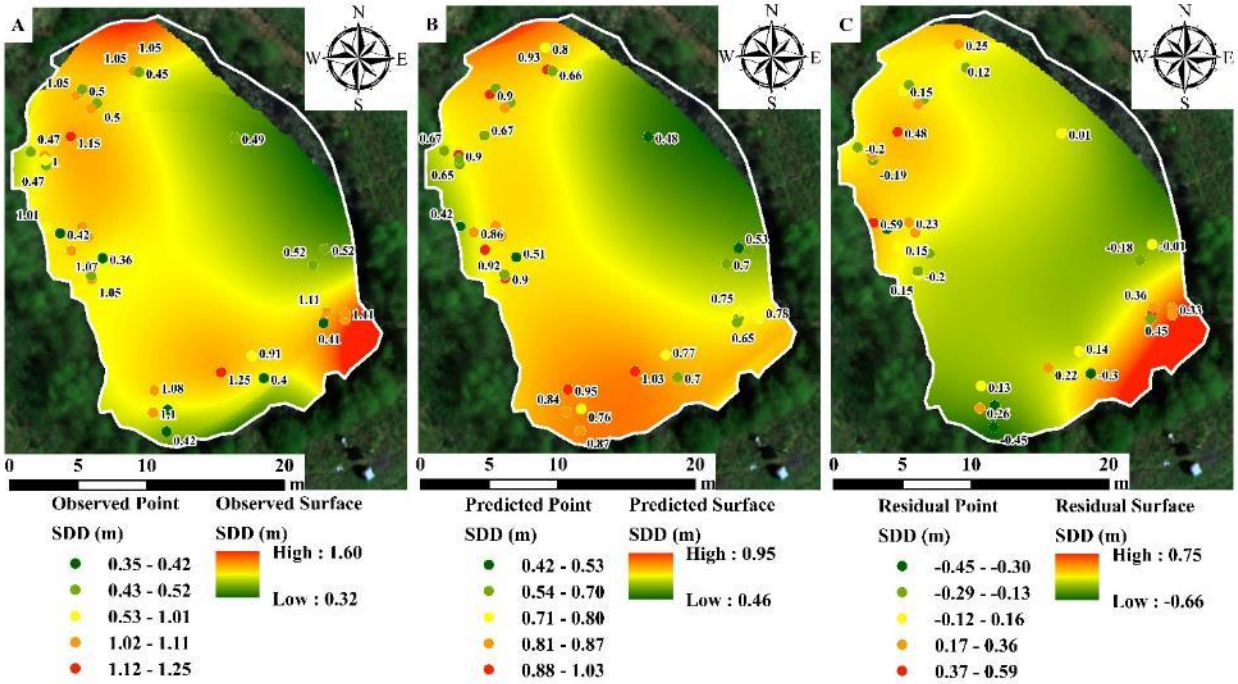

Figure 2.9 Observed (A) and Geographically Weighted Regression (GWR) predicted (B) Secchi Disk Depth (SDD) (m) surface maps with resulting residual surface (C); verification point data are labeled and, all surfaces were extrapolated with Local Polynomial Interpolation.

Given the heterogeneity of dataset and waterbody, most regression evaluation metrics (e.g., RMSE, bias, and RSS) appear to be acceptable (Table 2.4). However, the model's predictiveness ($R^2_{adj.}$) does not match the metrics evaluated, nor did these values fall within the 75 percent confidence interval. This low p-value, low R^2 phenomenon indicates that high variability datasets can still have a significant trend, and the independent variables evaluated could describe 2 – 57 percent of that variability. These results were not ideal and resulted in rejecting the primary hypothesis of this study. However, a significant statistical relationship was observed between the predictors and response variables. The significant relationship observed paired with the relatively low RMSE and bias support using sUAS technologies as a preliminary monitoring tool for optically shallow surface waters. If the reported models were applied, they would have low accuracy levels

but would be relatively precise. Including additional (e.g., HS reflectance - Becker et al. (2019)) and different data (e.g., bottom reflectance – Cannizzaro and Carder (2006)), utilizing alternative validation (e.g., k-fold cross-validation –Zeng et al. (2017)) and new reflectance extraction techniques, or evaluating other modeling options (e.g., spatial autocorrelation – Guimarães et al. (2017)) would likely improve the developed model's ability to estimate concentrations of OACs in optically shallow surface waters.

2.3.5 Simple Multispectral Scattering Correction

Overall, applying the SMSC to the composite reflectance extractions produced significantly different datasets (p-values < 0.001). The SMSC simulated the process of scattering, in that the energy was removed from EM radiation and reemitted in a different direction, phase, or wavelength (Scott 2014). However inexact this correction might be, it provides a novel theoretical approach to correct sUAS-derived MS data after post-processing. Zhang et al. (2019) demonstrated how a power function could be used to remove the impact of sun glint from sUAS spectral data after collection and processing. Zhang et al. (2019) produced retrieval models for Chl-a and turbidity with R^2 values of 0.62 and 0.91, respectively. These data suggest the higher resolution dataset (e.g., HS), type of water (e.g., optically deep), and sun glint correction were adequate to quantify the OACs present. Using the assumed scattering efficiency of both silt and sand-size particles at each band slightly increased the developed models' predictability. However, applying the scattering efficiency of silt to the SMSC data produced the most predictive models with R^2 values of 0.62, 0.91, 0.59, and 0.61 for Chl-a, TSS, turbidity, and SDD, respectively. These model improvements suggest a simple exercise with several assumptions, and minimal ancillary

data collection efforts can improve the predictability of statistically derived surface water quality models.

2.4 Conclusions

In this study, sUAS-derived MS bands or band ratios could not accurately estimate traditional water quality parameters in a small optically shallow inland waterbody. Generally, the reported models exhibited low explanatory ability, yet were still capable of producing statistically significant (p-value < 0.05) results when estimating in-situ surface water quality. Considering the optical complexity of the studied waters throughout the study period and the documented limitations of this type of experiment, these results were promising and representative of statistical modeling in a complex natural environment. Furthermore, this study provides environmental professionals a review of various reflectance extraction techniques, the types of limitations to expect when attempting to precisely describe the relationship between reflectance data and in-situ water quality, and a novel scattering correction technique further post-processing sUAS-derived MS imagery exposed to optically shallow waters.

Based on these results, acceptable monitoring of optically shallow waters via sUAS is not possible. However, with the continued degradation of surface water quality worldwide, a reevaluation of conventional monitoring approaches is required. This study presents one such approach, and as sUAS technologies become more prevalent, the need for standard methods and integration into regular monitoring activities will be required. Currently, sUAS technologies are far from replacing traditional in-situ monitoring and should only be used as a tool for the collection of additional and different data. However, if integrated into regular monitoring activities, environmental monitors could use these technologies to identify *hotspots* at a much finer temporal and spatial

scale than conventional monitoring, which could substantially decrease the amount of time, money, human-hours, and laboratory analyses required to sufficiently characterize the extent of the issue.

Literature Cited

Abdelmalik, K. W. (2018). Role of statistical remote sensing for inland water quality parameters prediction. *The Egyptian Journal of Remote Sensing and Space Sciences*, https://doi.org/10.1016/j.ejrs.2016.12.002.

Arabi, B., Salama, M. S., van der Wal, D., Pitarch, J., and Verhoef, W. (2020). The impact of sea bottom effects on the retrieval of water constituent concentrations from MERIS and OLCI images in shallow tidal waters supported by radiative transfer modeling. *Remote Sensing of Environment,* https://doi.org/10.1016/j.rse.2019.111596.

Arango, J. G., and Nairn, R. W. (2020) Prediction of optical and non-optical water quality parameters in oligotrophic and eutrophic aquatic systems using a small unmanned aerial system. *Drones,* https://doi.org/10.3390/drones4010001.

ArduPilot. (2020). Mission Planner computer software. Resource document. ArduPilot. https://ardupilot.org/planner/. Accessed 8 July 2016.

Avdan, Y. Z., Kaplan, G., Goncu, S., Avdan, U. (2019). Monitoring the water quality of small water bodies using high-resolution remote sensing data. *ISPRS International Journal of Geo-Information,* https://doi.org/10.3390/ijgi8120553.

Becker, R. H., Sayers, M., Dehm, D., Shuchman, R., Quintero, K., Bosse, K., and Sawtell, R. (2019). Unmanned aerial system based spectroradiometer for monitoring harmful algal blooms: a new paradigm in water quality monitoring. *Journal of Great Lakes Research*, https://doi.org/10.1016/j.jglr.2019.03.006.

Biber, E. 2013. The challenge of collecting and using environmental monitoring data. *Ecology and Society*, https://doi.org/10.5751/ES-06117-180468.

Bonansea, M., Rodriguez, M. C., Pinotti, L., and Ferrero, S. (2015). Using multi-temporal Landsat imagery and linear mixed models for assessing water quality parameters in Río Tercero reservoir (Argentina). *Remote Sensing of Environment*, https://doi.org/10.1016/j.rse.2014.10.032.

Buiteveld, H., Hakvoort, J. H., and Donze, M. (1994). Optical properties of pure water. *Proceedings of the Society of Photo-Optical Instrumentation (SPIE) 2258*, *Ocean Optics XII,* https://doi.org/10.1117/12.190060.

Cannizzaro, J. P., and Carder, K. L. (2006). Estimating chlorophyll a concentrations from remote-sensing reflectance in optically shallow waters. *Remote Sensing of Environment*, https://doi.org/10.1016/j.rse.2005.12.002.

Chen, Y., Chen, K., and Hu, Y. (2006). Discussion on determination of phytoplankton chlorophyll-a by "Hot Ethanol Method" and its measurement error. *Journal of Lake Sciences*, https://doi.org/10.18307/2006.0519.

Cheng, C., Wei, Y., Lv, G., and Yuan, Z. (2013). Remote estimation of chlorophyll-a concentration in turbid water using a spectral index: a case study in Taihu Lake, China. *Journal of Applied Remote Sensing,* https://doi.org/10.1117/1.JRS.7.073465.

Dekker, A. G., Zamurović-nenad, Ž., Hoogenboom, H. J., and Peters, S. W. M. (1996). Remote sensing, ecological water quality modelling and in situ measurements: a case study in

shallow lakes. *Hydrological Sciences Journal*, https://doi.org/10.1080/02626669609491524.

Dörnhöfer, K., and Oppelt, N. (2016). Remote sensing for lake research and monitoring – recent advances. *Ecological Indicators*, https://doi.org/10.1016/j.ecolind.2015.12.009.

Doxaran, D., Froidefond, J-M., Lavender, S. and Castaing, P. (2002). Spectral signature of highly turbid waters: Application with SPOT data to quantify suspended particulate matter concentrations. *Remote Sensing of Environment*, https://doi.org/10.1016/S0034-4257(01)00341-8.

Ehmann, K., Kelleher, C., and Condon, L. E. (2019). Monitoring turbidity from above: Deploying small unoccupied aerial vehicles to image in-stream turbidity. *Hydrological Processes*, https://doi.org/10.1002/hyp.13372.

Elarab, M., Ticlavilca, A., Torres-Rua, A., Maslova, I., and Mckee, M. (2015). Estimating chlorophyll with thermal and broadband multispectral high-resolution imagery from an unmanned aerial system using relevance vector machines for precision agriculture. *International Journal of Applied Earth Observation and Geoinformation*, https://doi.org/10.1016/j.jag.2015.03.017.

Federal Aviation Administration (FAA). (2016). Title 14: Aeronautics and Space | Part 107 – Small Unmanned Aircraft Systems. Resource document. FAA. https://www.ecfr.gov/cgi-bin/text-idx?SID=dc908fb739912b0e6dcb7d7d88cfe6a7&mc=true&node=pt14.2.107&rgn=div5#se14.2.107_13. Accessed 29 June 2020.

Flener, C. (2013). Estimating deep water radiance in shallow water: adapting optical bathymetry modeling to shallow river environments. *Boreal Environment Research*, 18, 488-502.

Gordon, R. H. (2005). Normalized water-leaving radiance: revisiting the influence of surface roughness. *Applied Optics*, https://doi.org/10.1364/ao.44.000241.

Grayson, R. B., Finlayson, B. L., Gippel, C. J., and Hart, B. T. (1996). The potential of field turbidity measurements for the computation of total phosphorus and suspended solids loads. *Journal of Environmental Management*, https://doi.org/10.1006/jema.1996.0051.

Green, K., Congalton, G. R., and Tukman, M. (2017). Imagery fundamentals. In *Imagery and GIS: Best practices for extracting information from imagery* (pp. 27 – 68). California: Esri Press.

Guimarães, T. T., Veronez, R. M., Koste, C. E., Gonzaga, Jr. L., Bordin, F., Inocencio, C. L., Larocca, C. A., de Oliveira, Z. M., Vitta, C. D., and Mauad, F. F. (2017). An alternative method of spatial autocorrelation for chlorophyll detection in water bodies using remote sensing. *Sustainability*, https://doi.org/10.3390/su9030416.

Gurlin, D., Gitelson, A. A., Moses, J. W. (2011). Remote estimation of chl-a concentration in turbid productive waters – Return to a simple two-band NIR-red model? *Remote Sensing of Environment,* https://doi.org/10.1016/j.rse.2011.08.011.

Ha, N., Thao, N., Koike, K., and Nhuan, M. (2017). Selecting the best band ratio to estimate chlorophyll-a concentration in a tropical freshwater lake using Sentinel 2A images from a case study of Lake Ba Be (Northern Vietnam). *ISPRS International Journal of Geo-Information,* https://doi.org/10.3390/ijgi6090290.

Hadjimitsis, D. G., and Clayton, C. (2009). Assessment of temporal variations of water quality in inland water bodies using atmospherically corrected satellite remotely sensed image data. *Environmental Monitoring and Assessment*, https://doi.org/10.1007/s10661-008-0629-3.

Hardin, J. P., Lulla, V., Jensen, R. R., and Jensen, R. J. (2018). Small unmanned aerial systems (sUAS) for environmental remote sensing: challenges and opportunities revisited. *GIScience and Remote Sensing*, https://doi.org/10.1080/15481603.2018.1510088.

Jensen, R. J. (2007). *Remote sensing of the environment: an earth resource perspective – 2nd ed*. India: Prentice-Hall.

Kanick, S. C., Krishnaswamy, V., Gamm, U. A., Sterenborg, H. J. C. M., Robinson, D. J., Amelink, A., and Pogue, B. W. (2012). Scattering phase function spectrum makes reflectance spectrum measured from intralipid phantoms and tissue sensitive to the device detection geometry. *Biomedical Optics Express*, https://doi.org/10.1364/BOE.3.001086.

Kislik, C., Dronova, I., and Kelly, M. (2018). UAVs in support of algal bloom research: a review of current applications and future opportunities. *Drones*, https://doi.org/10.3390/drones2040035.

Kubiak, K., and Kotlarz, J. (2016). Monitoring Cyanobacteria Blooms in Freshwater Lakes using Remote Sensing Methods. *Polish Journal of Environmental Studies*, https://doi.org/10.15244/pjoes/60175.

Lacaux, J., Tourre, Y., Vignolles, C., Ndione, J., Lafaye, J. (2007). Classification of ponds from high-spatial resolution remote sensing: Application to Rift Valley Fever epidemics in Senegal. *Remote Sensing of Environment,* https://doi.org/10.1016/j.rse.2006.07.012.

Lee, Z., Carder, L. K., Mobley, D. C., Steward, G. S., and Patch, S. J. (1998). Hyperspectral remote sensing for shallow waters. A semianalytical model. *Applied Optics*, https://doi.org/10.1364/ao.37.006329.

Li, J., Yu, Q., Tian, Y. Q., and Becker, B., L. (2017). Remote sensing estimation of colored dissolved organic matter (CDOM) in optically shallow waters. *ISPRS Journal of Photogrammetry and Remote Sensing*, https://doi.org/10.1016/j.isprsjprs.2017.03.015.

MicaSense. (2019). What are the units of the Atlas GeoTIFF output. Resource document. Atlas and MicaSense. https://support.micasense.com/hc/en-us/articles/215460518-What-are-the-units-of-the-Atlas-GeoTIFF-output-. Accessed 27 Jun. 2018.

Miles, J. (2005). Tolerance and Variance Inflation Factor. *Encyclopedia of Statistics and Behavioral Science*, https://doi.org/10.1002/9781118445112.stat06593.

Millennium Ecosystem Assessment (MA). (2005). *Ecosystems and Human Well-Being: Synthesis*. Washington, DC: Island Press.

Mobley, D. C. (1994). Optical Properties of Water. In M. Bass (Ed.), *Handbook of Optics, Second Edition* (pp. 60 – 144). New York: McGraw-Hill, Inc.

Mouw, B. C., Greb, S., Aurin, D., DiGiacomo, M. P., Lee, Z., Twardowski, M., Binding, C., Hu, C., Ma, R., Moore, T., Moses, W., and Craig, E. S. (2015). Aquatic color radiometry remote

sensing of coastal and inland waters: challenges and recommendations for future satellite missions. *Remote Sensing of Environment*, https://doi.org/10.1016/j.rse.2015.02.001.

Nairn, R. W., LaBar, J. A., Strevett, K. A., Strosnider, W. H., Morris, D., Garrido, A. E., Neely, C. A., and Kauk, K. (2010). Initial evaluation of a large multi-cell passive treatment system for net-alkaline ferruginous lead-zinc mine waters. *Journal of the American Society of Mining and Reclamation (JASMR),* https://doi.org/10.21000/JASMR10010635.

Nansen, C. (2018). Penetration and scattering – two optical phenomena to consider when applying proximal remote sensing technologies to object classifications. *Public Library of Science (PLOS) One*, https://doi.org/10.1371/journal.pone.0204579.

Olmanson, L. G., Brezonik, P. L., and Bauer, M. E. (2013). Airborne hyperspectral remote sensing to assess spatial distribution of water quality characteristics in large rivers: The Mississippi River and its tributaries in Minnesota. *Remote Sensing of Environment*, https://doi.org/10.1016/j.rse.2012.11.023.

O'Neill, D. J., Costa, M., and Sharma, T. (2011). Remote sensing of shallow coastal benthic substrates: in situ spectra and mapping of Eelgrass (Zostera marina) in the Gulf Islands National Park Reserve of Canada. *Remote Sensing*, https://doi.org/10.3390/rs3050975.

Organization for Economic Cooperation and Development (OECD). (1982). *Eutrophication of waters: monitoring, assessment and control*. Paris, France: OECD.

Palmer, C.J. S., Kutser, T., and Hunter, D. P. (2015). Remote sensing of inland waters: Challenges, progress and future directions. *Remote Sensing of Environment*, https://doi.org/10.1016/j.rse.2014.09.021.

Platt, C. M. R., and Collins, L. R. (2015). LIDAR | Backscatter. In G. R. North (Ed.), *Encyclopedia of Atmospheric Sciences 2nd Edition* (pp. 270-276). Oxford: Academic Press.

Sadar, J. M. (1998). *Turbidity Science*. United States: HACH Company.

Scott, J. F. (2014). Scattering of electromagnetic radiation. *AccessScience*, https://doi.org/10.1036/1097-8542.605200.

Su, T.-C., and Chou, H.-T. (2015). Application of multispectral sensors carried on unmanned aerial vehicle (UAV) to trophic state mapping of small reservoirs: a case study of Tain-Pu Reservoir in Kinmen, Taiwan. *Remote Sensing*, https://doi.org/10.3390/rs70810078.

Su, T.-C. (2017). A study of a matching pixel by pixel (MPP) algorithm to establish an empirical model of water quality mapping, as based on unmanned aerial vehicle (UAV) images. *International Journal of Applied Earth Observation and Geoinformation*, https://doi.org/10.1016/j.jag.2017.02.011.

Turpie, R. K. (2013). Explaining the spectral red-edge features of inundated marsh vegetation. *Journal of Coastal Research,* https://doi.org/10.2112/JCOASTRES-D-12-00209.1.

United States Environmental Protection Administration (USEPA). (1993). Method 180.1: Determination of Turbidity by Nephelometry. Rev 2.0. Environmental Systems Monitoring Laboratory, Office of Research and Development, Cincinnati, Ohio.

USEPA. (1999). Method 160.2: Residue, Non-Filterable (Gravimetric, Dried at 103-105 C). Rev 2.0. Environmental Systems Monitoring Laboratory, Office of Research and Development, Cincinnati, Ohio.

Volpe, V., Silvestri, S., and Marani, M. (2011). Remote sensing retrieval of suspended sediment concentration in shallow waters. *Remote Sensing of Environment*, https://doi.org/10.1016/j.rse.2010.07.013.

Watanabe, F., Alcantara, E., Rodrigues, T., Rotta, L., Bernardo, N., and Imai, N. (2017). Remote sensing of the chlorophyll-a based on OLI/Landsat-8 and MSI/Sentinel-2A (Barra Bonita Reservoir, Brazil). *Anais da Academia Brasileira de Ciências,* https://doi.org/10.1590/0001-3765201720170125.

Wentworth, C. (1922). A scale of grade and class terms for clastic sediments. *The Journal of Geology,* 30(5), 377-392.

Whitehead, K., and Hugenholtz, H. C. (2014). Remote sensing of the environment with small unmanned aircraft systems (UASs), part 1: a review of progress and challenges. *Journal of Unmanned Vehicle Systems*, https://doi.org/10.1139/juvs-2014-0006.

Williams, J. D., Bigham, M. J., Cravotta III, A. C., Traina, J. S., Anderson, E. J., and Lyon, G. J. (2002). Assessing mine drainage pH from the color and spectral reflectance of chemical precipitates. *Applied Geochemistry*, https://doi.org/10.1016/S0883-2927(02)00019-7.

Wu, J.-L., Ho, C.-R., Huang, C.-C., Srivastav, A. L., Tzeng, J.-H., and Lin, Y.-T. (2014). Hyperspectral sensing for turbid water quality monitoring in freshwater rivers: empirical relationship

between reflectance and turbidity and total solids. *Sensors*, https://doi.org/10.3390/s141222670.

Wu, D., Li, R., Zhang, F., and Liu, J. (2019). A review on drone-based harmful algae blooms monitoring. *Environmental Monitoring and Assessment*, https://doi.org/10.1007/s10661-019-7365-8.

Zeng, C., Richardson, M., and King, D. (2017). The impacts of environmental variables on water reflectance measured using lightweight unmanned aerial vehicle (UAV)-based spectrometer system. *ISPRS Journal of Photogrammetry and Remote Sensing*, https://doi.org/10.1016/j.isprsjprs.2017.06.004.

Zhang, X., Li, H., Cybele, N. S. M., Dai, W., and Li, Z. (2019). Remotely sensed water reflectance measurements based on unmanned aerial vehicle (UAV). *International Society of Offshore and Polar Engineers,* 614-619.

Chapter 3: Using sUAS for the Development and Validation of Surface Water Quality Models in Optically Deep Mine Waters

This chapter was formatted as a manuscript for submission to Mine Water and the Environment.

Abstract:

Remote estimation of water quality is of increasing interest to monitoring professionals. Predictive regression models have been developed using satellite and small Unoccupied Aerial System (sUAS) remote sensing techniques. Typically, these remote sensing techniques were applied to optically deep waters (e.g., the bottom was not visible), targeting traditional contaminants of concern (e.g., chlorophyll-a and total suspended solids). Therefore, by considering a water body that is shallow in terms of physical depth (e.g., water surface to substrate surface), yet optically deep (e.g., highly turbid) like many mine water systems, examinations may be made of relationships between physical and optical depth, water clarity, water chemical composition, and spectral reflectance. Thus, this study's purpose was to demonstrate novel spectral monitoring techniques for mining-impacted surface waters utilizing spectral data from two different platforms. First, the feasibility of utilizing sUAS-derived multispectral imagery (e.g., tens of spectral measurements) to estimate in-situ metal concentrations in ferruginous lead-zinc mine drainage was examined. Results describe strong linear relationships (e.g., $R^2_{adj.} > 0.74$) between remotely collected multispectral reflectance and in-situ metal concentrations (e.g., Fe, Li, Mn, Pb, and Zn). Developed models could estimate mean metal concentrations within a percent of the observed value with great confidence (e.g., 70 percent confidence interval). The “success” of the non-optical metal predictions (e.g., metals not making a significant contribution to spectra – Li, Mn, Pb, and Zn) was attributed to the surface properties of the iron precipitates (e.g., high sorption affinity). Model validation at a site with waters of a different geologic origin allowed the authors to assess this phenomenon's site-specificity. Unfortunately, validation of all models developed (Mn, Ni, Pb, S, and Zn) was not possible within this study’s statistical constraints (e.g., prediction within ± 25 percent of the observed value). However, two models (Fe and Li) were validated, and when other relationships were examined with site-specific spectra, significant improvements were observed. Employing hyperspectral (e.g., thousands of spectral measurements) remote sensing techniques produced

a novel identification technique for optically shallow waters (e.g., the bottom was visible) and other remote sensing interferences. To do this, the exponential decay of light in water was modeled using two physical measurements (e.g., Secchi disk depth and actual depth) and sUAS-derived red band reflectance. The established level of confidence (e.g., $R^2 = 0.73$) observed using data from two different sites suggests this model may provide environmental monitors with a means to evaluate the feasibility of using remote sensing technologies to assess water quality in mine drainage passive treatment systems. Utilizing cost-effective sUAS-derived multispectral imagery to estimate mine water quality may represent a new tool and pave the way for the next generation of environmental monitoring. Adopting this technology will advance the efficiency and effectiveness of monitoring, alter traditional environmental remote sensing strategies, and provide a glimpse into the ever-advancing future of environmental restoration.

Keywords:

Regression, Remote Sensing, Multispectral, Hyperspectral, Optical Depth

3.1 Introduction

3.1.1 Monitoring Mining Impacted Environments

All mining stages (e.g., exploration, design and planning, construction, production, closure, and reclamation) influence landscapes worldwide (Sonter et al. 2014; Bebbington et al. 2018; Buczyńska 2020; Werner et al. 2020). However, mineral and fuel extraction is expected to continue for the foreseeable future (Martins et al. 2020), with an ever-increasing need for sustainable reclamation practices based on sound science. Reclamation of a mining-impacted landscape is not a rapid process and can require in-situ data across vast spatial and temporal scales (Werner et al. 2020). Unfortunately, evaluating mining reclamation projects' success is often disregarded due to time, person-hours, monetary and logistical constraints. Specifically, these attempts often fail to capture the spatial and temporal variation of complex inland water bodies (Holl 2002; Biber 2013; Becker et al. 2019).

Advancing environmental monitoring strategies and data collection technologies are critical. One such approach includes incorporating remote sensing data, specifically small Unoccupied Aerial System (sUAS)-derived information (e.g., multispectral reflectance) into traditional environmental monitoring and reclamation projects (Becker et al. 2019; Shi et al. 2019). As electromagnetic (EM) energy passes through Earth’s atmosphere and encounters an object, several interactions occur (e.g., reflection, transmission, absorption, and scattering) between the photons and particles within the medium. In a shallow and transparent water body, photons interact with the bottom substrate altering the expected energy signal (e.g., optically shallow waters (OSWs)) (Albert and Gege 2006; Cannizzaro and Carder 2006; Salama et al. 2009). Conversely, if optically active constituents (OACs) (e.g., particulate Fe, chlorophyll-a, total

suspended solids) are present in elevated concentrations rendering the bottom substrate not visible, even within physically shallow surface waters, visible (VIS) EM energy will decay at an exponential rate, and interactions with the substrate will be nominal (Cannizzaro and Carder 2006; Zeng et al. 2017). These factors of optically deep waters (ODWs) allow for the development of relationships between reflected spectral energy and in-situ metal concentrations.

Terrestrial applications of sUAS technologies have been practical in several mining phases (Lee and Choi 2016; Ren et al. 2019; Park and Choi 2020). Cress et al. (2015) established a roadmap for performing geological surveys in the conterminous United States. Lee and Choi (2016) demonstrated how sUAS could produce high-resolution topographic surveys. Fang et al. (2019) utilized hyperspectral data and regression techniques to map Fe accumulation in exposed soil at a reclamation site. Several authors have demonstrated how spectral measurements can estimate concentrations of various traditional OACs (e.g., chlorophyll-a, total suspended solids, and turbidity) (Dekker et al. 1996; Cannizzaro and Carder 2006; Lim and Choi 2015; Matthews and Odermatt 2015; Su 2017; Arango and Nairn 2020) in water bodies. However, limited research has examined how sUAS-derived multispectral reflectance can describe an aquatic environment impacted by mining activities.

However, most sUAS are not without their limitations (Whitehead and Hugenholtz 2014; Gholizadeh et al. 2016; Zeng et al. 2017; Zhang et al. 2019). Some regulatory and technical constraints of sUAS include flight altitude limitations, line of sight requirements, short flight times, and limited payload capabilities, along with concerns about GPS and sensor accuracy (Watts et al. 2012; FAA 2016; Ren et al. 2019). From a scientific perspective, the lack of a standardized operating procedure for collecting environmental data and applying it to

reclamation monitoring has been a considerable limitation identified by this study and others (Buters et al. 2019; Shi et al. 2019). Many authors have also commented on the difficulty of developing empirical models, referencing the need to derive site-specific inherent optical properties (IOPs) and manage complex signals from turbid water, bottom reflectance, and mixed pixels (Lee et al. 1998; Lee and Carder 2002; Voss et al. 2003; Cannizzaro and Carder 2006; Salama et al. 2009; Palmer et al. 2015; Gholizadeh et al. 2016; Su 2017). Thus, the need to establish robust datasets for non-traditional water quality parameters (e.g., metals) and explore the applications' potential is apparent.

3.1.2 Hypotheses and Purpose

The two hypotheses of this study were (1) coupling various bands or band transformations from sUAS-derived multispectral imagery, and in-situ surface-water quality will allow for the development of statistical models capable of predicting metal concentrations in mining-impacted surface waters and (2) water quality models will remain valid when developed and tested in waters of different geologic origin. Thus, this study's purpose was to demonstrate novel spectral monitoring techniques for mining-impacted surface waters utilizing spectral data from two different platforms. First, the feasibility of utilizing sUAS-derived multispectral imagery to estimate in-situ metal concentrations in lead-zinc mine drainage was examined. Then, the models were assessed for accuracy and statistical validity in coal mine drainage of a different geologic origin. Finally, a method to remotely evaluate a waterbody's potential for these applications of sUAS technologies was presented.

3.2 Materials and Methods

3.2.1 Study Site Descriptions

The study locations for this study were two mine drainage passive treatment systems (PTS). The Mayer Ranch PTS (MRPTS) and the Hartshorne PTS (HPTS) served as the test and validation study sites, respectively. MRPTS is located within the Tar Creek Superfund Site, in the Oklahoma portion of the 6475 km^2 Tri-State Lead-Zinc Mining District (TSMD) (Figures 3.1a, 3.1b, 3.1c, and 3.1d). Nearly 460 million tons of lead and zinc ore were produced from the mid-1800s to 1970, leaving a derelict landscape contaminated with mining-related hazards (e.g., mining waste and contaminated water resources) (ODEQ 2017). MRPTS was designed and implemented to address nearly 1000 L/minute of net-alkaline artesian-flowing mine drainage contaminated with elevated levels of As, Cd, Fe, Ni, Pb, Zn, and SO_4^{2-} (Nairn et al. 2020). Operated in two parallel treatment trains, the ten-cell PTS has effectively treated net alkaline ferruginous mine drainage since 2008 (Nairn et al. 2010). HPTS is located within the Oklahoma portion of the 87500 km^2 Arkoma Basin coal field (Figures 3.1a, 3.1b, 3.1e, and 3.1f). Specifically, HPTS is located adjacent to Rock Island Improvement (RI) mine #7 (e.g., RI #7), which from 1907 to 1931 had approximately 500,000 tons of Lower Hartshorne coal mined from more than 100 meters underground (Friedman 1996; USGS 1996). Designed to treat approximately 40 L/minute of net-acidic artesian-flowing mine drainage contaminated with elevated levels of Fe, Mn, and SO_4^{2-}. Since 2007, the six-cell PTS has consistently removed trace metals and mineral acidity and discharges a net alkaline effluent (LaBar and Nairn 2009; Nairn et al. 2020).

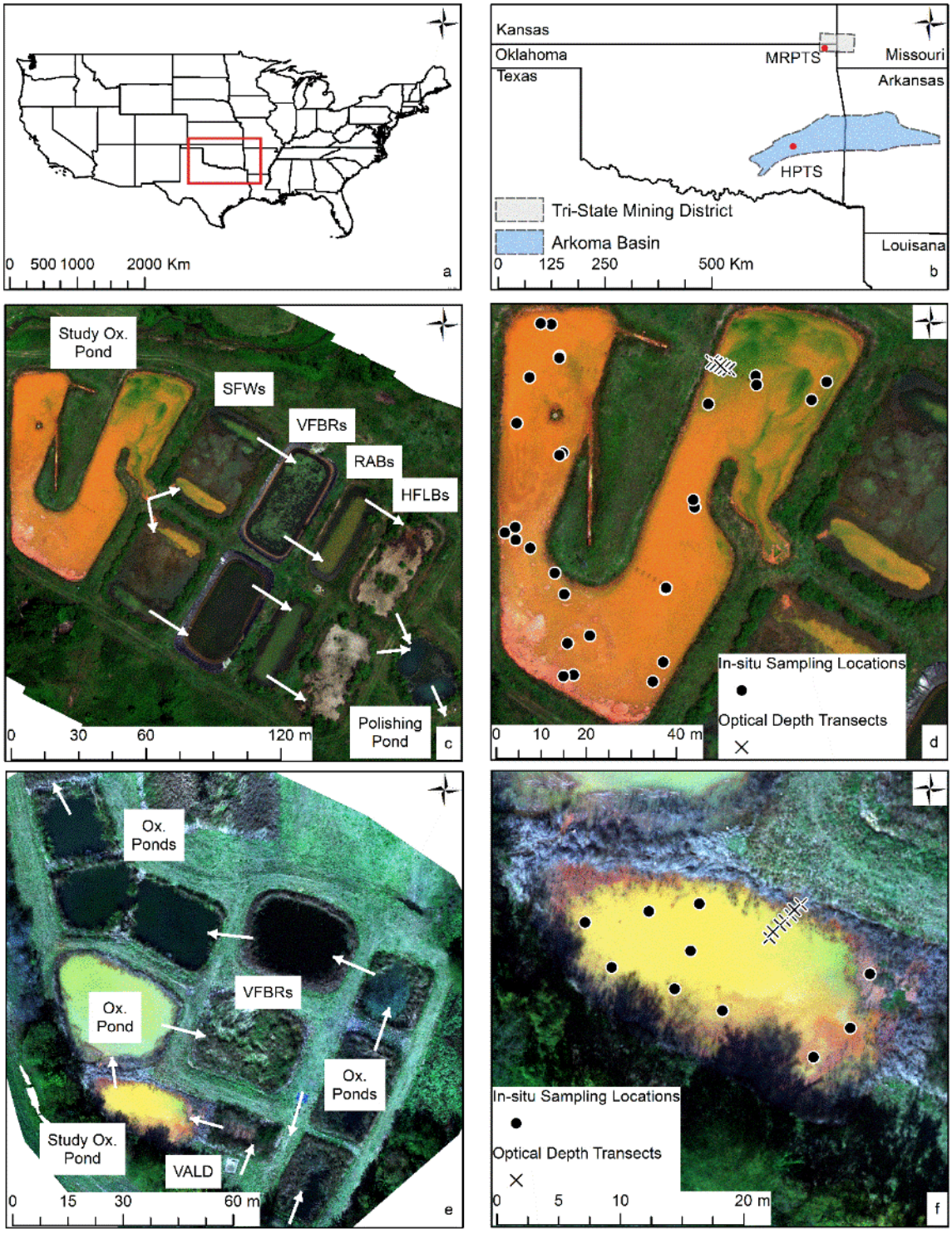

Figure 3.1 The study location within the United States of America (a), and general location within the state of Oklahoma (b). Mayer Ranch Passive Treatment System with process units identified with the general flow path indicated by white arrows (c) and the locations in-situ samples were collected and hyperspectral profiles were completed (d). Hartshorne Passive Treatment System with identification of groups of process units with the general flow path indicated by white arrows (e), and the locations in-situ samples were collected, and hyperspectral profiles were generated (f).

Both PTS has an initial oxidative unit near the beginning of the treatment train that served as the study ponds. It was the similarities concerning optical depth (OD), system design and age, influent water quality, and dominant optical properties that made the two oxidative units ideal candidates for testing water quality models developed using VIS/NIR EM energy. One important note is that each system's source waters differed in geologic origin and the targeted mining products (e.g., Pb and Zn at MRPTS; coal at HPTS). Mine drainage at MRPTS was produced from Mississippian carbonate host rocks (e.g., limestone and dolostone) with ores dominated by lead and zinc sulfides (McKnight and Fischer 1970). In contrast, mine drainage at HPTS stems primarily from the Hartshorne sandstone, which was characterized as quartzose sandstone with interbedded shales (Trumbull 1957). Understanding this difference in mine drainage development, the acidic nature (e.g., net alkaline versus net acidic) of the source waters was not crucial in the context of this study. However, what was important, was that due to the geologic host rock present at MRPTS and the incorporation of a vertical anoxic limestone drain (VALD) (alkalinity production via limestone dissolution and bicarbonate generation) (Figure 3.1e) at HPTS when the waters reached the studied units, both were net alkaline with elevated metal concentrations. Even though the studied waters were similar, assessing sUAS-derived models' validity in waters sourced from different geologic origins remains an unexplored scientific question.

3.2.2 In-situ Spectral Measurements

Before collecting spectral data, each instrument was field-calibrated. An Analytical Spectral Devices (ASD) FieldSpec3 was optimized and standardized with a white calibrated reflectance panel (CFP) to reflect 95 – 99 percent of EM energy. This calibration procedure was completed

every ten minutes or when illumination conditions changed (e.g., cloud cover) during data collection. The data generated at each wavelength represents the average of ten samples taken in 0.1 s increments. The hyperspectral (e.g., 350 – 2500 nm) profiles were collected at nadir (e.g., perpendicular to the water surface). Measurements were collected approximately one meter above the water surface at one-meter horizontal increments starting at the water's edge (e.g., 0-meters) (Figures 3.1d and 3.1e). Each set of ten measurements was collected five times, averaged, and post-processed to spectral reflectance using ASD ViewSpec Pro V. 6.2 processing software.

Calibration of the MicaSense RedEdge Multispectral Sensor (RedEdge sensor) required pre- and post-flight reflectance information from the same CFP. To account for changes to solar conditions throughout the flight, the processing software (Pix4DMapper) used both sets of images. The sensor was fixed via a gimbal to the Aerial Technologies International (ATI) vertical take-off and landing (VTOL) AgBot quadcopter. This VTOL sUAS simultaneously collected imagery in five discrete spectral bands (e.g., blue, green, red, rededge, and near-infrared (NIR)) with center points at 475, 560, 668, 717, and 840 nm, respectively. At both PTS, the sUAS-derived multispectral imagery was collected autonomously within ±2 hours of local solar noon. The flight planning software (Mission Planner V. 1.3.37) allowed for the development of autonomous missions throughout the study. Parameters at each PTS included operations at 6 meters second^{-1}, 60 meters above ground level, with at least 75 percent image side and overlap. With these parameters, the raw uncompressed 16-bit digital number imagery was transformed to high-resolution (e.g., < 10 cm per pixel) 32-bit spectral reflectance orthomosaics using the processing

software. If remote sensing interferences impacted either multispectral spectral dataset, outliers were identified and removed using the interquartile range of each multispectral band.

3.2.3 In-Situ Water Quality

The model development dataset consisted of thirty in-situ surface water grab samples collected from MRPTS during the summer of 2019, within ± 1-hour of acquiring the spectral measurements. Using a fully extended 3.6-meter swing-arm sampling pole allowed the collection of twenty samples from the pond's shore below the surface (< 1-meter) or until the 1-L HDPE bottle was no longer visible. Ten additional samples were collected similarly from the center of the pond via a canoe. The validation data set comprised ten in-situ surface water grab samples from HPTS during the fall of 2020. Samples at HPTS were collected in the same manner as the shoreline samples at MRPTS. At every sampling location, GPS coordinates and samples for total and dissolved (<0.45 µm) metal analyses were collected. Total and dissolved metals (e.g., Ag, Al, As, Ba, Ca, Cd, Co, Cr, Cu, Fe, K, Li, Mg, Mn, Na, Ni, Pb, S, Se, Si, and Zn) were analyzed following EPA approved methods (e.g., EPA 3015A (1994) and EPA 6010C (2000)) which allowed for the particulate fraction also to be calculated (e.g., total minus dissolved). To further characterize the water body while remaining within the desired time window (1-hour) of sUAS flights, alkalinity (e.g., EPA 310.1 (1978)), turbidity (e.g., ASTM 2130-B (2017)), and multiple physicochemical parameters (e.g., temperature, pH, specific conductance) measurements were collected only from the center of the pond at MRPTS. Statistical differences between the two sets of water quality data were quantified using Welch's unequal variances T-test and Tukey-Kramer test in Microsoft Excel. By employing these tests, data sets could be compared without assumptions regarding variance or

sample size. Outliers in each water quality dataset were identified and removed using the interquartile range of each water quality parameter.

3.2.4 In-Situ Examination of Optical Depth Influences

After collecting spectral data, Secchi disk depth (SDD) and actual water depth (AD) were measured in transects at equal increments (e.g., 1-meter) from the shores of the oxidation ponds (Figures 3.1d and 3.1e). To minimize the resuspension of substrate and modification of the water column's optical properties, SDD was measured first. Then AD was measured by lowering a weighted line into the water column until it contacted the substrate's surface. Assuming that SDD is proportional to OD, an SDD to AD ratio equal to one would result in remote sensing interferences (e.g., bottom substrate). Derivation of the relationship used the SDD to AD ratio and reflectance from the center point of the RedEdge sensor red band (668 nm) from both PTS (e.g., OD model). Utilizing the Raster Calculator in ArcMap V. 10.6.1 to generate a surface demonstrated the ability to identify remote sensing interferences in ODWs (e.g., SDD: AD ≥ 1).

3.2.5 Modelling Surface-Water Quality

Overall, the approach used to develop the water quality models followed the empirical method described by Dekker and Donze (1994) and applied by numerous other authors, as mentioned earlier. This method utilizes derived statistical relationships between measured multispectral reflectance and in-situ water quality. However, the authors of this study will attempt to disprove the statement that “the results have no multitemporal validity” made by Dekker and Donze (1994) when commenting on the practical limitations of such models.

Candidate water quality models were identified by first performing exploratory ordinary least squares (OLS) regression in ArcMap V. 10.6.1. OLS regression uses the entire dataset to minimize

the mean squared error (MSE) of the algorithm. Each exploratory run evaluated every possible combination (approximately 40,000) of one, two, and three input candidate explanatory variables (e.g., untransformed and log-transformed multispectral reflectance bands and band ratios) to develop the OLS models that best explained the dependent variable (e.g., in-situ total and particulate metal concentrations). Relationships among these variables were identified using the correlation coefficient (R), allowing for simple data exploration. Model selection criteria (Table 3.1) were set to satisfy OLS regression assumptions and produce statistically significant, well-fit, and unbiased surface water quality models.

The OLS tool in ArcMap V. 10.6.1 provided a way to calculate and evaluate the criteria in Table 3.1. However, a brief explanation of each metric may assist with interpreting the results of this study. An insignificant Jarque-Bera Statistic (p-value > 0.01) indicated the regression residuals (e.g., observed minus predicted value) were normally distributed, and the predictions displayed no significant bias. Non-normally distributed residuals suggest not all explanatory variables were accounted for, nonlinear relationships were modeled, or outliers significantly impacted the models (ESRI 2018). The Koenker Studentized (Bruesch-Pagan) (BP) Statistic (e.g., Koenker) was used to assess the consistency of the relationship between the independent and dependent variables in geographic and dataspace. Specifically, if the relationship (e.g., slope) was similar between the variables at all sampling locations (e.g., stationary) and that relationship did not change (e.g., linear to nonlinear) with changes in the magnitude of the explanatory variable (e.g., homoscedasticity) the models were specified correctly (e.g., a key variable was not missing). Moran's I and Getis-Ord Global G (Gi^*) were used to assess spatial autocorrelation and clustering of the raw data and regression residuals. Evidence of significant spatial autocorrelation (p-value

> 0.05) further suggests an explanatory variable was excluded from the model. Clustering was used to identify if any sampling location or region produced consistently higher or lower values (e.g., high-low clusters) which was considered significant at p-values > 0.05. The Joint-F test Statistic (Joint-F) provided an assessment of multiple regression model significance (p-value < 0.01) compared to a model with no independent variables (e.g., intercept only model). Finally, the Variance Inflation Factor (VIF) was a metric describing the redundancy among explanatory variables in the multiple regression model. VIF is the reciprocal of tolerance. Although no explicit rule exists, some authors have suggested that VIF > 10 indicates severe collinearity, poor estimation of regression coefficients, and an inflated standard error of the regression (Marquardt 1970; Miles 2005). All the statistical metrics and tools described in this paragraph were outputs from the OLS tool or analyzed separately in ArcMap V. 10.6.1 (ESRI 2018).

Table 3.1 Exploratory regression model criteria set to satisfy the assumptions of OLS regression in ArcMap V. 10.6.1.

Statistical Parameter	Selection Threshold
$R^2_{adjusted}$	> 0.75
Minimum Jarque-Bera	p-value > 0.01
Minimum Koenker	p-value > 0.01
Minimum Moran's I	p-value > 0.05
Minimum Getis-Ord	p-value > 0.05
Maximum Joint-F	p-value < 0.01
Maximum VIF	< 7.5

Models selected for further evaluation outperformed the selection criteria. In these cases, models with the highest adjusted (e.g., number of explanatory variables) coefficient of determination ($R_{adj.}^2$) and lowest Akaike information criterion adjusted for small sample sizes (AICc) were chosen for testing and validation. Several metrics (e.g., residuals, percent difference, MSE, Mean Absolute Error (MAE), along with the upper and lower confidence intervals) assessed the validity of the models developed and tested in MRPTS waters at HPTS. Acceptance of the

experimental hypotheses required (1) that the models produce predictions of MRPTS metal concentrations within the 75 percent confidence interval and (2) the predicted HPTS mean metal concentrations fall within ±25 percent of the measured value.

3.3 Results and Discussion

3.3.1 In-situ Water Quality

Mean in pond metal concentrations at MRPTS and HPTS were similar to mining-impacted waters found throughout the TSMD and Arkoma Basin, respectively (Table 3.2) (LaBar and Nairn 2009; Nairn et al. 2010). Some parameters were not detected in either system (Ag, As, Cr, and Se). Others (Ba, Ca, K, Mg, Na, and Si) were not considered due to the minimal environmental risk posed at the observed concentrations. Additionally, some metals (Cd, Co, and Cu) were quantifiable (e.g., > PQL) at MRPTS but not at HPTS, thus were not considered within the context of this manuscript (Holzbauer-Schweitzer and Nairn 2020). Emphasis will be placed on in-situ particulate Fe, and total Li, Mn, Ni, Pb, S, and Zn concentrations.

A statistical review of the relationships between water quality parameters revealed that Li, Mn, Ni, Pb, S, and Zn were strongly collinearly related ($R > 0.90$) at MRPTS. Interestingly, the dominant OAC (particulate Fe) exhibited no relationship ($R < 0.10$) with the other metals. At HPTS, only Li, Mn, Ni, Pb displayed strong collinearity ($R < -0.80$). S exhibited weak relationships ($R < 0.20$) with the investigated metals, and Zn was only moderately related ($R = 0.64$, -0.55, and 0.68) with Li, Mn, and Ni, respectively. However, the dominant OAC (particulate Fe) in this system displayed relationships of varying strength ($R = 0.83$, -0.48, 0.71, -0.54, 0.14, and 0.59) with Li, Mn, Ni, Pb, S, and Zn, respectively. Neither set of water quality data displayed significant signs of spatial autocorrelation (Moran's I) or hotspots (Getis-Ord Gi^*) when evaluated in ArcMap V. 10.6.1. In

total, outliers represented 10 percent (one water quality sample) and 7 percent (two water quality samples) of the data at HPTS and MRPTS, respectively. It appeared both sets of outliers were produced while attempting to collect surface samples representative of reflectance measurements near the surface debris (amorphous iron-oxyhydroxide) persistent in each oxidation pond.

Table 3.2 Observed in-situ multispectral reflectance for each band and water quality for the metals examined; dataset minimum (Min.), maximum (Max.), variance (Var.) and Welch's T-Test Assuming Unequal Variance (W-T) and Tukey-Kramer Test (T-K) were used to assess significant differences between the two sets (e.g., Mayer Ranch Passive Treatment System (MR) and Hartshorne Passive Treatment System (H)) of samples; "-" in the T-K column indicates samples were analyzed using the W-T test, and vice versa both examinations were evaluated at p-value < 0.05, indicated by "" for significantly different sets.*

Parameter	Site	Mean	Median	Min.	Max.	Var.	W-T p-value	T-K p-value
Reflectance								
Blue	MR	0.040	0.038	0.027	0.079	1.15E-04	6.46E-02	-
	H	0.036	0.037	0.029	0.038	7.27E-06		
Green	MR	0.106	0.105	0.082	0.125	1.95E-04	-	1.48E-01
	H	0.115	0.125	0.082	0.136	3.70E-04		
Red	MR	0.205	0.191	0.175	0.262	8.51E-04	-	7.57E-04*
	H	0.246	0.255	0.216	0.275	4.82E-04		
NIR	MR	0.130	0.113	0.083	0.303	2.61E-03	3.99E-03*	-
	H	0.089	0.079	0.075	0.134	3.72E-04		
RedEdge	MR	0.199	0.197	0.153	0.316	1.41E-03	7.86E-01	-
	H	0.197	0.198	0.175	0.206	7.53E-05		
[Metals] (mg L^{-1})								
Total Li	MR	0.259	0.245	0.231	0.289	6.51E-04	-	6.35E-12*
	H	0.378	0.373	0.330	0.432	9.08E-04		
Total Mn	MR	1.167	1.118	1.053	1.285	9.31E-03	2.19E-23*	-
	H	1.918	1.919	1.885	1.946	3.09E-04		
Total Ni	MR	0.658	0.634	0.581	0.742	4.13E-03	4.33E-23*	-
	H	0.045	0.045	0.042	0.049	4.28E-06		
Total Pb	MR	0.297	0.279	0.260	0.333	8.70E-04	8.67E-22*	-
	H	0.067	0.067	0.064	0.072	6.54E-06		
Total S	MR	746	709	661	832	5.39E+03	3.46E-14*	-
	H	478	478	474	485	1.11E+01		
Total Zn	MR	4.115	4.110	3.556	4.580	1.39E-01	2.03E-24*	-
	H	0.025	0.023	0.020	0.036	3.45E-05		
Particulate Fe	MR	10.59	9.15	4.89	22.01	2.57E+01	-	9.35E-01
	H	10.75	9.91	4.51	17.01	1.28E+01		

3.3.2 Spectral Measurements

At MRPTS, an evaluation of the relationships between individual reflectance bands revealed strong relationships between blue and NIR (R = 0.76) and NIR and rededge (R = 0.76). The red band exhibited relationships with rededge and green bands (R = 0.68 and 0.52, respectively). Otherwise, little to no correlation (R < 0.50) was observed for reflectance values at the MRPTS sampling locations. Fortunately, wind action issues (e.g., glint), cloud cover, and optical depth were minimal. However, interferences from surface debris (e.g., amorphous iron-oxyhydroxide) and algae growth were present, particularly in the southwestern and northeastern portions of the MRPTS oxidation pond, respectively (Figure 3.1d).

Multispectral reflectance values at HPTS were more strongly correlated than MRPTS, but the most robust relationships were observed between different sets of bands. The green band exhibited strong correlations with the red and NIR bands (R = 0.92 and -0.93, respectively). The red and NIR bands also displayed a strong negative relationship (R = -0.78). Surprisingly, little correlation between the red and rededge bands (R = 0.11) existed. The lack of relationship between these bands could be due to some remote sensing interferences present. For example, the surface debris present at MRPTS was also present at HPTS but to a greater degree. Shadows caused by trees adjacent to the pond were also present, but all samples were collected outside of the impacted area. On average, the rededge band had a 25 percent greater response (e.g., higher reflectance) than the red band reflectance. Anderson and Robbins (1998) supported these results finding that iron-oxide precipitates have peak reflectance values above 700 nm. Furthermore, Jackisch et al. (2018) indicate that goethite has an absorption edge at 668 nm, which was the red band's center point, resulting in lower reflectance values. An evaluation of the

hyperspectral profiles confirms the presence of this absorption feature when in ODWs at both PTSs (e.g., MRPTS 2 and 4 m; HPTS 2 and 3 m) (Figure 3.2). The absence of spectral outliers was confirmed using the remote sensing interference raster (OD model) described earlier.

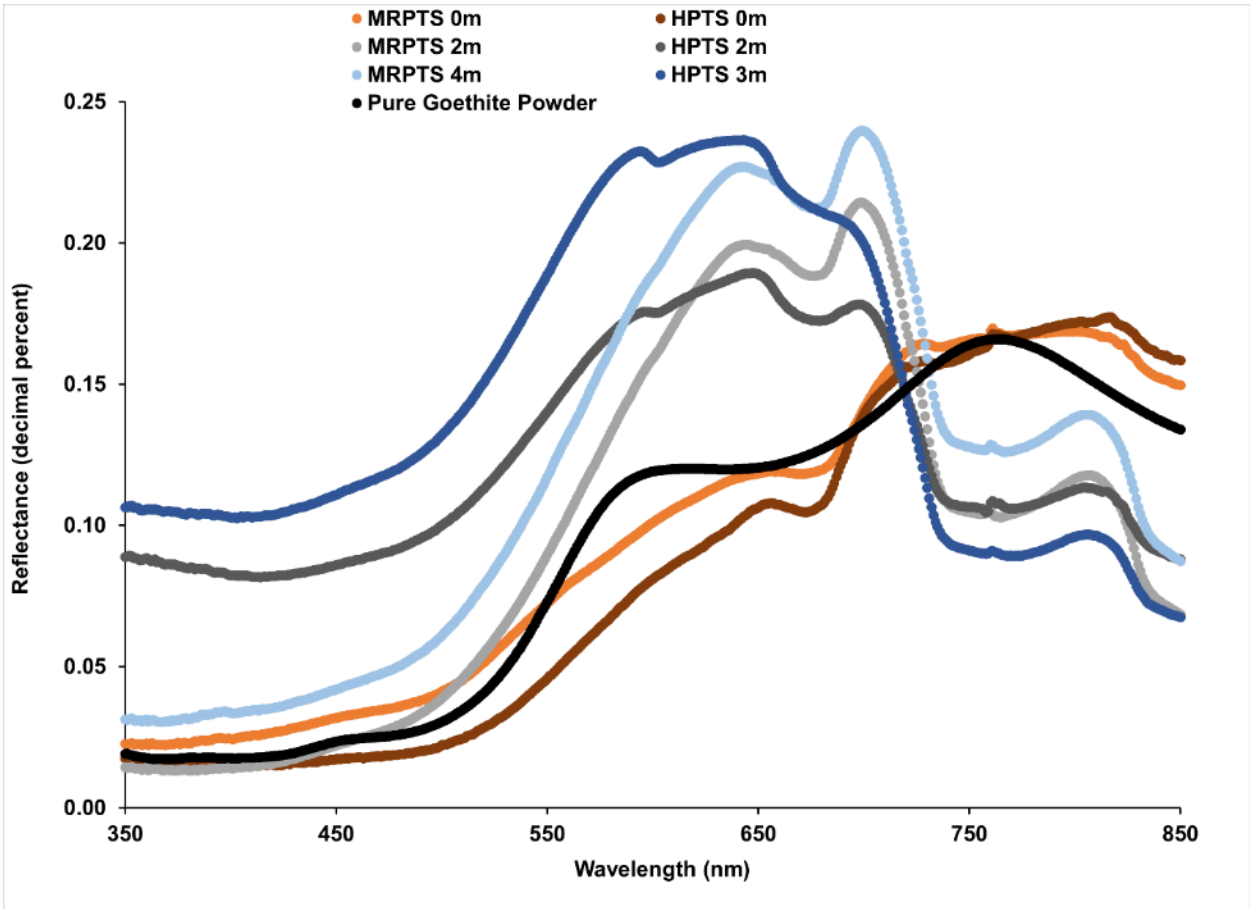

Figure 3.2 Hyperspectral profiles displaying the effect that remotely sensing substrate (e.g., OSW) had on measured reflectance (e.g., MRPTS and HPTS 0 m) compared to ODWs (e.g., MRPTS 2 and 4 m; HPTS 2 and 3 m), with all compared to reflectance of a sample of dried pure goethite powder from Kokaly et al. (2017).

3.3.3 Developing and Testing Surface Water Quality Models: MRPTS

Every explanatory variable (e.g., band or band ratio) included in each OLS regression model made significant contributions (p-value < 0.05). Each model was also statistically significant (p-value < 0.01; Joint F Statistic). The explanatory variables displayed no significant redundancy (VIF < 7.5), spatial autocorrelation (p-value > 0.05; Global Moran's I), or clustering (p-value > 0.05; Getis-Ord

Gi*) with one another. Values produced by the models displayed no significant bias (p-value > 0.01; Jarque-Bera Statistic), and the residuals were not significantly different from a normal distribution. Overall, the Koenker Statistic (p-value > 0.01) verified that the observed relationships were stationary and homoscedastic, indicating the models were properly specified (Table 3.3).

*Table 3.3 Developed total and particulate metal models passing the set model criteria at MRPTS. Blue, green, red, rededge, and NIR symbolized B, G, R, RE, and NIR, respectively. Log transformations of bands or band ratios abbreviated with "L". Significance at p-value (p) < 0.01 and 0.05 symbolized with * and **, respectively.*

Metal	**Total Li**	**Total Mn**	**Total Ni**	**Total Pb**	**Total S**	**Total Zn**	**Particulate Fe**
Coefficient 1	-1.66	0.30	-1.19	-1.61	-1508.99	-4.267	110.48
Variable 1	G*	RE_G*	R*	G*	R*	R*	NIR*
Coefficient 2	0.21	-0.98	-0.23	0.11	-282.67	-0.71	-5.81
Variable 2	B_NIR*	L_R*	NIR_R*	L_R_RE*	NIR_R*	NIR_G*	NIR_B**
Coefficient 3	0.09	-0.62	0.19	0.11	225.18	1.39	24.49
Variable 3	L_B_RE*	L_R_NIR*	RE_G*	L_NIR_RE*	RE_G*	RE_G*	L_B_R**
Intercept	0.18	0.40	0.67	0.22	788.49	3.21	-35.51
AICc	-126.60	-65.18	-85.97	-121.98	240.28	-2.19	112.12
$R^2_{adjusted}$	0.76	0.76	0.77	0.78	0.76	0.74	0.81
Jarque-Bera p	0.99	0.97	0.67	0.98	0.70	0.70	0.74
Koenker p	0.17	0.42	0.63	0.26	0.34	0.99	0.05
Moran's I p	0.08	0.07	0.07	0.07	0.08	0.10	0.79
Getis-Ord p	0.84	0.86	0.77	0.96	0.90	0.70	0.24
Joint-F p	< 0.01	< 0.01	< 0.01	< 0.01	< 0.01	< 0.01	< 0.01
VIF	2.57	2.10	2.10	1.22	2.10	3.27	2.56

When tested at MRPTS, the assessed models (Table 3.4) produced promising results. All tests were performed on each sample and averaged to produce a single value to simplify and more closely resemble results of a traditional in-situ sampling event (e.g., one in-situ sample). Only three models (Fe, Ni, and S) produced a greater than one percent difference from the observed mean concentrations. The same models also exhibited the highest bias at 0.64, 0.02, and 18.73

mg L^{-1}, respectively. Furthermore, only a 90 percent confidence interval for the Ni and S models could be achieved ([0.64, 0.66] and [718.45, 742.99], respectively). For metals with mean concentrations below 1 mg L^{-1} (e.g., Li, Ni, and Pb), the standard deviation of the predicted Ni concentrations was the greatest, increasing the interval's relative size. Thus, it was expected for Ni to fall within the established confidence interval.

Table 3.4 MRPTS testing metrics from developed OLS models passing set criteria. All values presented in mg L^{-1}, unless otherwise noted (e.g., Mean percent (%) difference); Confidence limits (CL) for Li, Mn, Pb, Zn, and Fe were established at 70 percent while values for Ni and S represent the 90 percent confidence limit; MSE and MAE stand for Mean Standard Error and Mean Absolute Error, respectively.

	Total Li	**Total Mn**	**Total Ni**	**Total Pb**	**Total S**	**Total Zn**	**Particulate Fe**
Measured mean	0.26	1.17	0.66	0.30	749	4.15	12.40
Predicted mean	0.26	1.17	0.65	0.30	731	4.14	11.76
Mean residual	-3.45E-4	2.78E-3	1.58E-2	2.99E-4	1.87E+1	1.34E-2	6.36E-1
MSE	0.00	0.07	0.01	0.00	10523.59	0.01	12.13
MAE	0.01	3.24	0.03	0.01	18.73	0.17	3.61
Mean % difference	-0.13	0.24	2.39	0.10	2.50	0.32	5.13
Upper CL	0.27	1.18	0.66	0.30	745.96	4.20	12.75
Lower CL	0.26	1.15	0.63	0.29	715.48	4.10	10.78

Regardless, the observed success of all other models (e.g., particulate Fe, and total Li, Mn, Pb, Zn) warranted further discussion. These total models displayed negative relationships ($R < -0.36$ and -0.58) with the blue and green bands, respectively, while exhibiting strong collinearity among each other ($R > 0.90$). Because the total metals were considered non-optical (e.g., constituents with little to no contribution to the observed spectra), the relationships with visible reflectance must be explained. Thus, the fact that the red band was not used more extensively to model the dominant optical parameter (particulate Fe) was somewhat unexpected. Theoretically, regions with deeper red colors would contain elevated particulate Fe concentrations and reflect proportionally more red EM energy. The observed strength ($R = 0.88$) of the linear relationship

between the red band and particulate Fe supported this theory. Since the blue and green bands were included in every non-optical metal model, other interactions likely occurred. Torren and Baron (2002) note that Fe oxides can also reflect strongly in the NIR while absorbing blue energy. Therefore, as particulate Fe concentrations increased, so did the quantity of red EM reflected, which proportionally decreased the amount of blue and green EM reflected (e.g., spectral shifting). As concentrations of non-optical metals collinearly decreased, the amount of blue and green EM increased. However, due to the spectral shifting (e.g., dominant optical properties), the increase likely occurred at longer wavelengths (e.g., red, rededge, or NIR). This shift was evident in the band or band ratios used to estimate the non-optical metals (e.g., a combination of blue, green, or NIR in every model). Thus, it appears this study exploited these fundamental EM interactions and physical relationships (e.g., prominence and adsorption capabilities of iron-oxyhydroxides) to successfully develop predictive, unbiased, and robust surface water quality models.

Although the 75 percent confidence interval of two models (Ni and S) did not contain the observed mean values, the study's overall success warranted an acceptance of the first hypothesis. The observed mean values for only these two models were within all calculated confidence intervals above 85 percent. All other models had observed mean values within at least a 70 percent confidence level. According to Petty (2012), a 95 percent confidence level is acceptable; however, some simulation experts use a confidence level of 80 percent for statistical validation. With lower confidence exist lower probability estimates fall within the intervals, but those estimates will have higher precision. Therefore, the levels of confidence established were deemed appropriate for a novel environmental study of this nature.

3.3.4 Validating Surface Water Quality Models: HPTS

Validation of the models developed and tested at MRPTS at HPTS produced mixed results. Ideally, at each PTS, the relationships between the independent and dependent variables (e.g., in-situ water quality and multispectral reflectance, respectively) would be proportional. Unfortunately, that was not observed, either in terms of the band and band ratios used or the relationships' directionality. Otherwise, most models exhibited bias proportional to the differences in the two datasets' mean metal concentrations, and all concentrations except Zn produced randomly distributed residuals (Table 3.5 and Figure 3.3). The Zn model did not perform well because not only were the two water quality datasets significantly different (p-value = 2.03E-24; Welch's Test), but the difference was greater than two orders of magnitude. Reflectance measurements did not appear to be the cause because the bands (e.g., blue, red, NIR) that exhibited significant differences (p-value < 0.05) between the two PTSs were also used in some combinations for all other models. Since the optical properties at MRPTS and HPTS were comprised primarily by Fe, the ability to derive meaningful statistical relationships must be attributed to the prominence and adsorption capabilities of iron-oxyhydroxides.

Table 3.5 HPTS validation metrics from applied OLS models developed at MRPTS. All values presented in mg L^{-1}, unless otherwise noted (e.g., e.g., Mean percent (%) difference). All established confidence limits (CL) represent the 95th percentile. MSE and MAE stand for Mean Standard Error and Mean Absolute Error, respectively.

	Total Li	**Total Mn**	**Total Ni**	**Total Pb**	**Total S**	**Total Zn**	**Particulate Fe**
Measured mean	0.38	1.91	0.45	0.07	478	0.03	10.75
Predicted mean	0.29	1.23	0.67	0.10	790	4.04	10.21
Mean residual	0.09	0.68	-0.22	-0.03	-312.09	-4.01	0.54
MSE	0.07	4.69	0.42	0.01	876610	144.79	2.60
MAE	0.09	0.76	0.22	0.03	312.09	4.01	1.55
Mean % difference	-23.18	-35.75	48.51	46.92	65.29	16582	-0.53
Upper CL	0.30	1.26	0.69	0.11	814.34	4.16	11.96
Lower CL	0.27	1.20	0.64	0.09	765.83	3.91	8.46

Furthermore, an apparent need to develop site-specific IOPs (Salama et al. 2009) seems unnecessary and overly complicated considering the disagreements regarding the theory of IOPs (Morel 2005). In-situ determinations of IOPs can prove problematic due to various physical, environmental, and instrumental limitations (Roesler and Boss 2007). Incorporating IOPs requires several assumptions, further complicating the modeling process, mainly because it is impossible to measure the IOPs of each constituent (Roesler and Boss 2007). Thus, it appears when remote sensing in the VIS/NIR range with limited spectral resolution (e.g., five narrow bands), the sensor-perceived color had a greater impact. The color of the studied systems was primarily a result of reflectance from iron-oxyhydroxides within the water column. The optical prominence of Fe paired with its linear relationship with total Li ($R = 0.83$) allowed for the development of models capable of accurately (e.g., ±25 percent of the measured value) describing these two metals (Table 3.5). However, in this study, the application of empirically derived surface water quality models confirmed the site-specific limitation discussed by numerous studies (Lee and Carder 2002; Voss et al. 2003; Cannizzaro and Carder 2006; Salama et al. 2009; Palmer et al. 2015; Gholizadeh et al. 2016; Su 2017). Although validation of meaningful statistical relationships was possible for two models (e.g., particulate Fe and total Li), all other models failed to meet the validation criteria (e.g., ±25 percent of the measured value) (Table 3.5) and warrant further examination. Thus, the second hypothesis was rejected because five of the seven studied metal models were not verifiable within the set criteria and scope of this study.

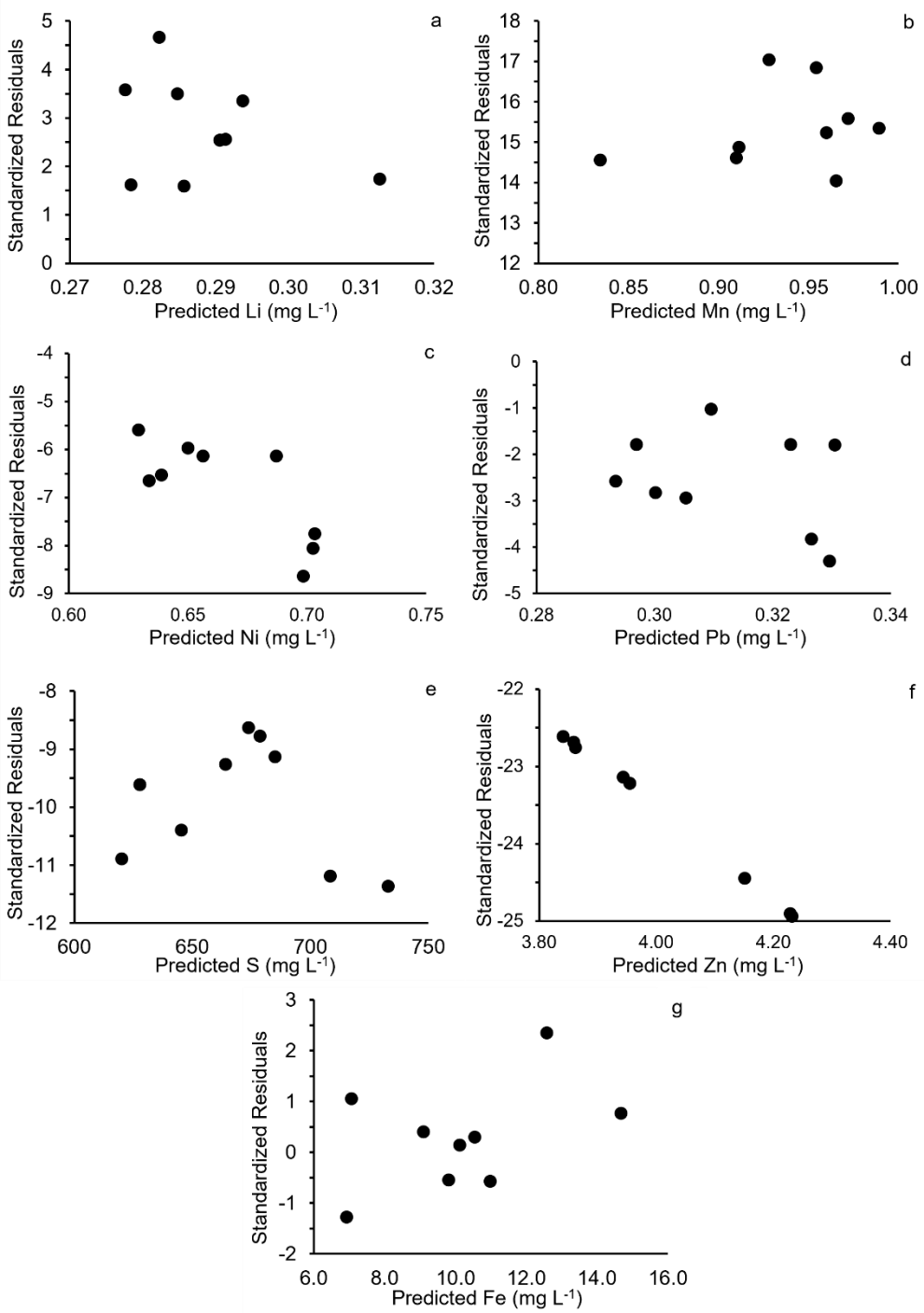

Figure 3.3 HPTS OLS regression residuals normalized by the standard deviation of the population versus the examined metal concentration estimated by applying the MRPTS OLS models.

By completing several other analyses, it could be determined whether the hypothesis's rejection was due to the applied models or simply lack of relationships between variables. The relationships between some of the independent and dependent variables at each PTS were drastically different. Exploratory regression at HPTS was used to quantify these differences. This exercise resulted in an entirely different set of independent variables (e.g., band or band ratios) capable of effectively describing in-situ water quality at HPTS. All models were properly specified and homoscedastic (p-value > 0.01; Koenker Statistic), produced statistically unbiased and normally distributed residuals (p-value > 0.01; Jarque-Bera Statistic), and exhibited no evidence of spatial autocorrelation (p-value > 0.05; Moran's I) (Table 3.6). The theory of utilizing sUAS-derived multispectral imagery to model in-situ water quality appears to be statistically valid. Unsurprisingly, some data used to develop models tested at HPTS were significantly different (p-value < 0.05; Welch's Test and Tukey-Kramer) than values measured at HPTS (Table 3.2). The only variables that did not exhibit significant differences were the blue, green, and rededge bands and particulate Fe concentrations (p-value = 0.07, 0.15, 0.79, and 0.94, respectively). Thus, the empirical nature of these models, particularly the range of OAC concentrations and types modeled paired with the difficulty of identifying relationships between various environmental processes across spatial and temporal scales, remains a complex challenge and requires future studies (Dekker and Donze 1994; Seppelt et al. 2009; Bennett et al. 2013).

*Table 3.6 Results of exploratory regression analysis with models using only in-situ HPTS data that passed set criteria. Blue, green, red, rededge, and NIR symbolized B, G, R, RE, and NIR, respectively. Particulate Fe concentrations, turbidity values, Akaike Information Criterion correct for small sample sizes, and Variance Inflation Factor symbolized as [Part. Fe], Turb, AICc, and VIF, respectively. Positive and negative signs before the variable indicate the directionality of the relationship. Significance at p-value (p) < 0.01 and 0.05 symbolized with * and **, respectively.*

	Total Li	**Total Mn**	**Total Ni**	**Total Pb**	**Total S**	**Total Zn**	**Particulate Fe**
Variable 1	+R_NIR*	-	+NIR*	+G_NIR*	-B_R*	+NIR*	-G_NIR*
Variable 2	+RE_G*	-RE_R*	+R_B*	+RE_R*	-B_NIR*	+G_NIR*	-NIR_B*
Variable 3	+[Part. Fe]*	+L_NIR*	-NIR_B*	-Turb**	+L_B*	+RE_R	+Turb*
AICc	-96.03	-2.54	-202.41	-169.45	153.02	-143.94	99.75
$R^2_{adjusted}$	0.99	0.90	0.99	0.80	0.99	0.77	0.96
Jarque-Bera p	0.11	0.10	0.45	0.93	0.23	0.57	0.12
Koenker p	0.14	0.21	0.12	0.16	0.27	0.03	0.16
Moran's I p	0.45	0.25	0.49	0.48	0.59	0.44	0.39
VIF	4.35	1.45	3.97	4.56	7.30	4.87	4.61

3.3.5 Optical Depth Interferences

Detecting substrate through a water column decreased the overall EM reflected and, more importantly, altered the overall spectral response (e.g., changes to peak reflectance wavelengths). Because it is impossible to separate individual OAC contributions to the response, some authors have used the peak reflectance wavelengths to develop meaningful relationships (Anderson and Robbins 1998; Roesler and Boss 2007; Matthews and Odermatt 2015; Gholizadeh et al. 2016; Jackisch et al. 2018). Accounting for this issue often requires empirically derived models with numerous in-situ measurements (e.g., OAC concentrations, absorption coefficients, bottom depth, and bottom albedo) (Albert and Gege 2006; Voss et al. 2003; Cannizzaro and Carder 2006).

By utilizing only sUAS-derived red band reflectance, in-situ measurements of SDD and AD, and the SDD to AD ratio allowed for the development of a method to identify optically shallow or regions impacted by other remote sensing interferences within ODWs. Using the SDD:AD ratio

and red band reflectance at each PTS transect (OD model) produced a moderately strong negative exponential relationship (R^2 = 0.73) (Figures 3.1d, 3.1f, and 3.4). The established exponential function (see equation in Figure 3.4), modeled after the Beer-Lambert law, represented the decay of spectral energy in water. Considering the OD model was developed from PTS with significantly different optical properties (e.g., red band reflectance), the agreement between the observed and predicted values, although small in sample size (n = 7), was encouraging (Figure 3.5). It appears the established methodology represents a reasonable approach to remotely evaluate a waterbody's potential for the application of sUAS technologies. Two spatial maps identifying the extent of remote sensing interferences (e.g., OSWs, algal blooms, surface debris, and shadows) demonstrate this application (Figures 3.6a and 3.6b). Neither sUAS mission was void of remote sensing interferences. However, nearly all sampling locations were in areas unimpacted by optical depth interferences (e.g., SDD: AD < 1.0). In future studies, optically complex waterbodies should first be evaluated with the OD model to assess the feasibility of employing remote sensing technologies for in-situ water quality monitoring.

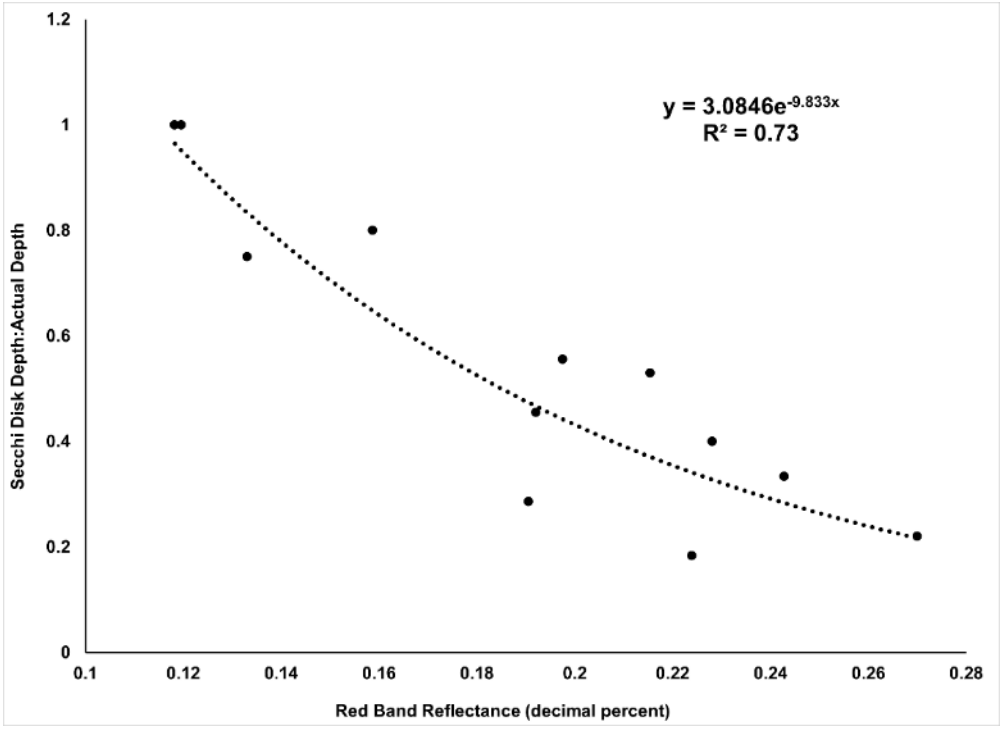

Figure 3.4 Exponential relationship developed with data from both PTS to identify portions of ODWs impacted by optical depth and other remote sensing interferences.

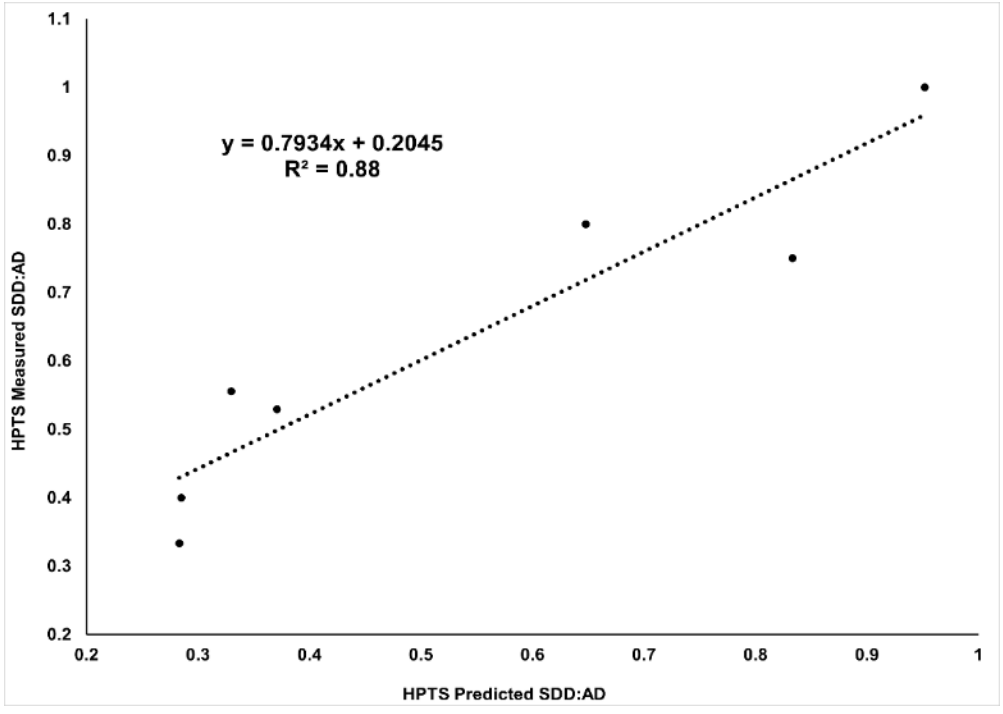

Figure 3.5 Relationship between observed and predicted Secchi disk depth (SDD) actual depth (AD) ratio at HPTS.

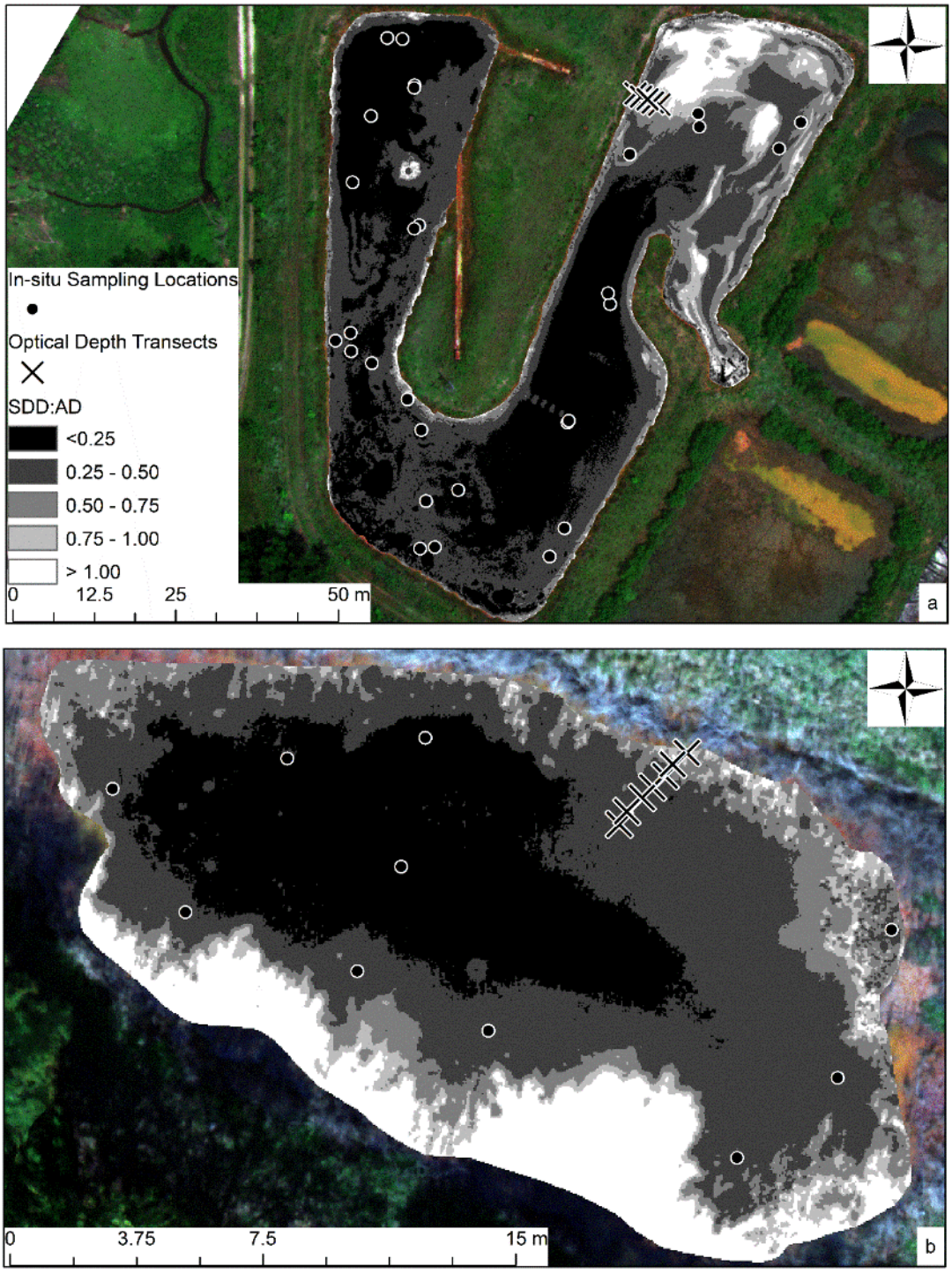

Figure 3.6 Remote sensing interference (e.g., OSWs) surfaces within the oxidation pond at MRPTS (a) and HPTS (b) developed with in-situ spectral measurements at the marked transect locations and applied to the entire pond using the Raster Calculator in ArcMap V. 10.6.1.

3.4 Conclusions

Remote sensing with sUAS can produce accurate and reliable surface-water quality models in ODWs with *prominent optical properties.* The exploitation of the natural (e.g., physical and chemical) relationships between various OACs allowed the development of non-optical metal models. When developed with PTS-specific reflectance and in-situ water quality, the results produced robust, unbiased, and accurate statistical models. Attempts to validate MRPTS models at HPTS suggest the models were somewhat site-specific. However, further research will be required to determine whether the limitation resulted from the applied models, chemical and physical relationships (e.g., sorption) in the ponds, or significant differences between the test and validation datasets. A statistically derived exponential relationship represents a methodology to remotely assess the feasibility of utilizing the technologies described herein to assess ODWs. Currently, due to the variability in accuracy, along with the lack of a standardized sUAS operating procedure and reporting criteria, these technologies should only be used as exploratory tools. This study expands on the current OACs that can be estimated remotely and demonstrates the benefits of incorporating sUAS technologies into traditional mine water monitoring efforts. With increased refinement, testing, and validation in additional forms of mine water, sUAS can be integrated with traditional monitoring efforts of mine drainage PTS. The systems and models discussed in this study may provide a reasonable alternative to in-situ surface water quality sampling and offer further insight into the nature of optically complex mine waters.

3.5 Future Work

The methodology presented herein should be tested in ODWs dominated by an OAC with different optical properties (e.g., As, Cu, Pb, and Zn hydroxides) on waters with lower OAC concentrations and commonly clear artesian source waters of mining-impacted environments. Alternative multispectral reflectance extraction techniques should be examined to determine which represents real-world conditions more accurately (Su and Chou 2015; Arango and Nairn 2020). If the ultimate goal is to minimize traditional in-situ sampling events and save time, money, and human hours, the widespread application requires the models to be refined with up-to-date water quality and reflectance measurements. Including data from each PTS in the model development phase could further refine and expand on the effective range of the models.

Acknowledgments

This work was supported by the Grand River Dam Authority (Agreements GRDA 060910 and GRDA 08272015). The authors appreciate the support from members of the Center for Restoration of Ecosystems and Watersheds (CREW), the additional spectral instrumentation provided by the Earth Observation and Modeling Facility (EOMF), and access to the property of private landowners.

Literature Cited

Albert A, Gege P (2006) Inversion of irradiance and remote sensing reflectance in shallow water between 400 and 800 nm for calculations of water and bottom properties. Applied Optics 45(10): 2331-2343. https://doi.org/10.1364/ao.45.002331.

Anderson J, Robbins E (1998) Spectral reflectance and detection of iron-oxide precipitates associated with acidic mine drainage. Photogrammetric Engineering and Remote Sensing 64(12) 1201-1208. ISSN: 0099-1112/98/6412-1201.

Arango J, Nairn R (2020) Prediction of optical and non-optical water quality parameters in oligotrophic and eutrophic aquatic systems using small unmanned aerial system. Drones 4(1): 1-21. https://doi.org/10.3390/drones4010001.

Bebbington AJ, Humphreys Bebbington D, Sauls LA, Rogan J, Agrawal S, Gamboa C, Imhof A, Johnson K, Rosa H, Royo A, Toumbourou T, Verdum R (2018) Resource extraction and infrastructure threaten forest cover and community rights. In: Berenbaum M (eds) Proceedings of the National Academy of Sciences. Vol. 52.United States of America, 13164-13173.

Becker RH, Sayers M, Dehm D, Shuchman R, Quintero K, Bosse K, Sawtell R (2019) Unmanned aerial system based spectroradiometer for monitoring harmful algal blooms: a new paradigm in water quality monitoring. Journal of Great Lakes Research 45(3):444-453. https://doi.org/10.1016/j.jglr.2019.03.006.

Bennett N, Croke B, Guariso G, Guillaume J, Hamilton S, Jakeman A, Marsili-Libelli S, Newham L, Norton J, Perrin C, Pierce S, Robson B, Seppelt R, Voinov A, Fath B, Andreassian V (2013)

Characterizing performance of environmental models. Environmental Modelling and Software 40:1-20. https://doi.org.10.1016/j.envsoft.2012.09.011.

Biber E (2013) The challenge of collecting and using environmental monitoring data. Ecology and Society 18(4):68. https://dx.doi.org/10.5751/ES-06117-180468.

Buczyńska A (2020) Remote sensing and GIS technologies in land reclamation and landscape planning processes on post-mining areas in the Polish and world literature. In: American Institute of Physics (AIP) Conference Proceedings. Vol 2209 040002-10. https://doi.org/10.1063/5.0000009.

Buters T, Bateman P, Robinson T, Belton D, Dixon K, Cross A (2019) Methodological ambiguity and inconsistency constrain unmanned aerial vehicles as a silver bullet for monitoring ecological restoration. Remote Sensing 11(10): 1180-1196. https://doi.org/10.3390/rs11101180.

Cannizzaro J, Carder K (2006) Estimating chlorophyll a concentrations from remote-sensing reflectance in optically shallow waters. Remote Sensing of the Environment 101(2006): 13-24. https://doi.org/10.1016/j.rse.2005.12.002.

Cress J, Hutt M, Sloan J, Bauer M, Feller M, Goplen S (2015) U.S. Geological Survey Unmanned Aircraft Systems (UAS) Roadmap 2014. U.S. Geological Survey Open-File Report 2015-1032:60. https://dx.doi.org/10.3133/ofr20151032.

Dekker A, Donze M (1994) Imaging spectrometry as a research tool for inland water resources analysis. In: Hill J and Megier J (eds) Imaging Spectrometry – a Tool for Environmental Observations, 4th vol. Springer, Dordrecht, pp 295-317.

Dekker A, Zamurović-nenad Ž, Hoogenboom H, Peters M (1996) Remote sensing, ecological water quality modelling and in-situ measurements: a case study in shallow lakes. Hydrological Science Journal 41(4): 531-547. https://doi.org/10.1080/02626669609491524.

ESRI (2018) Interpreting OLS results. Resource document ESRI. https://desktop.arcgis.com/en/arcmap/10.3/tools/spatial-statistics-toolbox/interpreting-ols-results.htm. Accessed 20 December 2020.

Fang Y, Hu Z, Xu L, Wong A, Clausi D (2019) Estimation of iron concentration in soil of a mining area from UAV-based hyperspectral imagery. In: Proceedings of the 2019 10th Workshop on Hyperspectral Imaging and Signal Processing: Evolution in Remote Sensing. Amsterdam, Netherlands, 1-5.

Federal Aviation Administration (FAA) (2016) Title 14: Aeronautics and Space | Part 107 – small unmanned aircraft systems. FAA. https://www.ecfr.gov/cgi-bin/text-idx?SID=dc908fb739912b0e6dcb7d7d88cfe6a7&mc=true&node=pt14.2.107&rgn=div5#se14.2.107_13. Accessed 29 June 2020.

Friedman S (1996) Map showing the distribution of underground mines in the Hartshorne and McAlester coals in the Hartshorne 7.5’ quadrangle, Pittsburgh and Latimer counties, Oklahoma. U.S. Geological Survey Open-File Report 7-96.

Gholizadeh M, Melesse A, Reddi L (2016) A comprehensive review on water quality parameters estimation using remote sensing techniques. Sensors 16(8): 1298-1340. https://doi.org/10.3390/s16081298.

Holl K (2002) Long-term vegetation recovery on reclaimed coal surface mines in the eastern USA. Journal of Applied Ecology 39(6): 960-970. https://doi.org/10.1046/j.1365-2664.2002.00767.x.

Holzbauer-Schweitzer B, Nairn R. (2020) Spectral monitoring techniques for optically deep mine waters. In: Pope J, Wolkersdorfer C, Sartz L, Weber A, Woldersdorfer K. (eds) Proceedings of the International Mine Water Association Congress. Christchurch, New Zealand, 110 – 117.

Jackisch R, Lorenz S, Zimmermann R, Möckel R, Gloaguen R (2018) Drone-borne hyperspectral monitoring of acid mine drainage: An example from the Sokolov Lignite District. Remote Sensing 10(3): 1-23. https://doi.org/10.3390/rs10030385.

Kokaly R, Clark R, Swayze G, Livo E, Hoefen T, Pearson N, Wise R, Benzel W, Lowers H, Driscol R, Klein A (2017) USGS Spectral Library Version 7: USGS Data series 1035, 61. https://doi.org/10.3133/ds1035.

LaBar J, Nairn R (2009) Evaluation of first 1.5 years of operation of a passive treatment system in SE Oklahoma. In: Barnhisel R (ed) Proceedings of the 2009 National Meeting of the American Society of Mining and Reclamation. Billings, MT, 693-708.

Lee Z, Carder K, Mobley C, Steward R, Patch J (1998) Hyperspectral remote sensing for shallow waters – A semianalytical model. Applied Optics 37(27): 6329-6338. https://doi.org10.1364/AO.37.006329.

Lee Z, Carder K (2002) Effect of spectral band numbers on the retrieval of water column and bottom properties from ocean color data. Applied Optics 41(12): 2191-2201. https://doi.org/10.1364/AO.41.002191.

Lee S, Choi Y (2016) Reviews of unmanned aerial vehicle (drone) technology trends and its applications in the mining industry. Geosystem Engineering 4: 197-204. https://doi.org/10.1080/12269328.2016.1162115.

Lim J, Choi M (2015) Assessment of water quality based on Landsat 8 operational land imager associated with human activities in Korea. Environmental Monitoring and Assessment 187(6): 4616. https://doi.org/10.1007/s10661-015-4616-1.

Martins W, Lima M, Barros Jr. U, Amorim S, Oliveira F, Schwartz G (2020) Ecological methods and indicators for recovering and monitoring ecosystems after mining: A global literature review. Ecological Engineering 145(15). https://doi.org/10.1016/j.ecoleng.2019.105707.

Marquardt D (1970) Generalized inverses, ridge regression, biased linear estimation, and nonlinear estimation. Technometrics 12(3): 591-612. https://doi.org/10.2307/1267205.

Matthews M, Odermatt D (2015) Improved algorithm for routine monitoring of cyanobacteria and eutrophication in inland and near-coastal waters. Remote Sensing of Environment 156: 374-382. https://doi.org/10.1016/j.rse.2014.10.010.

McKnight E, Fischer R (1970) Geology and ore deposits of the Picher field Oklahoma and Kansas. United States Geological Survey Professional Paper 588. 173 p.

Miles J (2005) Tolerance and Variance Inflation Factor. *Encyclopedia of Statistics and Behavioral Science*, https://doi.org/10.1002/9781118445112.stat06593.

Morel A (2005) Introduction to optical properties of the sea: Theoretical aspects: In: Babin M, Roesler C, Cullen J (eds) Real-time coastal observing systems for ecosystem dynamics and harmful algal blooms. UNESCO, Paris, pp 109-151.

Nairn R, LaBar J, Oxenford L, Shepherd N, Holzbauer-Schweitzer B, Arango J, Tang Z, Dorman D, Folz C, McCann J, Ingendorf JD, Stanfield H, Knox R. (2020) Toward sustainability of passive treatment in lecacy mining watersheds: operational performance and system maintenance In: Pope J, Wolkersdorfer C, Sartz L, Weber A, Woldersdorfer K. (eds) Proceedings of the International Mine Water Association Congress. Christchurch, New Zealand, 123 – 128.

Nairn R, LaBar J, Strevett K, Strosnider W, Morris D, Garrido A, Neely C, Kauk K (2010) Initial evaluation of a large multi-cell passive treatment system for net-alkaline ferruginous lead-zinc mine waters. In: Barnhisel R (ed) Proceedings of the 2010 National Meeting of the American Society of Mining and Reclamation. Pittsburgh, PA, 635-649.

Oklahoma Department of Environmental Quality (ODEQ) (2017) Tar Creek Superfund Site. Resource document ODEQ. https://www.deq.ok.gov/land-protection-division/cleanup-redevelopment/superfund/tar-creek-superfund-site/. Accessed 12 November 2020.

Palmer S, Kutser T, Hunter P (2015) Remote sensing of inland waters: Challenges, progress and future directions. Remote Sensing of Environment 157(2015): 1-8. https://doi.org/10.1016/j.rse.2014.09.021.

Park S, Choi Y (2020) Applications of unmanned aerial vehicles in mining from exploration to reclamation: a review. Minerals 10(663): 1-31. https://doi.org//10.3390/min10080663.

Petty M (2012) Calculating and using confidence intervals for model validation. In: Proceedings of the Fall 2012 Simulation Interoperability Workshop. Orlando, FL, 10-14.

Ren H, Zhao Y, Xiao W, Hu Z (2019) A review of UAV monitoring in mining areas: current status and future perspectives. International Journal of Coal Science and Technology 6(3): 320-333. https://doi.org/10.1007/s40789-019-00264-5.

Roesler C, Boss E (2007) In situ measurement of the inherent optical properties (IOPs) and potential for harmful algal bloom detection and coastal ecosystem observations. In: Babin M, Roesler C, Cullen J (eds) Real-time coastal observing systems for ecosystem dynamics and harmful algal blooms. UNESCO, Paris, pp 153- 206.

Salama M, Dekker A, Su Z, Mannaerts C, Verhoef W (2009) Deriving inherent optical properties and association inversion-uncertainties in the Dutch lakes. Hydrology and Earth System Sciences 13(7): 1113-1121. https://doi.org/10.5194/hess-13-1113-2009.

Seppelt R, Müller F, Schröder, Volk M (2009) Challenges of simulating complex environmental systems at the landscape scale: A controversial dialogue between two cups of espresso.

Ecological Modeling 220(24): 3481- 3498. https://doi.org/10.1016/j.ecolmodel.2009.09.009.

Shi K, Zhang Y, Qin B, Zhou B (2019) Remote sensing of cyanobacterial blooms in inland waters: present knowledge and future challenges. Science Bulletin 64(20): 1540-1556. https://doi.org/10.1016/j.scib.2019.07.002.

Sonter L, Moran C, Barrett D, Soares-Filho B (2014) Processes of land use change in mining regions. Journal of Cleaner Production 84(1): 494-501. https://doi.org/10.1016/j.jclepro.2014.03.084.

Su TC, Chou HT (2015) Application of multispectral sensors carried on unmanned aerial vehicle (UAV) to tropic state mapping of small reservoirs: A case study of Tain-Pu Reservoir in Kinmen, Taiwan. Remote Sensing 7(8): 10078-10097. https://doi.org/10.3390/rs70810078.

Su TC (2017) A study of a matching pixel by pixel (MPP) algorithm to establish an empirical model of water quality mapping, as based on unmanned aerial vehicle (UAV) images. International Journal of Applied Earth Observation and Geoinformation 58(2017): 213-224. https://doi.org/10.1016/j.jag.2017.02.011.

Torrent J, Barrón V (2002) Diffuse reflectance spectroscopy of iron oxides. Encyclopedia of Surface and Colloid Science (1): 1438-1446.

Trumbull J (1957) Coal resources of Oklahoma: United States Geological Survey Bulletin 1042-J, 305 – 383.

United States Geological Survey (USGS) (1996) 1995 National Oil and Gas Assessment Plays and 1995 National Oil and Gas Assessment ¼-mile cells within the 6200 Arkoma Basin Province. USGS Central Energy Resources Team. - https://certmapper.cr.usgs.gov/data/noga95/prov62/spatial/doc/prov62.xml. Accessed 10 January 2021.

Voss K, Mobley C, Sundman L, Ivey J, Mazel C (2003) The spectral upwelling radiance distribution in optically shallow waters Limnology and Oceanography 48(1): 364-373. https://doi.org/10.4319/lo.2003.48.1_part_2.0364.

Watts A, Ambrosia V, Hinkley E (2012) Unmanned aircraft system in remote sensing and scientific research: classification and considerations of use. Remote Sensing 4(6): 1671-1692. https://doi.org/10.3390/rs4061671.

Werner T, Mudd G, Schipper A, Huijbregts M, Taneja L, Northey S (2020) Global-scale remote sensing of mine areas and analysis factors explaining their extent. Global Environmental Change 60(2020): 1-10. https://doi.org/10.1016/j.gloenvcha.2019.102007.

Whitehead K, Hugenholtz C (2014) Remote sensing of the environment with small unmanned aircraft systems (UASs), part 1: a review of progress and challenges. Journal of Unmanned Vehicle Systems 2(3): 69-85. https://doi.org/10.1139/juvs-2014-0006.

Zeng C, Richardson M, King D (2017) The impacts of environmental variables on water reflectance measured using a lightweight unmanned aerial vehicle (UAV)-based spectrometer system. ISPRS Journal of Photogrammetry and Remote Sensing 130: 217-230. https://doi.org/10.1016/j.isprsjprs.2017.06.004.

Zhang Z, Li H, Cybele M, Dai W, Li Z (2019) Remotely sensed water reflectance measurements based on unmanned aerial vehicle (UAV). In: Chung J, Triantafyllou M, Langen I, Yao T (eds) Proceedings of the twenty-ninth 2019 International Ocean and Polar Engineering Conference. Honolulu, Hawaii, 614-619.

Chapter 4: In-situ Manipulations of Aquatic Optical Depth and its Effect on sUAS-Derived Spectral Reflectance

This chapter was formatted as a manuscript for submission to Remote Sensing of Environment.

Abstract:

The remote collection of spectral data (e.g., multi- and hyperspectral) with sensors fixed to various platforms (e.g., satellites, occupied aerial vehicles, and small unoccupied aerial systems (sUAS)) has allowed for the estimation of several optically active constituents (OACs) common in surface waters. However, in small, complex, and optically shallow waters where multiple OACs (e.g., chlorophyll-a and total suspended solids) impact the spectral signature, these technologies have experienced significant limitations. However, altering the scale at which these examinations are performed from surface waters (e.g., ponds, lakes, and reservoirs) to mesocosm systems will allow for a minute examination of the interactions between OACs and the impact of aquatic optical depth has on remotely sensed spectra. Thus, this study examines both optically shallow and optically deep water bodies at the mesocosm scale to determine the impact aquatic optical depth has on developing accurate surface-water quality models. Furthermore, the impact of bottom reflectance on the sUAS-derived spectral signature was described in two manners. Results demonstrated an accurate representation of OACs present in various forms and concentrations in optically deep mesocosms compared to optically shallow mesocosms when assessed with sUAS. Also, using an sUAS allowed for quantification of the effects of bottom reflectance. The interferences observed under these conditions (e.g., reflectance increased by 5 - 21 percent) were comparable to literature values when studying optically complex water bodies with hyperspectral data. Therefore, this study provides a basis for understanding the benefits and limitations of monitoring in-situ water quality via sUAS in optically deep and shallow waterbodies.

Keywords:

Ordinary Least Squares Regression; Mesocosm; Optically Active Constituents; Remote Sensing

4.1 Introduction

Inland aquatic ecosystems provide a range of goods and services (e.g., water and nutrient regulation, habitat and food provisioning, and recreational services) for humans and other organisms (MA 2005). For these systems to continue to provide the goods and services, their overall health (e.g., water quality) needs to be maintained and monitored. However, the chemical, physical, and optical properties of these environments can vary considerably, making it difficult to characterize the natural spatial and temporal variability with traditional methods (e.g., in-situ point monitoring) (Liu et al. 2003; Dörnhöfer and Oppelt 2016; Zeng et al. 2017; Seidel et al. 2020).

Many researchers have incorporated integrated in-situ and remote sensing data collection strategies to address some limitations of the current monitoring approach (Dall'Olmo and Gitelson 2005; Cannizzaro and Carder 2006; Larson et al. 2017; Zhou et al. 2017; Becker et al. 2019; Seidel et al. 2020). Incorporating existing (e.g., satellites) and developing remote sensing technologies (e.g., small Unoccupied Aerial Systems (sUAS)) has provided researchers the ability to measure spectra across entire aquatic ecosystems. Inherent optical properties (IOPs) of the water column and the optically active constituents (OACs) compose a majority of the reflected energy signal (e.g., reflectance) in optically deep waters (ODWs) (Liu et al. 2003; Voss et al. 2003; Cannizzaro and Carder 2006; Seidel et al. 2020). Utilizing the reflectance measured in the visible and near-infrared (VIS and NIR) spectra (e.g., 400 – 1000 nm) and observed in-situ water quality data have allowed for the retrieval and estimation of various OACs (e.g., chlorophyll-a (Chl-a), total suspended solids (TSS), Secchi disk depth (SDD)) in ODWs. These types of studies were successful because they documented OAC concentrations and the resulting spectral signature to

develop predictive surface water quality models (e.g., via various forms of regression) (Odermatt et al. 2012; Gholizadeh et al. 2016; Zhang et al. 2019; Seidel et al. 2020).

Alternately, in optically shallow waters (OSWs), reflectance can be impacted by the bottom substrate, the OACs present and their concentration, along with their IOPs, all of which vary among water bodies and are independent of one another (Liu et al. 2003; Odermatt et al. 2012; Palmer et al. 2015; Seidel et al. 2020). Researchers have developed algorithms to address some of these contributions (Gould and Arnone 1997; Voss et al. 2003; Cannizzaro and Carder 2006). Gould and Arnone (1997) partitioned bottom reflectance using a bio-optical model. The model required estimates of the water's IOPs (e.g., optical properties of water independent of illumination geometry), bottom depths, and albedos. Others have also used look-up tables, and neural network approaches to extract the IOPs, bottom depths, and bottom albedos from hyperspectral reflectance (e.g., hundreds to thousands of bands) data (Sandidge and Holyer 1998; Mobley et al. 2005). However, because most in-situ hyperspectral measurements are considered “point” measurements, they may not capture the spatial variation necessary to characterize a waterbody sufficiently (Seidel et al. 2020). Additional site-specific considerations (e.g., heterogeneity of OSWs) limit the use of empirically derived water quality models (Liu et al. 2003).

Furthermore, many studies examine a single OAC because discriminating individual OAC spectral signatures is complex and not well documented in the literature (Gholizadeh et al. 2016). Natural aquatic ecosystems rarely contain only one OAC (e.g., Chl-a), and in situations where multiple OACs were present, not all contribute to spectral reflectance equally (Liu et al. 2003). The OAC distribution (e.g., horizontal and vertical), density gradients (e.g., vertical), and light penetration

(e.g., SDD) within the water column have also presented concerns for remote sensing in OSWs. If the OACs form a layer outside the “detectable” water layer, the accurate estimation of OAC concentrations becomes unresolvable (Seidel et al. 2020). Thus, the accurate quantification of any OAC relies on the constituent's optical activity and whether interactions with other OACs alter its spectral signature (Liu et al. 2003). Before applying integrated remote sensing techniques in a waterbody, an understanding of OAC types and concentrations, along with any interactions among them, should be evaluated. Thus, in terms of real-world monitoring applications, these issues present a complex scientific question that has limited remote sensing in shallow inland waters with unique and ever-changing optical signatures.

The benefits of sUAS compared to satellite remote sensing (e.g., finer spatial resolution, custom revisit periods, and lower deployment costs) have been discussed in several reviews of remote sensing technologies (e.g., Whitehead and Hugenholtz 2014; Gholizadeh et al. 2016; Becker et al. 2019). One of the benefits frequently cited includes the spatial resolution of data produced by sUAS for evaluating small, shallow, inland waters, which were otherwise too small for satellite-derived imagery. Thus, a literature gap exists in that most studies examined full-scale waterbodies, likely to convey the results in a manner that promotes the widespread use of the technologies. However, to further understand the interactions between OACs, the impact of aquatic optical depth (OD) on remotely sensed spectra and to determine if sUAS imagery can describe these optically complex systems, a shift in scale is required. Specifically, an evaluation of mesocosm systems with varying types and concentrations of OACs which, appears to have been avoided in the literature. Thus, characterization of mesocosm optically complex waters by

exploiting the technological benefits of sUAS that many authors describe (e.g., pixel resolution) has not been achieved.

By examining both OSWs and ODWs, this study offers a stepping stone for real-world in-situ environmental remote monitoring with sUAS. Through careful examination of the mesocosm systems, the possibilities of integrated in-situ remote sensing techniques were demonstrated. Impacts on the measured spectral signature from detecting substrate through a water column were also examined. This study's objectives were two-fold: (1) document the presence of various OACs and the impact their concentrations had on sUAS-derived multispectral imagery and (2) determine how bottom reflectance alters the optical properties of the water column when examined with an sUAS in optically complex mesocosm scale systems. Therefore the two experimental hypotheses evaluated in this study were: (1) if actual depth exceeds the aquatic OD (e.g., ODW), the optical properties of the water column will represent the concentrations and types of OACs (e.g., total suspended solids, chlorophyll-a, and metals) in-situ when measured with sUAS, and (2) if detectable through a column of water (e.g., OSW) the electromagnetic (EM) signature of the substrate will be represented when measured with an sUAS. With the overall goal of documenting the effects that various optically complex mesocosm systems have on establishing accurate water quality models with sUAS-derived multispectral imagery.

4.2 Material and Methods

4.2.1 Study Site Description

The mesocosms examined in this study were constructed in northeastern Oklahoma (36.570, -94.964) at an aquatic plant nursery managed by the Grand River Dam Authority (GRDA). Initial setup required constructing six large (4 m long, 1.5 m wide, and 1 m deep) in-situ pseudo water

baths or boxes. These boxes were oriented in a north-south direction, minimizing variable illumination conditions, and were spaced approximately 2 meters apart to address the shading potential and provide easy access. Liners were installed in all boxes to moderate the mesocosms water temperature throughout the yearlong study (August 2019 – October 2020). For much of this study, a concurrent but unrelated mesocosm study with a similar setup was completed (Figure 4.1A).

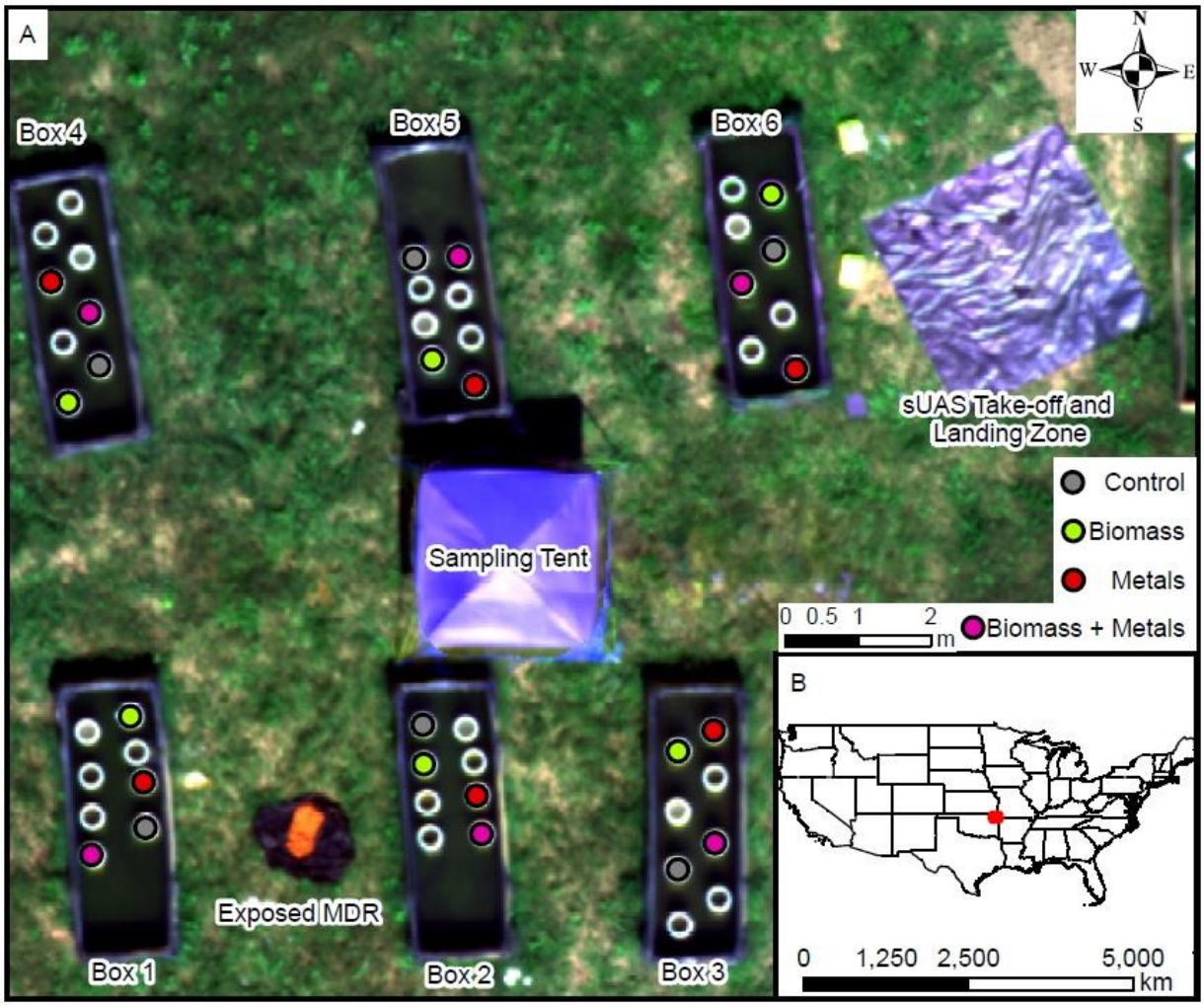

Figure 4.1 (A) Study site setup at managed aquatic nursery, showing box orientation, locations of each vessel studied, the sUAS flight pad (take-off and landing zone), and the sampling tent which was used for protection against the elements (e.g., heat). Vessels not identified were part of a concurrent study unrelated to this experiment. (B) Location of study site (e.g., red dot) within Oklahoma and the continental United States of America.

4.2.2 Mesocosm Setup

The mesocosms in this study consisted of four types of vessels (e.g., 19-L buckets), each replicated six times. The four vessel types examined were identified as control (C), biomass (B), metals (M), and biomass plus metals (BM). Each vessel contained approximately 5 kg of substrate. This study explored two substrate types, the first of which (soil) was sourced from the study location and placed in each of the C and B vessels. The second substrate was sourced from a mine drainage passive treatment system (Mayer Ranch Passive Treatment System) in Miami, Oklahoma. The substrate was the result of iron oxidation and precipitation (mine drainage residuals (MDR)) (for detailed information, see Tang and Nairn 2021). The only substrate in the M vessels was MDR. Substrate within the BM vessels consisted of a mixture of approximately 50 percent soil and 50 percent MDR by weight (Figures 4.2A and 4.2B).

Water from a nearby surface water pond was added to the boxes via pumping. Using a 1-L graduated cylinder and the same water supply (stock water) to fill the vessels minimized substrate resuspension. Algal growth was promoted in the B and BM vessels by adding approximately 0.5-L of water from a wastewater lagoon (dosing water) in Commerce, Oklahoma (Table 4.1). Vessels were then randomly assigned a box (e.g., 1-6) and a location within the box (Figure 4.1A). Placing vessels atop a cinderblock ensured they were insulated by the water bath and shadows were minimized.

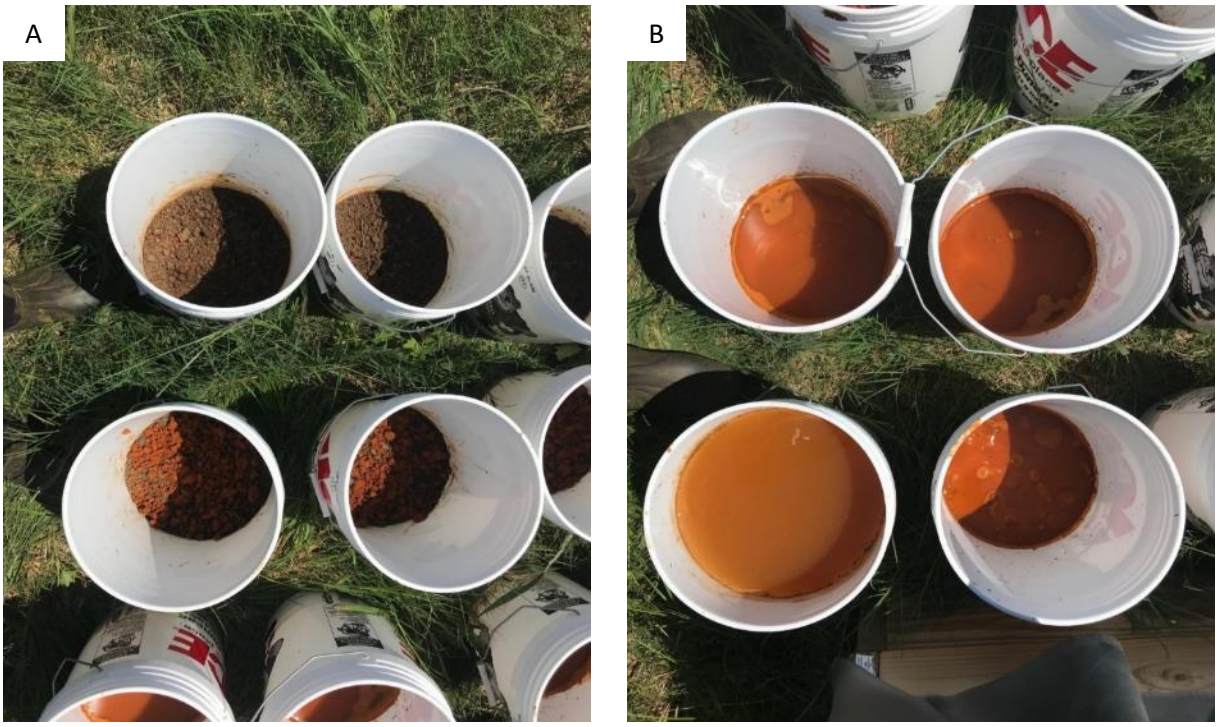

Figure 4.2 Vessels with soil (e.g., B - top vessels) and MDR (e.g., BM - middle vessels) substrate in place. (B) BM (e.g., middle) and M (e.g., bottom) vessels partially filled with water prior to being placed in their respective boxes.

Table 4.1 Mean water quality data for waters used during mesocosm setup; Hazen Units (HU), Total Nitrogen (TN), Total Phosphorus (TP); dosing water data sourced from Arango and Nairn (2020), which did not examine the same parameters as this study, thus (-) indicates the parameter was not quantified; n = 4 and 11 for stock and dosing water, respectively.

	Chl-a (ug L^{-1})	**TSS (mg L^{-1})**	**Color (HU)**	**Total Fe (mg L^{-1})**	**TN (mg L^{-1})**	**TP (mg L^{-1})**
Stock water	3.27	8.65	73.25	0.08	-	-
Dosing water	358.30	65.33	-	-	12.47	3.33

4.2.3 In-situ Water Quality Sampling and Analyses

In-situ surface water quality sampling was completed pre- and post-mixing. The sampling efforts included OACs frequently cited in sUAS-based remote sensing literature (Chl-a, TSS, and SDD) (Dall'Olmo and Gitelson 2005; Cannizzaro and Carder 2006; Larson et al. 2017; Zhou et al. 2017; Becker et al. 2019; Seidel et al. 2020), and those less commonly examined (metal concentrations

and color) (Rostom et al. 2017). Additional ancillary data collected included various weather parameters (air temperature, relative humidity, wind speed, and precipitation via a rain gauge). Section 4.2.6 Data Collection Schedule and Experimental Design provides a detailed description of the field data collection schedule for this study.

From each vessel, approximately 1-L of water was removed during each sampling event (e.g., pre-mixing). All aqueous samples were collected near the middle of the water column with a peristaltic pump at the lowest setting (e.g., 120-mL min^{-1}). A 250-mL sample bottle was filled and preserved with approximately 2-mL of trace metal grade nitric acid (e.g., pH < 2) for total metal analyses. Following the same procedure, the collection of a second 250-mL bottle filled with water passed through a 0.45 µm groundwater filter allowed for quantification of the dissolved metal fraction. These samples were analyzed within the six-month hold-time following USEPA Methods 3015A and 6010C (2007 and 2007)). Chl-a concentrations were quantified by collecting a 100-mL sample and immediately storing it on ice and away from light. Samples were then immediately returned to the laboratory and analyzed following the non-acidic USEPA Method 445.0 (1997). An additional 250-mL sample was collected, stored on ice, and analyzed for TSS following ASTM Standard Method 2540D (1997). A final 60-mL sample was collected for color determinations. Unpreserved, these samples' hold time was only 48 h. Therefore, analysis occurred upon returning to the laboratory or the morning of the next day following USEPA Method 147A (2016). Throughout each sampling event, at least three turbidity measurements (if all within ±10 percent) were obtained from each vessel using a portable turbidimeter following USEPA Method 180.1 (1993). After collecting all aqueous samples, the peristaltic pump was used to introduce water into the bottom of a 1.5-m transparency tube used for in-situ SDD

determinations. A multiparameter data sonde quantified additional water quality parameters (specific conductance, pH, and dissolved oxygen). Finally, the physical depth was measured with a weighted tape measure before moving to the next vessel and repeating the sampling process.

In total, four in-situ sampling events were completed. The initial sampling event took place two days after setup. It was intended that this event serve as the first pre-mixing event (e.g., OSWs). However, the resulting SDD measurements characterized all of the vessels as ODWs. Two additional events involved sampling every vessel pre- and post-mixing. Due to logistical limitations, a partial event was completed with a randomly selected sample of all the vessels (e.g., three of each type for pre- and post-mixing). The resulting sample number (n) for each pre-mixing vessel was 15. Post-mixing n for C, B, M, and BM was 21, 21, 19, and 20, respectively. The M and BM vessels had slightly lower n for several reasons. Sampling limitations began in March of 2020 as the global SARS-CoV-2 (e.g., COVID-19) pandemic restricted research efforts (e.g., limits on personnel, laboratory, and fieldwork) until the summer of 2020. This unexpected delay in sampling resulted in abandoning two of the M vessels and one of the BM vessels due to natural conditions (e.g., floated off cinderblock, filled with vegetation, or little to no water present).

4.2.4 Spectral Data Collection, Processing, and Extraction

An Aerial Technologies International (ATI) AgBot equipped with a MicaSense RedEdge sensor was the specific sUAS utilized in this study. The sensor simultaneously captured spectral reflectance in five discrete bands with center points in the blue (475 nm), green (560 nm), red (668 nm), rededge (717 nm), and NIR (840 nm) portions of the spectrum. Using the AgBot's autonomous capabilities (e.g., missions developed with MissionPlanner V. 1.6.67) removed the human aspect of flight and allowed for a single mission to be repeated, thus directly comparing reflectance

values. A typical mission's operational parameters included a flight altitude of 50 m above ground level, a flight speed of 5 m s^{-1}, with image overlap and sidelap set to 80 percent. Using these parameters produced an accurately georeferenced orthomosaic of the study site with a pixel resolution of approximately 3.40 cm per pixel. To keep cloud cover and glint to a minimum spectral data were collected nadir ± 2 hr of local solar noon.

Raw sUAS multispectral imagery was geolocated, radiometrically corrected, and mosaiced to produce spectral reflectance rasters with PIX4DMapper Pro V4.3.9. Although few custom processing options were available, this software provides the user with high-quality results with minimal input requirements. An image of a calibrated reflectance panel was captured immediately before takeoff and after landing, which accounted for changes to the flight's illumination conditions.

Reflectance was manually extracted from each vessel, avoiding any potentially mixed pixels, glint, or shading. Median values were extracted from the nine most central pixels (Figure 4.3). These pixels were those most likely unaffected by remote sensing interferences (e.g., mixed pixels, glint, and shading). The extraction procedure was completed in ESRI ArcMap V. 10.6.1 by creating a 24-polygon feature class to extract the pixel values from each mission (e.g., pre- and post-mixing) reflectance raster. Using the Raster to ASCII tool and Microsoft Excel, the reflectance data was organized, processed, and added to the appropriate datasets. The two substrates were purposefully left exposed so the sUAS could simultaneously measure their spectra. Pixels within the substate's extent were identified and extracted randomly to ensure representation of the variability.

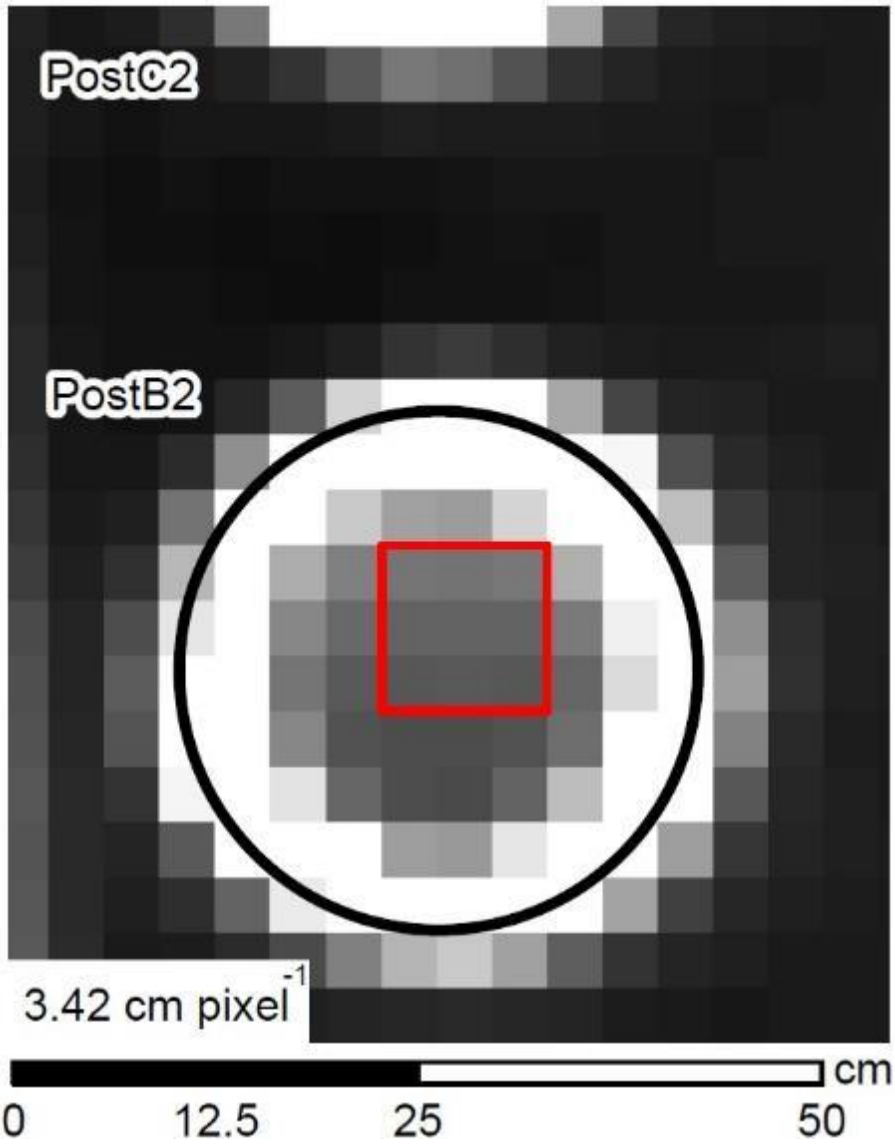

Figure 4.3 Example reflectance extraction technique performed for each vessel (e.g., PostB2) and raster (e.g., blue) throughout the study; the adjacent vessel (e.g., PostC2) was shown to provide information on spacing; the black circle and white squares represent the extent of the vessel (e.g., edge of 19-L bucket); the red square represents the nine pixels extracted; glint resulted in mixing of pixels near the edge of the vessels.

4.2.5 Substrate Spectral Analysis

Spectral angle mapping (SAM) provided a metric to quantify the effect of remote sensing substrate through OSW columns. SAM is a classification method that utilizes a theta (Θ) angle to determine the spectral similarity between measured and reference spectra. The Θ angle

represents the spectral similarity between two objects symbolized as vectors in a color space whose dimensions were equal to the number of bands used in the analysis (Van der Meer 1997; Torrent and Barrón 2002; Williams et al. 2002; Hamza et al. 2016). In this study, the sUAS collected spectral information from three bands within the RGB/VIS color space (e.g., blue, green, and red). These bands allowed for the calculation of the dot product (Eq. 1). Then similarities (e.g., Θ angles) were calculated using the arc-cosine of the dot product. Like Williams et al. (2002), when two objects were spectrally similar to the reference, the dot product was approximately equal to 1, and low (e.g., < 10 degrees) Θ angles were observed. Comparing two spectrally dissimilar objects produced dot products less than one and Θ angles greater than 10 degrees. Theta angles were symbolized in a three-dimensional space with axes representing median reflectance values from all events for each band (e.g., RGB). (Hamza et al. 2016). These data represent the total amount of spectral energy reflected from each object and the spectral difference within the VIS spectrum remotely sensed by the sUAS.

$$\theta = cos^{-1} \frac{sample\ reflectance * reference\ reflectance}{\|\overrightarrow{sample\ reflectance}\| * \|\overrightarrow{reference\ reflectance}\|} \quad \text{(Eq. 1)}$$

4.2.6 Data Collection Schedule and Experimental Design

The most important and controllable portion of this study was the experimental design. This study operated on the assumption that SDD could be used as a surrogate to identify aquatic OD. In other words, if the actual depth of water exceeded the SDD and the bottom substrate was not visible, vessels were considered to be ODW. Conversely, if the SDD exceeded the vessel's actual water depth, it was characterized as an OSW. Controlling the physical depth of water within the vessels while manipulating aquatic OD via mixing was vital. Mixing was completed using a 40 cm mixing paddle with a 6 cm impellor and a cordless 9.6V battery-powered drill (maximum rotations

per minute (RPM) of 750). Mixing occurred within the bulk (e.g., center) of the water column, at maximum RPM for approximately 15 – 20 s or until the substate was no longer visible. Examples of vessels pre- and post-mixing are presented in Figures 4.4A and 4.4B. For the remainder of this manuscript, vessels and their respective models will be identified by the treatment (e.g., pre-mixing), type (e.g., C), and if necessary, replicate (e.g., box) number (e.g., PreC1). To identify the models more precisely, each includes the suffix of the modeled OAC (e.g., PreCChla).

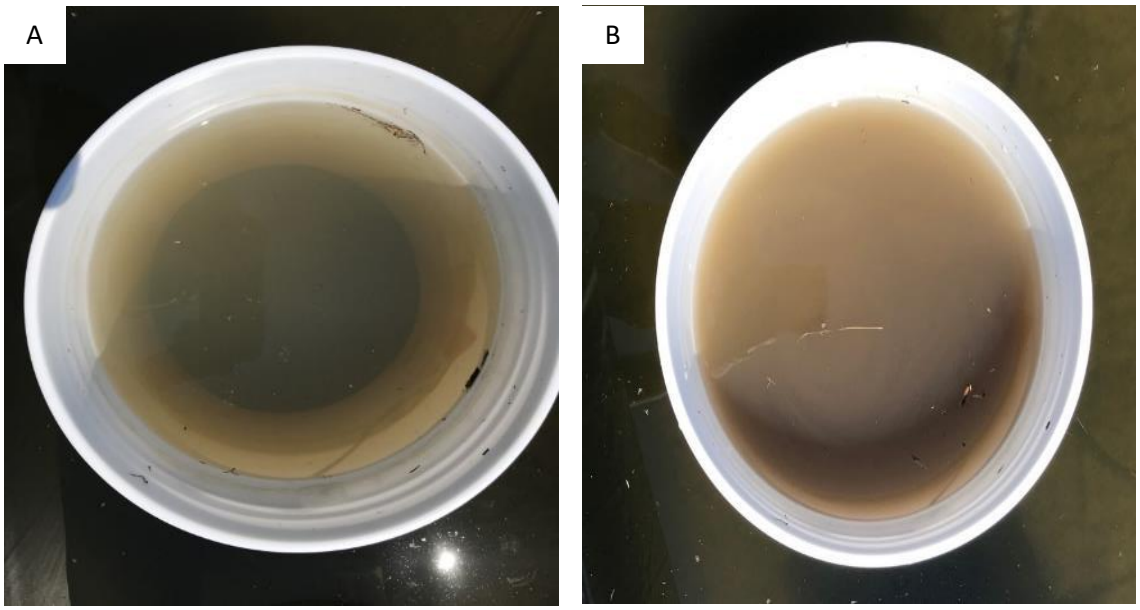

Figure 4.4 (A) PreB2 with substrate visible through water column containing 3.83 mg L-1 of TSS, a turbidity of 31.20 nephelometric turbidity units (NTU), an SDD equal to 37 cm (physical depth was 23.50 cm) and an apparent color of approximately 200 Hazen units (H.U). (B) PostB2 with substrate no longer visible containing 123.33 mg L^{-1} of TSS, a turbidity of 376.50 NTU, an SDD equal to 9 cm (physical depth was constant) and an apparent color equal to approximately 496 H.U. Shading was present but minimal in each vessel, Figure 4.3 demonstrates how this interference was avoided.

Each data collection effort adhered to the following sampling protocol: (1) performed in-situ water quality sampling – removing water from the vessels, (2) collected actual and aquatic OD measurements, (3) acquired sUAS-derived multispectral imagery, (4) mixed vessels (e.g., convert

from OSW to ODW), (5) acquired sUAS-derived multispectral imagery, (6) collected actual and aquatic OD measurements, (7) performed in-situ water quality sampling – removing more water from the vessels. Reestablishment of pre-sampling water levels (e.g., approximately 75 percent full) occurred after completing in-situ efforts.

4.2.7 Statistical Analyses and Justification

To assess if mixing caused significant increases in OAC concentrations and reflectance, a one-tailed Mann-Whitney U-Test was performed with band-specific reflectance from each set of vessels (e.g., pre- and post-mixing C blue band) and an alpha equal to 0.05. If significant (p-value < 0.05), results suggest mixing significantly increased median values of measured OAC concentrations and reflectance. This test was selected because the datasets exhibited non-normal distributions, unequal variances, and different sample sizes.

Exploratory regression was used as a preliminary data mining tool when all the factors contributing to the relationship between two variables were unknown (ESRI 2018a). In this study, exploratory regression evaluated all combinations of the explanatory variables (e.g., multispectral bands or band ratios). This analysis produced models that fulfilled the requirements and assumptions of ordinary least squares (OLS) regression. Explanatory (independent) variables consisted of each band (blue, green, red, rededge, NIR), band ratio (e.g., blue:green), and the log-transformed value of both. This number (50) of explanatory variables resulted in over 20,000 trials (sets of explanatory variables) that attempted to describe the OAC in question accurately and precisely. This approach was pursued because all the factors contributing to the relationships between OACs and multispectral reflectance were unknown and were not known a priori.

Correctly specified models met or exceeded the set criteria, meaning all explanatory variables were statistically significant, exhibited a justifiable relationship with the dependent variable, and were not redundant (e.g., variance inflation factor (VIF) < 7.5). Furthermore, the residuals produced by these models exhibited a normal distribution, suggesting no significant bias in the outputs (e.g., Jarque-Bera p-value > 0.10). Thus, to satisfy these conditions, the exploratory regression criteria included an adjusted R squared ($R^2_{adj.}$) greater than 0.65, a Jarque-Bera p-value above 0.10, a VIF below 7.50, and each explanatory variable must have made a significant (p-value < 0.05) contribution to the model. In many cases, numerous sets of explanatory variables satisfied these requirements. Therefore, the "best" models were those with the greatest $R^2_{adj.}$. If $R^2_{adj.}$ was similar, models with the lowest Akaike Information Criterion (AICc) and VIF values were given priority. In the event no models satisfied the criteria, those chosen for evaluation produced the highest $R^2_{adj.}$. The modeling tools available in ESRI ArcMap V. 10.6.1 were utilized to complete this exercise (ESRI 2018b; ESRI 2018c). In total, 20 different sets of pre- and post-mixing models (e.g., five OACs examined for each of the four types of vessels pre- and post-mixing) were selected for evaluation.

A partial F-Test provided an assessment of the condition (mixing) and if it altered the relationship (regression constants and coefficients) between in-situ OAC concentrations and multispectral reflectance. Establishing a conditional variable for the pre- and post-mixing datasets (zero and one, respectively) allowed for a statistical description of the changes in pre- and post-mixing regression constants (e.g., intercept). Furthermore, to determine if manipulating OD altered the response (e.g., slopes) of the dependent variable to the independent variables, an interaction term was included in the analysis. This interaction term was the product of the condition (e.g.,

mixing) and multispectral reflectance of one of the bands included in the respective regression model. If significance (p-value < 0.05) was observed for either the condition (e.g., mixing) or interaction effect (e.g., the effect of mixing on multispectral reflectance) this indicated that manipulating in-situ OD affected the relationship between the inputs and outputs statistically (Frost 2020).

If the partial F-test did not produce significant results, the relationships examined were consistent and comparable for OSWs and ODWs. If significant differences were observed, the relationships were not consistent, making the statistical comparison more related to how mixing alters the relationships observed, rather than addressing whether the spectra of OACs were represented more in ODWs than OSWs when measured with sUAS. Calculation of additional metrics allowed for a more robust examination of the model's fit, which was necessary due to the variability of the datasets and the nature of $R^2_{adj.}$. These metrics included the mean absolute error (MAE), standard error of the regression (SE), relative percent difference (RPD), and the sum of the squared errors (SSE), which assisted in evaluating the first experimental hypothesis.

4.3 Results and Discussion

4.3.1 In-Situ Water Quality

Observed water quality varied significantly (p-value < 0.05) for all OACs examined when comparing pre- and post-mixing concentrations. Evaluating the relationship between all TSS and turbidity values produced a correlation coefficient (R) of 0.79. When examined separately, the relationships diminished (e.g., 0.57 and 0.32) for pre- and post-mixing datasets, respectively. The post-mixing R was lower because particles immediately began to settle after mixing. However, when comparing the apparent color (e.g., perceived color resulting from particulates and

turbidity) to the TSS, the post-mixing data were more strongly correlated than pre-mixing (e.g., 0.74 and 0.63, respectively). Overall, the most robust relationship (R = 0.82) observed was among color and turbidity in the pre-mixing dataset.

The ranges and number of OACs examined in this study differ from typical remote sensing studies (Table 4.1). Cannizzaro and Carder (2006) estimated Chl-a concentrations ranging from 0.026 – 20.6 µg L^{-1} (n = 451) in shallow oceanic waters off Florida's coast. With this range, the authors classified the data as OSWs and ODWs and developed two separate models to explain this variability. Su (2017) employed sUAS remote sensing techniques to characterize concentrations of several OACs (e.g., Chl-a, SDD, and turbidity) in four separate water bodies. Chl-a concentrations evaluated were comparable to this study (e.g., 111-325 µg L^{-1}). However, the author presented separate models for each waterbody, with one requiring two models. The reported R^2 values ranged from 0.00 to 1.00 for Chl-a when estimated with the NIR:red ratio in ODWs. Larson et al. (2017) examined TSS concentrations in a portion of the Maumee River in Toledo, Ohio. These authors collected 21 surface (e.g., 0 - 15 cm) samples with a median TSS concentration of 55.0 mg L^{-1}. Using an sUAS similar to this study, the authors report an $R^2_{adj.}$ of 0.32, and note applications of sUAS-derived multispectral imagery were optimized (e.g., highest $R^2_{adj.}$ observed) at a water depth of approximately 91 cm. Overall, a study completed by Dall'Olmo and Gitelson (2005) provided comprehensive water quality examination (e.g., Chl-a, SDD, TSS, and turbidity) but only focused on estimating Chl-a concentrations with various combinations of hyperspectral bands.

Few studies have explored the capability of remote sensing techniques to estimate nontraditional OACs (e.g., metal concentrations). One such study examined various metal concentrations in

Mariout Lake, located in northern Egypt (Rostom et al. 2017). This study reported relatively high R values ranging from 0.27 – 0.97 considering the observed mean concentrations of 0.1 and 0.036 mg L^{-1} for Zn and Cu, respectively (n =22). Surprisingly, Fe was readily estimated (R^2 = 0.87) with reflectance from a single wavelength (e.g., 366 nm). However, the authors provide no further evaluation of the models fit, nor how the models were developed. Using hyperspectral data to model in-situ water quality requires managing the inherent collinearity and noise present when applying hyperspectral remote sensing in optically complex waters (Seidel et al. 2020).

Table 4.2 Summary water quality data for the OACs examined by treatment (e.g., pre- and post-mixing) and type (e.g., C, B, M, and BM); Minimum (Min), median (Med), and maximum (Max) values and units presented; Hazen Units (HU); All values were statistically different (p-value < 0.05) when comparing treatments (e.g., PreC and PostC) with one-tailed Mann-Whitney U Test.

		PreC	PostC	PreB	PostB	PreM	PostM	PreBM	PostBM
Chl-a (ug L^{-1})	Min	0.09	2.65	0.20	2.09	0.05	0.94	0.20	1.32
	Med	0.73	22.81	0.74	27.46	2.73	21.75	3.53	22.43
	Max	3.91	220.72	33.60	106.95	93.62	178.86	24.46	199.76
TSS (mg L^{-1})	Min	0.86	39.00	0.14	32.50	0.14	17.50	0.71	13.13
	Med	5.86	104.00	2.80	100.50	2.29	42.00	2.29	40.75
	Max	15.40	330.00	18.20	272.67	16.40	129.00	10.40	145.00
SDD (cm)	Min	11	5	16	6	12	1	13	4
	Med	25	8	25	10	25	12	24	13
	Max	47	27	37	26	26	19	26	17
Color (HU)	Min	9.60	75.30	7.10	35.10	4.90	52.20	4.50	56.90
	Med	41.70	269.60	47.90	131.30	11.20	136.60	17.50	130.70
	Max	658.40	1021.30	356.50	815.90	144.10	353.60	121.40	237.80
Total Fe (mg L^{-1})	Min	0.02	0.83	0.04	0.53	0.03	5.17	0.04	3.90
	Med	0.16	2.41	0.21	1.71	0.18	15.64	0.19	16.95
	Max	3.24	8.22	2.18	4.93	3.23	104.68	2.19	37.03

4.3.2 Multispectral Reflectance

The multispectral reflectance measured across all bands was not significantly different (p-value > 0.05) when comparing pre- and post-mixing C and B vessels. Conversely, the only bands that did not exhibit a significant difference (p-value > 0.05) for the M and BM vessels were the blue

and NIR bands (Table 4.2). Reflected NIR energy was not significantly different because water strongly absorbed NIR energy, causing a shift from lower (e.g., green) to higher (e.g., red) wavelengths (Shah et al. 2020). However, the peak reflectance measured for the C and B vessels was from the NIR band. NIR energy can help distinguish between physically shallow and deep waters (e.g., bathymetry) because between 0.3 and 0.9 m, NIR energy can be readily absorbed (Shah et al. 2020). Studies have also used NIR energy to develop single band (Shafique et al. 2003) and band ratio (Larson et al. 2018) relationships with TSS, suggesting the high NIR values observed were the result of interactions with the bottom substrate (PreC and PreB vessels) and substrate in solution (e.g., TSS) (PostC and PostB). The statistical difference between pre- and post-mixing TSS values should have also resulted in significantly different reflectance values. The lack of significant differences supports that NIR reflectance measured from the pre-mixing vessels resulted from interactions with the bottom substrate.

Median blue band reflectance was the lowest across all vessels and bands. Interestingly, when the substrate was soil (e.g., C and B vessels), pre-mixing vessels reflected more blue EM energy. When MDR was the substrate, post-mixing vessels reflected more blue energy. Gholizadeh et al. (2016) state that in clear waters, the maximum light penetration at 475 nm (e.g., RedEdge sensor blue band center point) can be as deep as 55 m and as shallow as 60 cm when TSS concentrations approach 400 mg L^{-1}. Jensen (1989) and Shah et al. (2020) support this by stating that if OAC concentrations were low, the optimum wavelength range to assess bathymetric properties is 440 – 540 nm. Within a similar spectral region (e.g., 450 – 600 nm), bottom reflectance has been shown to significantly increase (e.g., approximately 20 percent) reflectance values measured

(Cannizzaro and Carder 2006; Zeng et al. 2017). These factors suggest the blue band reflectance resulted from interactions with the substrate and TSS.

Green and red band reflectance were significantly different for the M and BM vessels due to the MDR's visual prominence in both. The PreM and PreBM green band reflected the least amount of EM energy compared to the rest of the vessels and as much or more red EM energy than other vessels. Fundamental EM interactions indicate that a body of water exhibiting the color red reflects more red EM energy while absorbing green EM. Furthermore, the intended use of the RedEdge sensor was to examine Chl-a in terrestrial ecosystems. Thus, the rededge band was centered where Chl-a absorbs the most EM (e.g., approximately 717 nm). As already mentioned, the increased particulates in solution (e.g., TSS) and interactions with substrate also caused the spectra to shift from green to red wavelengths. This shift's magnitude was important because Anderson and Robbins (1998) found iron precipitates (e.g., MDR) to have a mean peak reflectance near 650 nm. In theory, vessels containing MDR should have had a peak reflectance in the red band (e.g., 668 nm). However, observed peak reflectance occurred in rededge (e.g., 717 nm). Suggesting the various types and abundance of OACs could have caused a shift of approximately 49 nm.

Table 4.3 Summary sUAS-derived multispectral reflectance by treatment (e.g., pre- and post-mixing) and type (e.g., C, B, M, and BM); Minimum (Min), median (Med), and maximum (Max) values presented as decimal percent; statistical differences identified with Mann-Whitney U-Test (p-value < 0.05) and symbolized as bolded values.

		PreC	PostC	PreB	PostB	PreM	PostM	PreBM	PostBM
Blue	Min	0.016	0.024	0.015	0.025	0.015	0.024	0.014	0.025
	Med	0.054	0.042	0.051	0.043	0.024	0.034	0.024	0.031
	Max	0.076	0.085	0.084	0.081	0.059	0.051	0.064	0.050
Green	Min	0.022	0.026	0.023	0.029	**0.026**	**0.031**	**0.024**	**0.033**
	Med	0.084	0.068	0.083	0.069	**0.048**	**0.085**	**0.049**	**0.069**
	Max	0.105	0.138	0.110	0.124	**0.086**	**0.147**	**0.097**	**0.145**
Red	Min	0.024	0.032	0.022	0.017	**0.026**	**0.042**	**0.030**	**0.047**
	Med	0.090	0.075	0.084	0.076	**0.071**	**0.151**	**0.074**	**0.140**
	Max	0.101	0.156	0.106	0.141	**0.098**	**0.291**	**0.111**	**0.293**
Rededge	Min	0.037	0.042	0.043	0.049	**0.060**	**0.058**	**0.049**	**0.074**
	Med	0.091	0.090	0.095	0.090	**0.107**	**0.159**	**0.110**	**0.159**
	Max	0.111	0.183	0.110	0.167	**0.130**	**0.328**	**0.141**	**0.335**
NIR	Min	0.061	0.071	0.064	0.074	0.080	0.055	0.067	0.055
	Med	0.101	0.094	0.100	0.090	0.098	0.103	0.106	0.108
	Max	0.126	0.230	0.125	0.197	0.131	0.277	0.152	0.270

4.3.3 Remote Sensing in Optically Complex Waters

If the presence and concentrations of OACs were represented in the optical properties of ODWs, the post-mixing OLS models would reflect this. Specifically, post-mixing models will be capable of describing greater variability (e.g., higher $R^2_{adj.}$) or produce more accurate estimations of the OAC in question when evaluated with additional statistical metrics (e.g., RPD, MAE, SE, and SSE). However, to ensure the pre- and post-mixing OLS models were consistent and comparable, only models that were not significantly different (e.g., partial F-test) were compared and discussed in the context of this study. For example, significant differences in the models' slopes suggest the condition (e.g., mixing) altered the relationship between reflectance and in-situ OAC concentrations. Overall, nine of the twenty sets of models evaluated did not have significantly different regression constants and slopes (Table 4.3).

Table 4.4 OLS models evaluated that were not significantly different (p-value > 0.05; Partial F-Test), bolded values indicate the OLS selection criteria were exceeded; units of MAE and SE presented in units of the model parameter (e.g., µg L^{-1}, cm, mg L^{-1}, mg L^{-1}, and Hazen units for Chl-a, SDD, Fe, TSS, and color, respectively); SEE presented in squared units of the model parameter.

	R^2_{adj}	Koenker p-val	Jarque-Bera p-val	VIF	AICc	RPD (%)	MAE	SE	SSE
PreCChl-a	0.79	1.27E-01	0.91	**47.78**	30.61	41.82	0.30	0.45	2.22
PostCChl-a	0.53	8.54E-02	0.11	4.90	220.02	80.70	26.00	36.31	22412.17
PreBChl-a	0.84	1.49E-01	0.10	4.62	91.28	-126.74	2.22	3.40	127.05
PostBChl-a	0.90	7.52E-01	0.68	5.20	-8.81	26.22	0.12	0.39	2.60
PreBSDD	0.74	2.74E-01	0.59	**494.88**	87.83	8.38	2.06	3.03	100.95
PostBSDD	0.69	5.27E-02	0.15	3.79	117.80	18.27	2.04	3.18	172.36
PreBFe	0.72	3.44E-01	0.65	4.82	29.03	-67.99	0.30	0.43	2.00
PostBFe	0.85	7.90E-02	0.27	3.41	37.34	15.82	0.31	0.47	3.74
PreMTSS	0.89	1.16E-01	0.52	4.58	63.27	146.74	0.94	1.34	19.64
PostMTSS	0.80	9.44E-01	0.10	5.96	13.09	24.50	0.14	0.84	10.63
PreMColor	0.66	5.03E-01	0.13	3.12	148.54	78.28	14.47	22.92	5776.65
PostMColor	0.52	5.68E-01	0.03	5.28	10.37	27.75	0.13	0.41	2.54
PreMFe	0.54	7.81E-01	0.64	4.74	28.43	63.03	0.50	1.56	26.74
PostMFe	0.71	9.44E-01	0.16	3.14	6.03	32.35	0.15	0.58	5.10
PreBMChl-a	0.70	1.12E-01	0.50	**173.87**	90.90	-36.54	2.44	3.36	123.86
PostBMChl-a	0.82	7.66E-01	0.08	4.81	13.72	34.27	0.19	0.93	13.76
PreBMFe	0.74	**9.78E-03**	0.85	2.98	17.12	107.30	0.18	0.27	0.78
PostBMFe	0.39	8.61E-02	0.67	2.26	151.62	45.07	6.34	8.38	1124.09

Given the statistical differences observed in the in-situ OAC concentrations and multispectral reflectance (Table 4.1 and Table 4.2, respectively), significant differences in the developed models were not expected. However, since all models did not exhibit significant differences, further exploration was warranted. Vessels containing soil (e.g., C, B, and BM) as substrate produced significantly different models for TSS and color. The slopes of the color were significantly different, indicating the condition (e.g., mixing) affected the relationship between color and multispectral reflectance in OSWs compared to ODWs. The statistical differences in TSS models may be attributed to the soil substrate's presence, which leads to scattering and saturation, causing multispectral reflectance to not significantly increase as OAC concentrations

increase (Giardino et al. 2019). Thus, the number of suspended particles (e.g., TSS) appeared to alter the spectra complicating the models (Gholizadeh et al. 2016). The MChl-a models exhibited significant differences in both slope and constants. The significant increase in Fe from PreM to PostM likely caused the spectra to shift and change shapes at higher wavelengths impacting the region in which Chl-a could be readily estimated (e.g., RE) (Shah et al. 2020).

Additional evidence that spectra from ODWs more accurately represented in-situ OACs was the greater $R^2_{adj.}$ observed in the PostBChl-a, PostBFe, PostMFe, and PostBMChl-a models. Although the PreMTSS and PreMColor models could explain more variation in the dependent variables (e.g., $R^2_{adj.}$), the datasets' variability was lesser by an order of magnitude. Evaluation of the outputs revealed the PreM model estimates were more than 75 and 140 percent different (e.g., RPD) from the observed color and TSS, respectively. A review of absolute differences (e.g., MAE and SE) showed both PostM models to be higher quality estimators (e.g., lower MAE), the estimates of which were closer to the regression line (e.g., lower SE) (Table 4.3). In four cases, the pre-mixing data failed to produce models that satisfied the OLS regression criteria (e.g., PreCChl-a, PreBSDD, PreBMChl-a, and PreBMFe). Severe collinearity or redundancy (e.g., VIF) was present in the explanatory variables included in the PreCChl-a, PreBSDD, and PreBMChl-a models. The significant Koenker Statistic observed for the PreBMFe model suggests heteroscedasticity between the independent and dependent variables. Therefore, these models did not accurately represent the optical properties of the OACs in-situ, likely as a result of the limitations of remote sensing OSWs discussed earlier. These results support the first experimental hypothesis that in statistically similar OLS models, the optical properties of OACs were represented more accurately in ODWs than OSWs.

4.3.4 Effects of Remotely Sensing Substrate

To further assess the effects of remotely sensing substrate on spectral signatures, two evaluations (e.g., quantitative and qualitative) comparable to work published by Williams et al. (2002) and Hamza et al. (2016), who utilized SAM to assess two materials' spectral properties quantitatively were completed. In this study, assessment of spectral differences occurred in the three dimensions (e.g., RGB) within the VIS spectrum and captured by the RedEdge sensor. Due to the nature of manipulating aquatic OD and OAC concentrations, the spectral similarity between the pre-mixing vessels and the reference (e.g., soil or MDR) indicated the OSWs spectral signature was representative of the substrate. For the same reasons, all post-mixing vessels were expected to be spectrally similar to the reference (e.g., substrate).

For all spectra examined, the only vessel characterized as spectrally dissimilar to its reference was PreBM. BM was also the only vessel containing a mixture of the two reference substrates. The two substrates required separate analyses because the optical properties were not additive. Each substrate produced spectral dissimilarities, so the smaller angle was selected for presentation. Figure 4.5 graphically describes these spectral dissimilarities in a three-dimensional space where (β, γ, α) represent blue, green, and red band reflectance, respectively. The angles (e.g., Θ_1 and Θ_2) represent the angular dissimilarity from the MDR reference for PreBM and PostBM, respectively. Overall, bottom reflectance increased measured reflectance by approximately 4.5, 5.1, 21.8, and 15.6 percent when comparing the C, B, M, and BM vessels, respectively. These differences were similar in magnitude (e.g., 20 percent increase in OSWs) to studies examining the substrate's contribution to hyperspectral reflectance (e.g., Cannizzaro and Carder 2006; Zeng et al. 2017). The differences suggest sUAS-derived multispectral may serve as

a reasonable alternative to hyperspectral data allowing for more comprehensive examination (e.g., in terms of extent) of impaired surface waters for environmental remote sensing studies.

Completing a simple digital image analysis produced a qualitative assessment of the substrate's impact on sUAS-derived multispectral imagery. Anderson and Robins (1998) found iron precipitates to have high reflectance when examined with a false-color composite relative to scenes containing no iron precipitates. Figures 4.6A and 4.6B visualize the results of this exercise. The pre-mixing (Figure 4.6A) produced lower reflectance relative to the post-mixing counterpart (Figure 4.6B). These two analyses confirm that when the substrate was detectable (e.g., visible) through an OSW column, the substrate's EM signature was represented when measured with an sUAS—resulting in acceptance of the second experimental hypothesis.

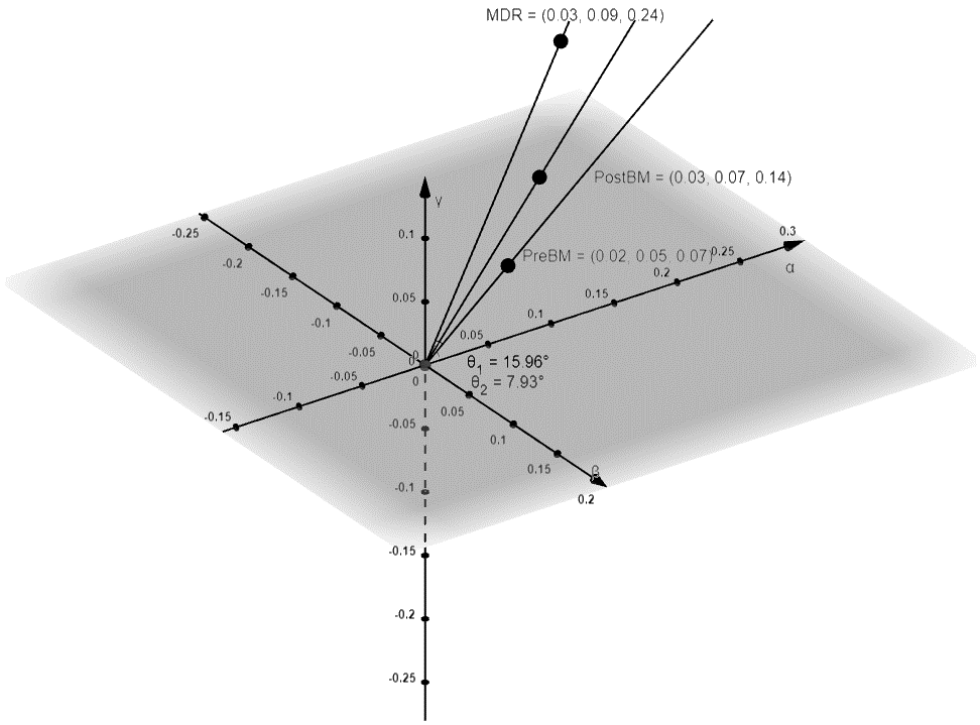

Figure 4.5 Results of SAM exercise for the only spectrally dissimilar vessel (e.g., PreBM) where (β, γ, α) represent blue, green, and red band reflectance, respectively; grey plane used to assist in visualization of three-dimensions, but is dimensionless (e.g., if γ were equal to zero points would fall on this plane); PreBM and PostBM spectral angles presented as Θ_1 and Θ_2, respectively.

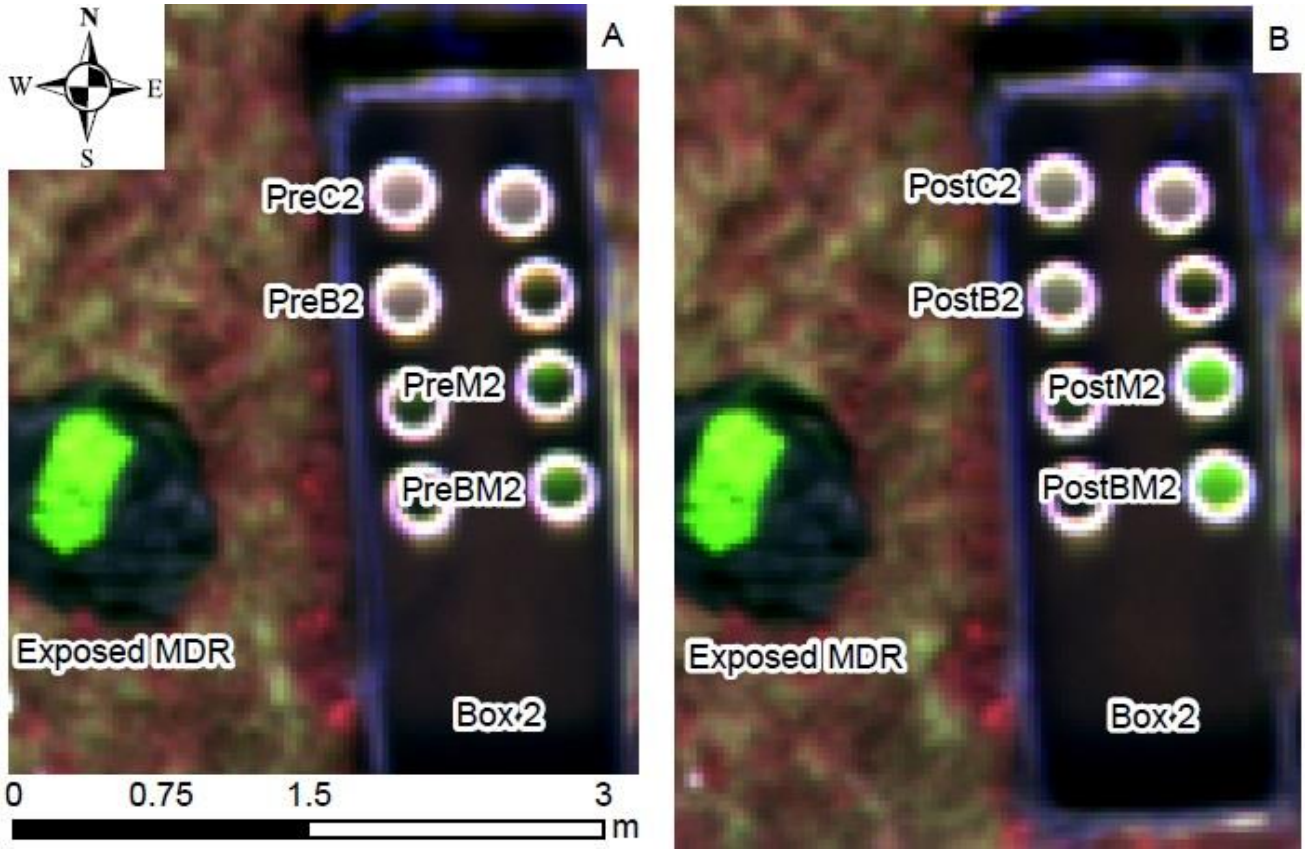

Figure 4.6 Qualitative identification of MDR substrate remotely sensed with sUAS and visualized in a false color composite (e.g., GBR) to demonstrate the impact substrate visible through a column of shallow water has on sUAS-derived multispectral imagery in OSWs (A) (e.g., pre-mixing) and ODWs (B) (e.g., post-mixing).

4.4 Conclusions and Future Directions

Through integrated remote sensing techniques and a novel experimental design, this study demonstrated how OACs present in various forms and concentrations were more accurately represented in mesocosm ODWs than OSWs when assessed with sUAS. Results confirm that the dominant OAC included in each treatment (e.g., Chl-a in B) significantly influenced the spectral signature measured, which limited the ability to estimate concentrations of other OACs in-situ. Unfortunately, interactions among OACs were not well reported in the literature, nor the focus of this study. Thus, future studies were suggested.

This study also suggests two approaches for determining the optical impacts of remote sensing substrate through OSW columns, the results of which were comparable to studies that utilized hyperspectral data, suggesting sUAS represent a reasonable alternative for spectral data collection in optically complex waters. This study's results indicate that an sUAS equipped with a multispectral sensor could estimate OAC concentrations in shallow optically complex waters. sUAS could also identify OSWs and determine whether the spectra measured from an OSW column represent the bottom substrate. Together these examinations provide insight into the capabilities and limitations of remote monitoring with sUAS in optically complex inland waters.

However, further work will be required to confirm if SDD may be an in-field surrogate for aquatic OD. Additional research should attempt to quantify the undocumented interactions between OACs present in natural waters. Performing a similar study with higher-resolution sensors (e.g., hyperspectral) and sUAS would allow for comparisons between the platforms. This level of characterization may also provide enough spectral data to estimate OAC in OSWs. Overall, this study provides a basis for real-world in-situ monitoring with sUAS in natural optically complex waters common around the world.

Literature Cited

Arango, J. G., and Nairn, R. W. (2020) Prediction of optical and non-optical water quality parameters in oligotrophic and eutrophic aquatic systems using a small unmanned aerial system. *Drones,* https://doi.org/10.3390/drones4010001.

Anderson, J., Robbins, E. (1998) Spectral reflectance and detection of iron-oxide precipitates associated with acidic mine drainage. *Photogrammetric Engineering and Remote Sensing,* 64(12) 1201-1208. ISSN: 0099-1112/98/6412-1201.

ASTM. (1997) Standard Method 2540D: The determination of total suspended solids in aqueous samples. *Standard Methods for the Examination of Water and Wastewater*. https://doi.org/10.2105/SMWW.2882.030.

Becker, R.H., Sayers, M., Dehm, D., Shuchman, R., Quintero, K., Bosse, K., Sawtell, R. (2019) Unmanned aerial system based spectroradiometer for monitoring harmful algal blooms: a new paradigm in water quality monitoring. *Journal of Great Lakes Research*, 45(3):444-453. https://doi.org/10.1016/j.jglr.2019.03.006.

Cannizzaro, J., Carder, K. (2006) Estimating chlorophyll a concentrations from remote-sensing reflectance in optically shallow waters. *Remote Sensing of the Environment*, 101(2006): 13-24. https://doi.org/10.1016/j.rse.2005.12.002.

Dall'Olmo, G., Gitelson, A. (2005) Effect of bio-optical parameter variability on the remote estimation of chlorophyll-a concentration in turbid productive waters: experimental results. *Applied Optics,* 44(3): 412-422. https://doi.org/10.1364/AO.45.003577.

Dörnhöfer, K., and Oppelt, N. (2016) Remote sensing for lake research and monitoring – recent advances. *Ecological Indicators*, https://doi.org/10.1016/j.ecolind.2015.12.009.

ESRI. (2018a) How exploratory regression works. https://desktop.arcgis.com/en/arcmap/10.3/tools/spatial-statistics-toolbox/how-exploratory-regression-works.htm (accessed 8 March 2021).

ESRI. (2018b) Exploratory regression. https://desktop.arcgis.com/en/arcmap/10.3/tools/spatial-statistics-toolbox/exploratory-regression.htm (accessed 8 March 2021).

ESRI. (2018c) Ordinary least squares (OLS). https://desktop.arcgis.com/en/arcmap/10.3/tools/spatial-statistics-toolbox/ordinary-least-squares.htm (accessed 8 March 2021).

Frost, J. (2020) *Regression analysis: an intuitive guide for using and interpreting linear models, first ed.* Statistics by Jim Publishing.

Gholizadeh, M., Melesse, A., Reddi, L. (2016) A comprehensive review on water quality parameters estimation using remote sensing techniques. *Sensors*, 16(8): 1298-1340. https://doi.org/10.3390/s16081298.

Giardino, C., Brando, V., Gege, P., Pinnel, N., Hochberg, E., Knaeps, E., Reusen, I., Doerffer, R., Bresciani, M., Braga, F., Foerster, S., Champollion, N, Dekker, A. (2019) Imaging spectrometry of inland and coastal waters: state of the art, achievements and perspectives. *Surveys in Geophysics,* 40(3): 401-429. https://doi.org/10.1007/s10712-018-9476-0.

Gould, R., Arnone, R. (1997) Remote sensing estimates of inherent optical properties in a coastal environment. *Remote Sensing of Environment,* 61(2): 290-301. https://doi.org/10.1016/S0034-4257(97)89496-5.

Hamza, M., Al-Thubaiti, A.S., Dhieb, M., Bel Haj Ali, A., Garbouj, M., Ajmi, M. (2016) Dasymetric mapping as a tool to assess the spatial distribution of population in Jeddah City (Kingdom of Saudi Arabia). *Current Urban Studies,* 4: 329-342. https://doi.org/10.4236/cus.2016.43022.

Larson, M., Simic Milas, A., Vincent, R., Evans, J. (2018) Multi-depth suspended sediment estimation using high-resolution remote-sensing UAV in Maumee River, Ohio. *International Journal of Remote Sensing*, https://doi.org/10.1080/01431161.2018.1465616.

Liu, Y., Islam, MA., Gao, J. (2003) Quantification of shall water quality parameters by means of remote sensing. *Progress in Physical Geography*, https://doi.10.1191/0309133303pp357ra.

Millennium Ecosystem Assessment (MA). (2005). *Ecosystems and Human Well-Being: Synthesis*. Washington, DC: Island Press.

Mobley, C., Sundman, L., Davis, C., Bowles, J., Downes, T., Leathers, R., Montes, M., Bissett, W., Kohler, D., Reid, R., Louchard, E., Gleason, A. (2005) Interpretation of hyperspectral remote-sensing imagery by spectrum matching and look-up tables. *Applied Optics,* 44(17): 3576-3592. https://doi.org/10.1364/AO.44.003576.

Odermatt, D., Gitelson, A., Brando, V., Schaepman, M. (2012) Review of constituent retrieval in optically deep and complex waters from satellite imagery. *Remote Sensing of Environment,* 118: 116-126. https://doi.org/10.1016/j.rse.2011.11.013.

Palmer, S., Kutser, T., Hunter, P. (2015) Remote sensing of inland waters: Challenges, progress and future directions. *Remote Sensing of Environment*, 157(2015): 1-8. https://doi.org/10.1016/j.rse.2014.09.021.

Rostom, N., Shalaby, A., Issa, Y., Afifi, A. (2017) Evaluation of Mariut Lake water quality using hyperspectral remote sensing and laboratory works. *The Egyptian Journal of Remote Sensing and Space Sciences,* 20: S39-S48. https://doi.org/10.1016/j.ejrs.2016.11.002.

Sandidge, J., Holyer, R. (1998) Coastal bathymetry from hyperspectral observations of water radiance. *Remote Sensing of Environment,* 65(3): 341-352. https://doi.org/10.1016/S0034-4257(98)00043-1.

Seidel, M., Hutengs, C., Oertel, F., Schwefel, D., Jung, A., Vohland, M. (2020) Underwater use of a hyperspectral camera to estimate optically active substances in the water column of freshwater lakes. *Remote Sensing*, 12(11): 1745-1764. https://doi.org/10.3390/rs12111745.

Shafique, N.A., Fulk, F., Autrey, B.C., Flotemersch, J. (2003) Hyperspectral remote sensing of water quality parameters for large rivers in the Ohio river basin. In: Proceedings of the 1st Interagency Conference on Research in Watersheds. Benson, AZ.

Shah, A., Deshmukh, B., Sinha, L.K. (2020) A review of approaches for water depth estimation with multispectral data. *World Water Policy,* 6(1): 152-167. https://doi.org/10.1002/wwp2.120029.

Su, T.C. (2017) A study of a matching pixel by pixel (MPP) algorithm to establish an empirical model of water quality mapping, as based on unmanned aerial vehicle (UAV) images. *International Journal of Applied Earth Observation and Geoinformation,* 58(2017): 213-224. https://doi.org/10.1016/j.jag.2017.02.011.

Tang, Z., Nairn, R. (2021) Mine drainage residual additions to lake sediments alter phosphorus and trace metal distributions. *Water, Air, and Soil Pollution,* 232(52): 51 – 64. https://doi.org/10.1007/s11270-021-05016-3.

Torrent, J., Barrón, V. (2002) Diffuse reflectance spectroscopy of iron oxides. Encyclopedia of Surface and Colloid Science (1): 1438-1446.

United States Environmental Protection Agency (USEPA). (1993). Method 180.1: Determination of Turbidity by Nephelometry. Rev 2.0.

United States Environmental Protection Agency (USEPA) (1997). Method 445.0: In vitro determination of Chlorophyll a and Pheophytin a in marine and freshwater algae by fluorescence. Rev. 1.2.

United States Environmental Protection Agency (USEPA) (2007). Method 3015A (SW-846): Microwave-assisted acid digestion of aqueous samples and extracts. Rev. 1.0.

United States Environmental Protection Agency (USEPA) (2007). Method 6010C (SW-846): Inductively coupled plasma optical emission spectrometry. Rev. 3.0.

United States Environmental Protection Agency (USEPA) (2016). Method 147A (SW-846): Color in drinking, saline, and surface waters; domestic and industrial wastes. Rev. 0.0.

Van der Meer, F. (1997) Mineral mapping and landsat thematic mapper image classification using spectral unmixing. *Geocarto International,* 12(3): 24-40. https://doi.org/10.1080/10106049709354594.

Voss, K., Mobley, C., Sundman, L., Ivey, J., Mazel, C. (2003) The spectral upwelling radiance distribution in optically shallow waters Limnology and Oceanography 48(1): 364-373. https://doi.org/10.4319/lo.2003.48.1_part_2.0364.

Whitehead, K., Hugenholtz, C. (2014) Remote sensing of the environment with small unmanned aircraft systems (UASs), part 1: a review of progress and challenges. *Journal of Unmanned Vehicle Systems,* 02(03): 69-85. https://doi.org/10.1139/juvs-2014-0006.

Williams, J. D., Bigham, M. J., Cravotta III, A. C., Traina, J. S., Anderson, E. J., and Lyon, G. J. (2002). Assessing mine drainage pH from the color and spectral reflectance of chemical precipitates. *Applied Geochemistry*, https://doi.org/10.1016/S0883-2927(02)00019-7.

Zeng, C., Richardson, M., King, D. (2017) The impacts of environmental variables on water reflectance measured using a lightweight unmanned aerial vehicle (UAV)-based spectrometer system. ISPRS Journal of Photogrammetry and Remote Sensing 130: 217-230. https://doi.org/10.1016/j.isprsjprs.2017.06.004.

Zhang, Z., Li, H., Cybele, M., Dai, W., Li, Z. (2019) Remotely sensed water reflectance measurements based on unmanned aerial vehicle (UAV). In: Chung J, Triantafyllou M, Langen I, Yao T (eds) Proceedings of the twenty-ninth 2019 International Ocean and Polar Engineering Conference. Honolulu, Hawaii, 614-619.

Zhou, X., Marani, M., Albertson, J., Silvestri, S. (2017) Hyperspectral and multispectral retrieval of suspended sediment in shallow coastal waters using semi-analytical and empirical methods. *Remote Sensing,* 9(4): 393-421. https://doi.org/10.3390/rs9040393.

Chapter 5: Effects of Mission Parameters on the Accuracy and Efficiency of sUAS-Derived Multispectral Imagery and Operations

This chapter was formatted as a manuscript for submission to the ISPRS Journal of Photogrammetry and Remote Sensing.

Abstract:

Data collection from afar (e.g., remote sensing) allows scientists to study natural phenomena at more acceptable temporal resolutions and greater areal extents than traditional (e.g., in-situ) environmental studies. Unfortunately, the scientific literature lacks a defined standard method for collecting small Unoccupied Aerial Systems (sUAS)-derived multispectral imagery for environmental modeling purposes (e.g., water quality estimation). The development of a proposed method must incorporate the understanding that each sUAS has system-specific constraints (e.g., battery life, flight speed, and wind stability) and collects mission-specific data (e.g., true color, multispectral, or hyperspectral imagery). Therefore, this study's goal was to provide a basis for developing an sUAS image collection standard operating procedure for environmental monitoring by examining the impact mission parameters had on imagery generated. An assessment of the spatial and spectral characteristics of the sUAS imagery was presented in a standardized manner. Evaluation of accuracy (e.g., reflectance and color) and efficiency (e.g., flight time and battery consumption) of individual sUAS missions produced a set of operational parameters to be considered in future environmental remote sensing studies. Providing a methodological approach for the development of calibrated target objects was required because no one set of parameters will work for all sUAS, target objects, or study goals. Results demonstrate the precise identification of color was heavily reliant on pixel resolutions and in-situ solar conditions during operations. Furthermore, changes in solar conditions could describe approximately 60 percent of the error observed in color identification. Overall, the most efficient mission, in terms of flight time and image storage space, did not produce the most precise color representation, suggesting the balance between sUAS operations and data quality has yet to be achieved. Future studies must further examine the tradeoffs between changes in solar conditions (e.g., solar elevation angle), areal coverage (e.g., high altitude flights), fine spatial resolutions, and the accurate retrieval of spectra (e.g., color) while communicating in a manner

that is transferable across the digital environment, ensuring future environmental remote sensing studies produce the highest quality data possible.

Keywords:

Multispectral Reflectance, Munsell, Environmental Remote Sensing

5.1 Introduction

5.1.1 Remote Sensing with sUAS

Small Unoccupied Aerial Systems (sUAS) have demonstrated applications for precision agriculture (Peter et al. 2020), land cover identification (Ridd 1994), mining exploration (Park and Choi 2020), land reclamation (Martin et al. 2015), and in-situ surface water quality examinations (Holzbauer-Schweitzer and Nairn 2020). sUAS present tremendous benefits over satellite remote sensing, such as finer spatial resolution, operations under clouds with limited atmospheric effects, and the ability to perform missions autonomously at the operator's discretion. Finer spatial resolutions allow for studies in smaller focus areas and more minute examinations of the scene (Small 2003). The reported “success” of studies varies across the literature, with a heavy dependency on the application and the object(s) being remotely sensed (Whitehead and Hugenholtz 2014; Gholizadeh et al. 2016; Park and Choi 2020).

Since remote sensing with sUAS is in its adolescence, a need exists to develop standardized operational methods (Shah et al. 2020). This need arises from the laborious and, at times, temporally or spatially misrepresentative nature of the traditional in-situ monitoring of terrestrial and aquatic environments (Biber 2013). Numerous studies have already demonstrated the benefit of environmental remote sensing. Incorporating sUAS in regular monitoring efforts would not only improve the extent of current monitoring efforts but over time, with increased computing (e.g., artificial intelligence) and technological capabilities (e.g., increased sensor abilities and accuracies), sUAS may serve as a reasonable alternative to traditional monitoring efforts. This standardization of operational parameters must consider differences in sUAS platforms (e.g., flight time, maximum velocity, and image stabilization capabilities), operational

conditions (e.g., operation mode, illumination, wind or other risks), and sensor capabilities (e.g., ground sampling distance).

Examining how altering specific parameters on an autonomously operated sUAS may be of particular interest. Ranquist et al. (2016) explored the impact various weather parameters (e.g., fog, haze, and glare) had on sUAS operations and operators but did not assess data quality. Zeng et al. (2017) described the environmental effects of remote sensing with sUAS over various water bodies. Results demonstrated that spectra measured in the same location at different times had a standard deviation of 10.4 percent, changes in altitude (e.g., 20 to 100 m) had negligible effects on reflectance, and spectra exposed to glint or shadows abruptly and unpredictably changed (Zeng et al. 2017). Mamaghani et al. (2019) used a MicaSense RedEdge 3 (MicaSense, Inc., Seattle, Washington, USA 98103) to examine changes in vegetation reflectance (via Normalized Difference Vegetation Index (NDVI) calculations) throughout a day, at a single altitude (e.g., 1.5 m) while applying various sensor calibration techniques. The results show reflectance increased with decreases in solar zenith angles (e.g., complementary to solar elevation angle) and had higher standard deviations on sunny versus cloudy days. Increases in standard deviations were attributed to shadows on sunny days, which significantly altered the scene's overall reflectance. Most environmental remote sensing applications state the products developed (e.g., water quality retrieval models) exhibit certain levels of site-specificity (Liu et al. 2003), and the studies described earlier were no different. Standardizing target objects, like those used to calibrate spectral sensors (e.g., calibrated reflectance panels) would provide a unique opportunity to communicate sUAS performance. However, before developing a standard method, one must consider the sensors utilized (e.g., the specific band(s) and multi- or hyperspectral imaging

capabilities), the optical properties of the target object desired (e.g., reflectance, transmittance, or absorbance), along with all other sUAS characteristics mentioned earlier. Since most environmental remote sensing studies report products (e.g., NDVI) with spectra contained in the visible spectrum, it appears a standardization of color would be most appropriate (e.g., Gholizadeh et al. 2016). Therefore, a study controlling sUAS operational parameters while examining calibrated target objects and reporting success in a standardized metric may fill the identified literature gap. Such a study may also provide a basis for the integration of sUAS into traditional environmental monitoring practices.

5.1.2 Color

Although the perception of color, its communication, derivation, or conversion was not necessarily the focus of this study, a basic understanding was required. The perception of color is subjective among observers, both natural (e.g., humans) and digital (e.g., monitors, printers, and sensors). Various color models or color spaces have managed color mathematically by representing colors as tuples of values. Developed in 1996 for digital displays, printers, and throughout the internet, sRGB is one of the most common color spaces. Based on the human perception of color, sRGB is an additive color model based on the combination of light from the three primary sources (e.g., red, green, and blue) with values ranging from 0 - 255. However, the colors represented were device-specific, resulting in the perception of different colors across devices if a color management scheme (e.g., standardization) was not applied (Mokrzycki and Tatol 2011).

Typically, from the environmental perspective, the Munsell system is utilized to identify soil and other natural colors (Anderson and Robbins 1998; Torrent and Barrón 2002; Poppiel et al. 2020).

Three components (e.g., chroma, value, and hue) comprise the system used to describe the richness or saturation, lightness, and color (e.g., blue) of the material, respectively (Poppiel et al. 2020). In the Munsell color space, a combination of chroma, value, and hue make up the perceived color. For remote sensing applications, the Munsell neutral color scale can be used for sensor calibration (e.g., calibrated reflectance panels), testing imagery, or reflectance standards (X-Rite 2021A). In this system, absolute achromatic colors (e.g., white, black, and pure greys) have zero chromas and no hue. Instead, the letter "N" replaces the hue notation. Thus, the value can range from 0 (e.g., absolute black) to 10 (e.g., absolute white), where N5 would occur halfway between the absolutes, visually (X-Rite 2021A).

However, both the sRGB and Munsell systems describe the human perception of color but do not account for illumination or observation conditions at the time of viewing. On the other hand, uniform color spaces (UCS) standardize color differences, so the perceived color difference is proportional to the spatial distance in the color space (Mokrzycki and Tatol 2011). Specifically, a conversion to the International Commission on Illumination (CIE) L^* a^* b^* ($L^*a^*b^*$) coordinates, where L^* represents lightness, a^* is the red/green coordinate, and b^* is the blue/yellow coordinate. Once in this UCS, colors can be discussed in a standardized manner. More importantly, the calculated difference (e.g., Delta Empfindug (ΔE)) in color can be communicated. ΔE represents the Euclidean distance between two colors, which is proportional to the visually perceived difference. Generally, ΔE values below 2 require experienced observers to differentiate. Values of 2 – 4 are perceivable to the average human eye, while values greater than 5 indicate significant color differences (Mokrzycki and Tatol 2011). Another valuable metric is the Color Quality Scale (CQS) which Davis and Ohno (2005) described in detail. Briefly, CQS ranges

from 0 to 100 (e.g., indicates true color match) and assesses overall color quality by penalizing (e.g., decreasing CQS) colors that shifted in hue or lightness and decreased in chroma by compensating for illumination and observation conditions.

Therefore, this study communicates the effect altering sUAS operational parameters had on reflectance from calibrated target objects with known colors consistently and comparably. Thus, it was hypothesized that various operational parameters (e.g., flight speed, altitude, image overlap, and operations around solar noon) would impact the quality of sUAS-derived multispectral imagery and the ability to develop accurate statistical models. The hypothesis was evaluated by quantifying the spectral error caused by performing sUAS missions under differing conditions and identifying the set of parameters that produced the highest quality data most efficiently. Overall, the goal was to provide a basis for the development of standard operating procedures to be used for environmental monitoring via sUAS.

5.2 Materials and Methods

5.2.1 Study Site Characteristics

The study site utilized was in Noble, Oklahoma (35.128710, -97.325059) and provided an area to examine the target objects. Although small (< 10,000 m^2), the site was relatively level and void of shadows minimizing the potential for shading from vegetation or panel components. The site was visited once on February 5th, 2021. Solar azimuth and elevation angles were collected after operations using the Solar Calculator maintained by the National Oceanic and Atmospheric Administration (NOAA) Global Monitoring Laboratory (GML) at the latitude and longitude provided (NOAA GML 2021).

5.2.2 Description and Classification of Target Objects

Calibrated target objects were created for this study. These objects consisted of six 1.2 X 1.2 m medium density fiberboard (MDF) calibrated panels. Each side of the calibrated panels was sanded with 80-grit sandpaper to promote primer adhesion (Figure 5.1A). Between each sanding, dust was removed with a vacuum and a damp cloth (e.g., mineral spirits). The front was then sanded with 150-grit sandpaper and cleaned following the same process (Figure 5.1B). Panels were primed with an oil-based interior/exterior primer using 7.5-cm chiseled foam brushes and allowed to dry (Figure 5.1C). Unfortunately, because MDF is highly absorbent, it took two to three coats to sufficiently cover the panel's surface. Between each coat, the panels were sanded (e.g., 150-grit) and cleaned according to the described process. Upon achieving sufficient coverage, the panels' front side was sanded with 220-grit sandpaper to remove unevenly primed surfaces (Figure 5.1D). A final cleaning followed the final sanding. Then each of the six boards received two coats of flat matte spray paint manufactured by MyPerfectColor®. The manufacturers' website (MyPerfectColor.com) provided reference Light Reflectance Values (LRVs), and a comparison to the observed LRV allowed for an assessment of application and manufacturing consistencies. Paints were applied according to manufacturer specifications and allowed to air dry. Once panels dried, they were cleaned a final time and prepared for divisions. The divisions were established with 2.5-cm black duct tape allowing for examination of mixed pixels and identification of measurement areas. Each panel was initially divided into four equally sized squares (e.g., 0.6 m X 0.6 m). Each square was then further divided into a smaller 15 X 15 cm square (e.g., measurement square) where colorimetric measurements were collected.

Figure 5.1 Calibrated panels in development, (A) after being sanded with 80-grit (B) and 150-grit sandpaper, (C) application of a single coat of primer, and (D) multiple coats of primer and a final sanding with 220-grit sandpaper.

Examination of four "natural" panels also occurred (Table 5.1). These MDF panels were similar in dimensions to the calibrated panels but were not prepared (e.g., sanded) before field deployment. The materials used to cover these panels consisted of tan play sand (TSand), grey paver sand (GSand), dried mine drainage residuals (MDR) from the Mayer Ranch Passive Treatment System (see Tang and Nairn (2021) for more details), and local topsoil (Soil). These objects were selected to represent a variety of colors present in natural environments. MDR and TSand were processed to pass a #40 sieve (e.g., particles < 0.420 mm), the GSand was processed to pass #20 sieve (e.g., particles < 0.841 mm), and the topsoil was unprocessed. The processing created homogenous (e.g., size, color, and the ability to level material) surfaces, which allowed

an assessment of particle size impacted sUAS-derived multispectral imagery. These boards were divided with 1.22 m X 2.5 cm furring (wood) strips to resemble the divisions established on the calibrated panels and allow a more direct comparison of the spectra.

The perceived color of each panel was measured with an X-Rite CAPSURE RM200 (X-Rite 2021B) (Table 5.1) (Figure 5.2). Technology within the CAPSURE was capable of compensating for irregular surfaces (e.g., textured samples compared to smooth color swatches), allowed for the selection of sample area size (2, 4, or 8 mm), and provided its illumination source (e.g., D65 – average daylight illumination). Before CAPSURE measurements were collected, the instrument was calibrated with a device-specific calibrated reflectance panel (e.g., white reference slider) which also served to protect the instruments' optical components. Color measurements were collected with an 8 mm aperture in each of the four measurement squares and consisted of three "perfect" matches (e.g., 12 matches per panel). In this study, a "perfect" match was identified for each panel by allowing the instrument to select from three Munsell fan decks (e.g., Munsell Book of Color Matte, Munsell Glossy Book, and Munsell Soil Book). Collecting numerous color measurements on the panel suggested the perceived color of the entire panel was relatively consistent. The focus is on panels described in Table 5.1 due to image saturation issues caused by two panels (e.g., N9 and N8) which will be further discussed in Section 5.3.2 Representation of Color.

Table 5.1 Munsell color characteristics of calibrated and natural panels, (-) indicate no value, and MyPerfectColor supplied manufacturer LRV.

	Munsell Color Characteristics			Manufacturer
Panel ID	**Hue**	**Value**	**Chroma**	**LRV (percent)**
N7	-	7/	0 (N)	44.11
N6	-	6/	0 (N)	28.86
N4	-	4/	0 (N)	9.74
N3	-	3/	0 (N)	7.49
TSand	10YR	6/	4	-
GSand	5Y	7/	1	-
MDR	5YR	4/	8	-
Soil	7.5YR	4/	3	-

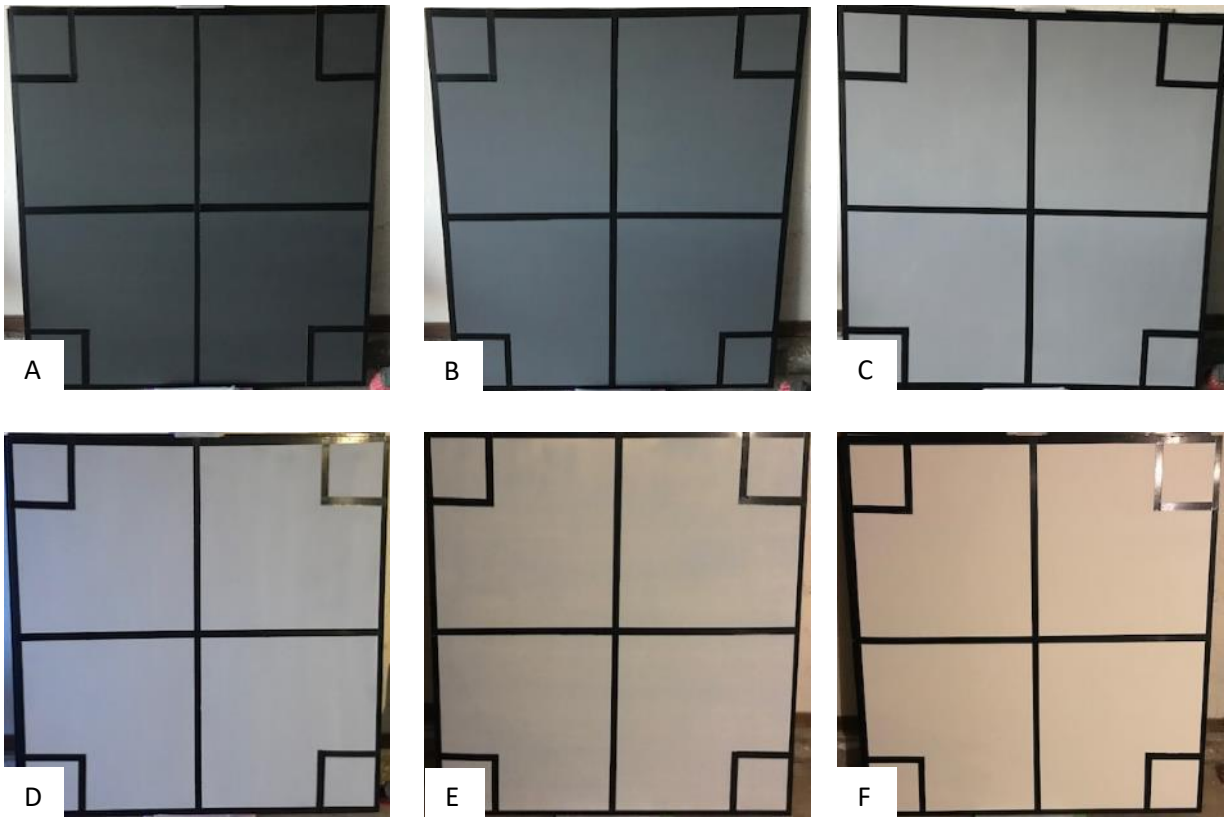

Figure 5.2 Finished calibrated panels (1.2 m X 1.2 m), divided with 2.5 cm black duct tape into four equally sized (0.6 m X 0.6 m) squares and further divided in the corners to smaller (15 cm X 15 cm) measurement where colorimetric measurements were collected. Panels (A), (B), (C), (D), (E), and (F) represent values of N3, N4, N6, N7, N8, and N9 on the Munsell neutral color scale, respectively.

5.2.3 Description of sUAS, Operations, and Reflectance

The sUAS utilized in this study was an Aerial Technologies International (ATI) AgBot V2 equipped with a MicaSense RedEdge multispectral sensor (RedEdge sensor) and a downwelling solar irradiance (e.g., light) sensor (DLS). The AgBot is a vertical takeoff and landing (VTOL) quadcopter (e.g., four-rotor) operated autonomously using MissionPlanner Software V. 1.6.67, a 3D Robotics PixHawk autopilot, and a HEX/ProfiCNC Here2 GPS module. The AgBot can reach flight speeds of approximately 15 m sec^{-1}, a range of approximately 25 km, with a flight time of about 20 minutes. The RedEdge sensor simultaneously captures spectral data in five discrete bands with center points at 475 (blue), 560 (green), 668 (red), 717 (rededge), and 840 (near-infrared (NIR)) nm. The ground sampling distance (e.g., pixel resolution) produced by this sensor is approximately 3, 4.5, and 6.5 cm $pixel^{-1}$ when operated at 50, 75, and 100 m above ground level (AGL). Raw ".TIF" format multispectral imagery produced by this sensor was radiometrically corrected, mosaiced, and orthorectified using the manufacturer recommended Pix4DMapper Pro V 4.3.9. To assist in the radiometric correction, a DLS was integrated into the sUAS. This sensor improves the imagery's radiometric quality by measuring solar irradiance conditions throughout the mission and supplying the information to the processing software. Before and after each mission, an image of a calibrated reflectance panel was captured with the RedEdge sensor for additional radiometric correction. Although this software provides limited custom processing options, it was selected for simplicity, repeatability, and to represent a reliable processing option, should sUAS achieve more widespread use (Mamaghani and Salvaggio 2019).

The RedEdge sensor manufacturer (MicaSense 2021) suggests specific operational parameters to produce the highest quality data. By far, the recommendation for overlap (e.g., 75 percent of the

image overlaps with subsequent images) appeared to the most influential parameter. Additional considerations were given to altitude and flight speed, time of operation (e.g., solar noon), the calibration procedure, and the need to collect imagery at nadir. Thus, the parameters manipulated in this study to determine their effect on spectral reflectance were operations around solar noon, flight speed, altitude, and image overlap (Table 5.2). The missions were developed in sets of three, allowing for a comparison of spectra from minor changes to the operational parameters. For example, mission 1 (M1), M7, and M11 served as the control missions emphasizing solar noon operations. Image overlap was also studied because the manufacturers focused on required values (e.g., 75 percent). M8, M9, and M10 examined overlap at the manufacturer specification and ± 10 percent of the recommendation to assess whether sacrificing data quality could increase mission efficiency (e.g., coverage, mission time, and battery consumption). A final set of operational parameters based on sUAS mission efficiency (e.g., coverage time^{-1}) and data accuracy was examined.

Once post-processed, the sUAS-derived multispectral pixel values (e.g., spectral reflectance) and stretched values (e.g., sRGB) were manually extracted in ArcMap V. 10.6.1 using the Pixel Inspector tool. The nine central-most pixels within the measurement square were of focus, assessing the mixed pixel phenomenon (e.g., pixel and stretched values were not pure representations of the target object). Cross-sectional profiles of the panels showing how reflectance changed across the surface were developed with the Interpolate Line and Profile Graph tools in ArcMap V. 10.6.1.

Table 5.2 Operational parameters examined, sets indicated with bold; italicized missions (e.g., M1, M7, and M11) served to assess operations around solar noon, ΔAzimuth and ΔElevation indicate the change in solar azimuth and elevation angles throughout sUAS missions.

Mission	Altitude (m)	Flight speed (m sec^{-1})	Image Overlap (percent)	ΔAzimuth (degree)	ΔElevation (degree)
M1	***50***	*5*	*80*	1.21	0.18
M2	**75**	5	80	1.22	0.12
M3	**100**	5	80	1.24	0.06
M4	50	**7.5**	80	1.24	-0.03
M5	50	**10**	80	1.24	-0.08
M6	50	**12.5**	80	1.23	-0.13
M7	*50*	*5*	*80*	1.48	-0.30
M8	50	5	**65**	1.15	-0.28
M9	50	5	**75**	0.83	-0.25
M10	50	5	**85**	1.31	-0.50
M11	*50*	*5*	*80*	1.25	-0.58

5.2.4 Assessment of Perceived Color

Removing the human aspect of color perception was necessary for this study. Utilizing a UCS was required to compare colors quantified by different instrumentation and to communicate across the digital environment. Fortunately, most modern technology defaults to the sRGB colorspace, which uses red, blue, and green as the primary color channels with possible values ranging from 0 to 255. The sUAS-derived sRGB values were extracted from processed imagery using techniques described earlier. Reference Munsell values (e.g., perfect CAPSURE matches) were converted to sRGB using open-source R Statistical Software V. 3.5.2 code provided by Rossel et al. (2006). Both the reference sRGB and sUAS-derived sRGB values were then further standardized (e.g., illumination and observation conditions) to CIE $L^*a^*b^*$ coordinates with the open-source ColorMine library V 1.1.3 supported by the Massachusetts Institute of Technology (MIT) and executed in Python programming language (Colormine 2014).

Once all spectra were converted to a UCS, additional metrics could be calculated to evaluate the colors perceived by the sUAS. The LRV was used to describe how light or dark a material looked with values ranging from 0 (e.g., black) to 100 (e.g., white) and was calculated with Equation 1. To evaluate the color differences (e.g., Euclidean distance within the CIE color space or perceived difference in visual sensation), ΔE calculations occurred for each panel contained within the sUAS missions (Equation 2). To assess which set of sUAS parameters produced color most representative of the references (e.g., panels), the National Institute of Standards and Technology (NIST) CQS V 7.40 was applied. CQS was determined using the calculated ΔE of each panel from all sUAS missions, D65 illumination conditions (e.g., average daylight illumination) and Equations 3 and 4. Equation 4 was required to scale the CQS values from the outdated Color Rendering Index (CRI) (Davis and Ohno 2005). A final comparison was performed to examine the multispectral reflectance pixel value and CAPSURE reference spectra (e.g., assumed to represent spectral reflectance (from 380 – 730 nm, in ten nm bands) of various Munsell colors) collected under different illumination and observation conditions. This exercise's goal was to demonstrate the need to communicate color (e.g., VIS spectra) in a standardized manner.

$$LRV = \left(\frac{L^{*}+16}{116}\right)^{3} * 100 \quad \text{Eq. 1}$$

Where:

LRV = Light Reflectance Value, percentage

L^{*} = CIE standard lightness value

$$\Delta E = \sqrt{\left(L^{*}_{sample} - L^{*}_{reference}\right)^{2} + \left(a^{*}_{sample} - a^{*}_{reference}\right)^{2} + \left(b^{*}_{sample} - b^{*}_{reference}\right)^{2}} \quad \text{Eq. 2}$$

Where:

ΔE = Delta Empfindug – Euclidean distance between two colors in UCS

L^* = CIE standard lightness value

a^* = CIE red/green coordinate

b^* = CIE blue/yellow coordinate

$$R_a = \sqrt{\frac{1}{n}\sum_{i=1}^{n}\Delta E_i^2} \quad \text{Eq. 3}$$

Where:

R_a = General color rendering index

n = sample size

ΔE = Delta Empfindug – Euclidean distance between two colors in UCS

$$CQS = 10 * ln\left[exp^{\frac{R_a}{10}} + 1\right] \quad \text{Eq. 4}$$

Where:

CQS = Color Quality Scale

R_a = General color rendering index

5.2.5 Evaluation of Mission Efficiency

Evaluation of sUAS mission efficiency occurred using the ΔE calculations. Mission parameters evaluated included mission storage capacity (e.g., disk space required), number of images per band, spatial resolution, area covered, relative percent difference between initial and optimized camera parameters (e.g., focal length), which should always be lower than 5 percent, pixel reprojection error in the orthomosaic, battery voltage and percentage consumed, along with the change in azimuth and solar elevation angles throughout the mission. Assessing the linear relationship between calculated ΔE and the quality report parameters output from the

processing software (Pix4DMapper) provided such an efficiency metric. The goal was to identify mission parameters capable of describing the error (e.g., coefficient of determination (R^2)) observed with color identification (e.g., ΔE) to assist in the quantification of the performance of individual missions and identification of error sources.

5.3 Results and Discussion

Changes to solar azimuth (e.g., the clockwise angle from true north to object) and elevation (e.g., the angle from the horizon to object) angles during the study day (February 5th, 2021 1200 – 1444 CST) are reported in Table 5.2. The most substantial positive (0.18°) and negative (-0.58°) changes in solar elevation angles occurred throughout the first (e.g., M1) and last missions (e.g., M11), respectively (e.g., closer to sunrise and sunset). Solar noon occurred just before starting M4, while the greatest change in solar azimuth angles was observed during M7 (1.48°). These conditions fit the study design well, which purposefully exposed all three control missions (e.g., M1, M7, and M11) to these changes in solar conditions (e.g., operations around solar noon). Furthermore, shading caused by vegetation was absent, while cloud cover and shading from panel components were minimal throughout operations. Before beginning the missions, the maximum measured wind speed and temperature at the ground surface were 2.2 m sec^{-1} and 13.4 °C, respectively. Since the DLS accounted for illumination variations throughout the mission, any changes to the spectra collected were assumed to be a result of the mission parameters (e.g., flight altitude, speed, and image overlap) and solar conditions (e.g., operation around solar noon) for each flight (Table 5.3, Figure 5.3). Multispectral imagery and data will be presented from the most representative (e.g., lowest ΔE for all panels) mission within a set (e.g., M1, M2, M4, M9).

*Table 5.3 Bolded reference (e.g., N7) values were provided by paint manufacturer; other values were measured (reflectance (center point in nm) and color as sRGB (red, green, and blue)) or calculated (L*a*b* and ΔE).*

	Red (668)	Green (560)	Blue (475)	Red	Green	Blue	L*	a*	b*	ΔE
N7	**0.42**	**0.43**	**0.43**	**156**	**153**	**161**	63.69	2.64	-3.80	-
M1	0.43	0.40	0.38	143	115	123	51.30	12.33	-0.24	16.13
M2	0.34	0.35	0.30	161	178	194	71.77	-2.50	-10.12	11.47
M4	0.13	0.14	0.14	123	131	137	54.29	-1.67	-4.25	10.35
M9	0.04	0.04	0.05	94	117	139	48.22	-2.82	-14.74	19.72
N6	**0.36**	**0.36**	**0.36**	**151**	**146**	**154**	61.19	3.39	-3.57	-
M1	0.30	0.28	0.27	97	77	88	35.11	10.47	-3.27	27.03
M2	0.24	0.25	0.24	113	126	154	52.69	1.82	-16.61	15.65
M4	0.09	0.10	0.10	85	89	99	37.80	0.72	-6.29	23.70
M9	0.03	0.03	0.04	67	84	103	35.03	-1.44	-13.10	28.26
N4	**0.14**	**0.15**	**0.15**	**99**	**95**	**101**	40.86	2.84	-2.85	-
M1	0.14	0.13	0.13	42	35	40	14.67	4.44	-2.11	26.25
M2	0.12	0.13	0.12	51	58	72	24.31	0.84	-9.56	17.96
M4	0.04	0.05	0.05	37	40	45	16.01	-0.02	-3.73	25.03
M9	0.01	0.01	0.02	28	39	44	14.84	-3.24	-4.84	26.79
N3	**0.10**	**0.10**	**0.10**	**74**	**71**	**75**	30.57	2.13	-1.95	-
M1	0.09	0.08	0.08	26	21	23	7.39	2.93	-0.48	23.24
M2	0.08	0.08	0.08	34	36	45	14.35	1.56	-6.25	16.79
M4	0.03	0.03	0.03	24	24	27	8.36	0.81	-2.10	22.24
M9	0.01	0.01	0.01	17	22	25	6.89	-1.30	-2.83	23.94
TSand	**0.39**	**0.32**	**0.17**	**175**	**145**	**106**	62.00	5.74	24.92	-
M1	0.45	0.33	0.19	150	93	61	45.15	19.97	27.96	22.26
M2	0.42	0.33	0.19	197	166	118	69.79	4.70	29.07	8.89
M4	0.14	0.12	0.08	135	107	70	47.12	6.05	24.91	14.89
M9	0.04	0.03	0.03	107	110	73	45.30	-7.67	20.30	21.91
GSand	**0.35**	**0.36**	**0.09**	**181**	**174**	**159**	71.28	-0.12	8.58	-
M1	0.36	0.30	0.25	119	83	79	39.02	14.44	8.34	35.39
M2	0.33	0.29	0.24	154	149	152	62.20	2.40	-0.93	13.40
M4	0.11	0.10	0.09	104	95	88	40.95	2.28	5.30	30.61
M9	0.03	0.03	0.03	83	100	92	40.78	-8.25	2.38	32.17
MDR	**0.38**	**0.17**	**0.05**	**138**	**76**	**26**	38.98	22.29	39.24	-
M1	0.37	0.13	0.04	124	35	11	28.14	37.40	35.55	18.95
M2	0.35	0.14	0.05	164	67	30	39.22	28.10	40.91	6.05
M4	0.12	0.05	0.02	112	44	17	27.54	28.54	31.24	15.30
M9	0.03	0.01	0.01	88	47	21	24.20	16.25	24.31	21.85
Soil	**0.15**	**0.12**	**0.06**	**96**	**64**	**41**	30.19	11.06	19.61	-
M1	0.19	0.12	0.07	61	30	22	15.37	14.13	12.11	16.89
M2	0.19	0.13	0.08	86	59	49	27.65	10.45	10.95	9.05
M4	0.06	0.04	0.03	56	36	25	16.37	7.92	11.17	16.49
M9	0.02	0.01	0.01	43	37	26	15.01	0.67	8.37	21.55

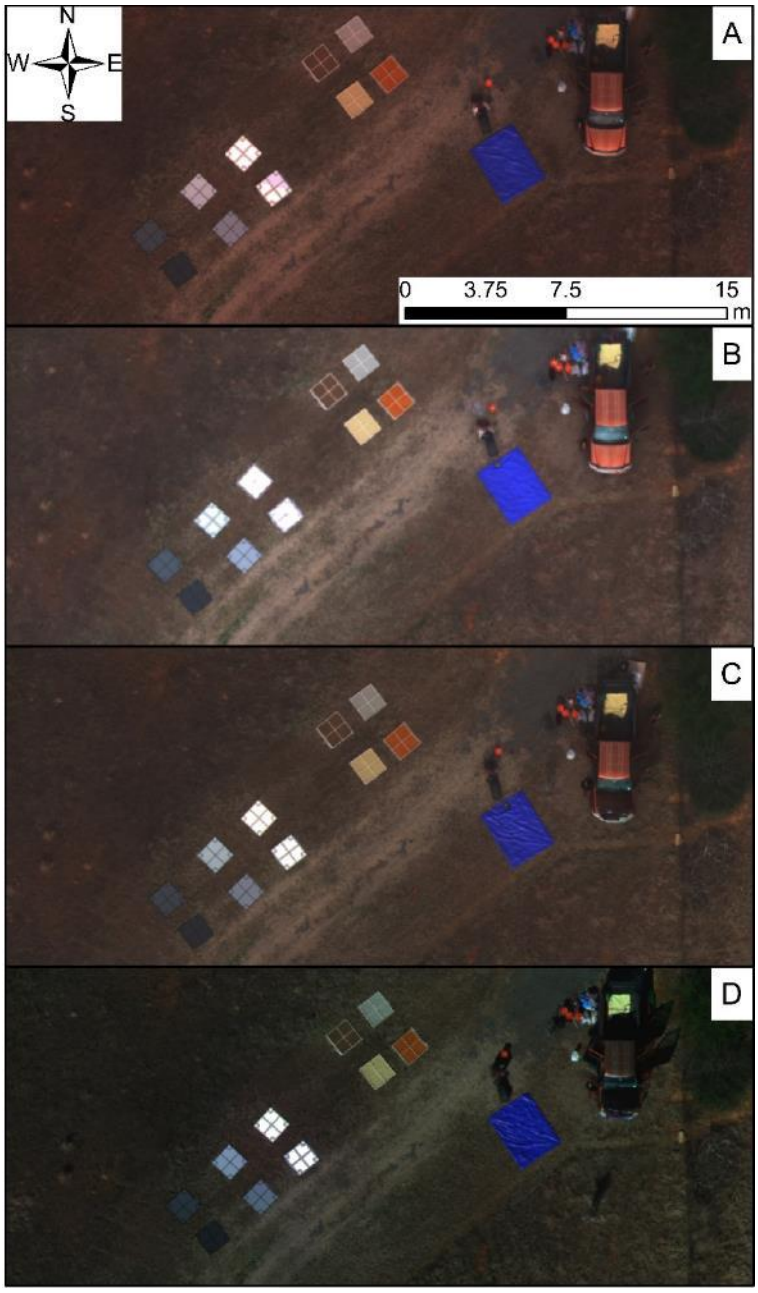

Figure 5.3 Study site RGB composites of representative missions within "sets" where M1, M2, M4, and M9 were represented by (A), (B), (C), and (D), respectively. The first group of panels (northeastern set of four) comprise the natural panels, starting furthest northeast and working clockwise were GSand, MDR, TSand, and Soil, respectively. The calibrated panels (set of six) identified from right to left, north then south; N9, N8, N7, N6, N4, N3. The scale and orientation of (A) was representative of all other images.

5.3.1 Spatial Discrimination

The ground sampling distance (e.g., spatial resolution) of the missions ranged from 3.15 cm pixel^{-1} (M9) to 6.47 cm pixel^{-1} (M3). M2 produced imagery with a spatial resolution of 4.78 cm pixel^{-1}, which typically produced the best representation of the central most pixel in the measurement square. Missions completed at 50 m AGL (e.g., M1 and M4-11) had relatively consistent pixel resolutions (e.g., 3.26 ± 0.08 cm pixel^{-1}). Pixel sizes increased with flight altitude, which also increased pixel mixing and the accurate retrieval of spectra when comparing M2 and M3 (e.g., 75 and 100 m AGL, respectively) (Baltsavias 1999; Mesas-Carrascosa et al. 2015). However, flights completed at lower altitudes had slightly greater pixel reprojection errors compared to the high-altitude flights. Finer resolutions may be desired when studying specific natural environments (e.g., small inland waters). However, as Hsieh et al. (2001) pointed out, these spatial resolutions may not consistently improve data quality. Conversely, if the environment studied was heterogeneous (e.g., urban environments), finer spatial resolutions will be required to discern individual objects (e.g., small buildings) (Small 2003). Although the difference in reprojection error was minor (e.g., 0.042 pixels), this demonstrates one of the tradeoffs between spatial resolution, operation altitude, and data quality.

Furthermore, Figure 5.4 demonstrates the impact mixed pixels had on reflectance from the missions selected from each set. Missions with small pixels (M1 and M4) showed increased responses to borders used in both the calibrated and natural panels. Near the panels' edges (e.g., measurement squares), it appears both borders caused a measurable increase in reflectance when comparing M1 and M2. The mixing of spectra becomes even more problematic if used to

develop statistical models based on the relationship between the assumed pure pixel value and the parameter of interest (e.g., water quality parameters) (Gholizadeh et al. 2016).

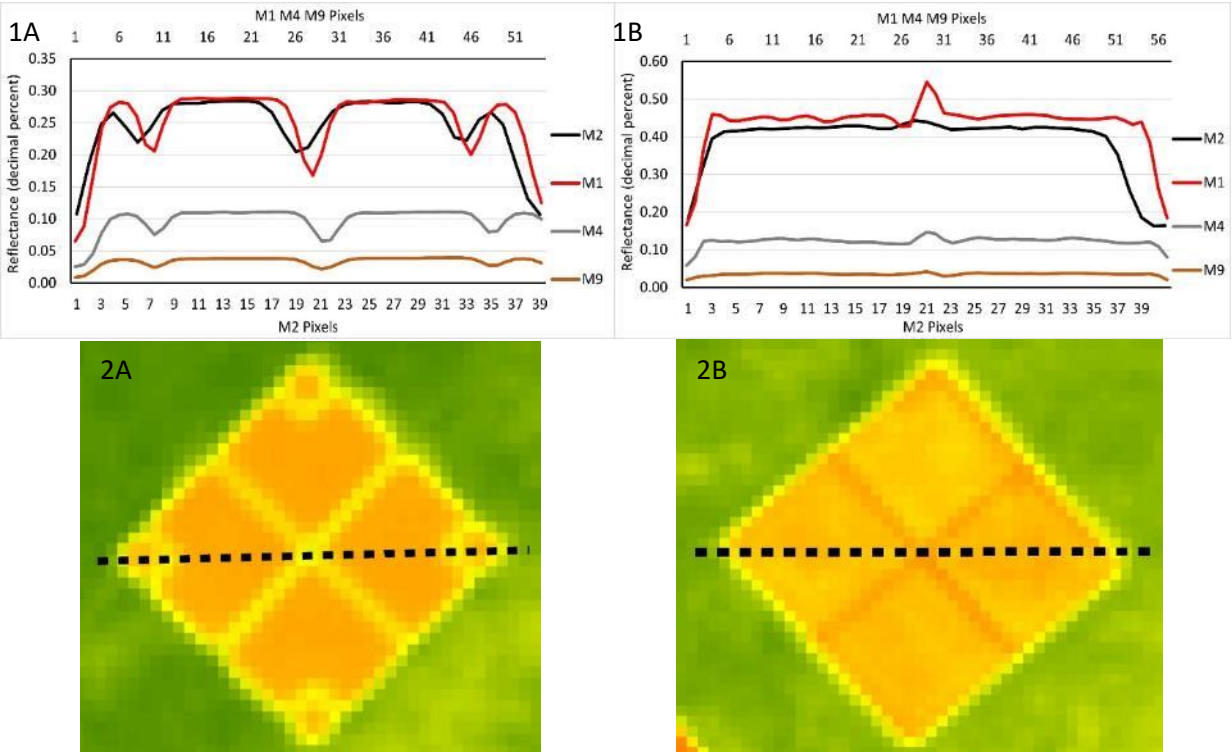

Figure 5.4 Cross sectional profiles from M1, M2, M4 and M9 with M1, M4, and M9 using the upper x-axis and M2 using the lower x-axis (1A and 1B) showing the impact of spectral mixing (e.g., mixed pixels) especially around the edges of the panels and divisions. Examples of extraction (along black dotted line) shown for calibrated panel N6 with blue band reflectance (2A) and natural panel MDR showing red band reflectance (2B) both from M2 clearly demonstrating this phenomenon. Missions with finer spatial resolution produced a more pronounced spectral response than missions with coarser spatial resolution (M2) and less image overlap (M9).

5.3.2 Representation of Color

The fact that image saturation caused issues with two panels in this study was surprising considering the time of year, illumination conditions reported, and the DLS presence. Attempts to reprocess the imagery did not alter the results. Thus, the raw imagery was examined and confirmed image saturation. In the VIS spectrum, the blue and green bands had the widest

bandwidth (e.g., 20 nm), allowing more electromagnetic (EM) energy to enter the RedEdge sensor than the other VIS bands (e.g., red and rededge). These were also the only bands impacted by saturation and only for two panels. Larger bandwidths combined with the level of contrast in the scene (e.g., Munsell N9 to N3) likely produced saturation (Whitehead and Hugenholtz 2014). However, a relatively consistent percentage of pixels were impacted (e.g., 50 to 75 percent) (Figure 5.3) across all missions. Since the eight other panels were seemingly unaffected, panels N9 and N8 were not considered within this study's scope and were removed from further discussion.

LRV calculations provided an assessment of panel lightness (e.g., value) and a metric to confirm that all panels were not affected by image saturation. The manufacturer-provided LRVs (Table 5.1) were all within ten percent of the observed LRVs with N7, N6, N4, N3 different by 9.69, -0.61, -2.04, 1.02 percent, respectively. These calculated LRVs were reasonable considering the other factors (e.g., manufacturing and application) that may have impacted the panel's LRV, confirming the paints were within manufacturer specifications, applied consistently, and not affected by saturation. Saturation is typical throughout environmental remote sensing studies (Huete et al. 1997; Haboudane et al. 2004; Mouw et al. 2015; Zeng et al. 2017) and has been managed by ensuring adequate sensor sensitivity and by simply avoiding bright objects (Wang 2007; Hu et al. 2012; Mouw et al. 2015).

Calculations of ΔE were completed for each mission, and the panels examined. Mouw et al. (2015) allude to the standardization of color products (e.g., NDVI) from post-processing software that should be provided if sUAS technologies achieve widespread implementation. Carrascosa et al. (2015) demonstrated this standardization theory by quantifying how NDVI values were

impacted by sUAS altitude, operation mode, and ground control point settings. However, further standardization was required, particularly of the target object. Thus, to demonstrate how altering mission parameters impact the sensor-perceived color, emphasis was placed on M1, M2, M4, and M9 (Figure 5.5). For all missions and panels examined, there was only one instance M4 outperformed (e.g., produced a lower ΔE value) M2. However, the magnitude of the difference between these missions was minimal compared to the differences between all other panels. Thus, it appears the parameters utilized in M2 produced the most representative panel colors of all other sUAS missions. M2 had an ideal spatial resolution (e.g., 4.78 cm $pixel^{-1}$ in the 15 cm measurement square) minimizing mixed pixels, the lowest mean solar irradiance measured (0.43 $W\ sr^{-1}\ m^{-2}$ (e.g., radiance unit in watt per steradian per square meter)) and the smallest change in solar elevation angle (0.12°) of all missions. Although mixed pixels were minimized, environmental factors outside the control of any study (e.g., solar conditions) substantially impacted the reflectance measured.

Therefore, to allow for comparison of spectra collected under various illumination conditions, both datasets (e.g., panel and sUAS) were further standardized with the CQS tool provided by Davis and Ohno (2005). Under D65 illumination conditions, the ΔE values in Figure 5.5 and Table 5.3 were applied to Equations 3 and 4, providing an assessment of the overall color representation of individual missions across all panels. M2 produced the highest CQS of 73, followed by M4, M1, and M9 with CQS of 53, 47, and 45, respectively. Thus, under the assumed illumination conditions, M2 still produced the most representative spectra across all missions and nearly all panels.

Figure 5.5 $L^*a^*b^*$ colors of Munsell identified reference (Ref.) panels (e.g., N7 - calibrated and Tan Sand (Tsand) - natural) and those produced from M1, M2, M4, and M9 (Test) displaying the calculated color difference (e.g., ΔE) for each of the panels examined.

The need to communicate color in a standardized manner becomes evident with the data presented in Figures 5.6A and 5.6B. These figures represent what was assumed to serve as the spectra referenced by the CAPSURE to produce Munsell color matches, plotted with the sUAS-derived multispectral reflectance pixel values produced by the post-processing software. The magnitude of reflectance corresponds directly to the change in solar azimuth and elevation angles. For example, M1 produced the highest reflectance values, had the smallest change in azimuth angle (1.21°), and the largest positive change in solar elevation angle (0.18°). Surprisingly, M4 produced relatively low reflectance values even though it was performed five minutes after local solar noon and had the slightest absolute change in solar elevation angle (0.03°). These were also likely why M4 produced a slightly more representative color than M2 for panel N7 (Figure 5.5).

To further demonstrate the need for standardization, it appeared the "correct" color identification was more a function of the shape of the spectra (e.g., profile shape) rather than the similarity in relative reflectance (e.g., magnitude of reflectance) (Figures 5.6A and 5.6B). The UCS utilized (e.g., CIE $L^*a^*b^*$) consists of three dimensions. The $L^*a^*b^*$ values acted as coordinates, and if one was substantially different from reference values, the perceived color was modified accordingly. This question of accuracy (e.g., reflectance) versus precision (e.g., $L^*a^*b^*$ colors) should be further examined in the context of using sUAS to describe natural ecosystems. Specifically, this study could be increased in scale to differentiate between missions (e.g., duration and coverage) to truly provide the most efficient set of operational parameters for real-world in-situ environmental monitoring with sUAS.

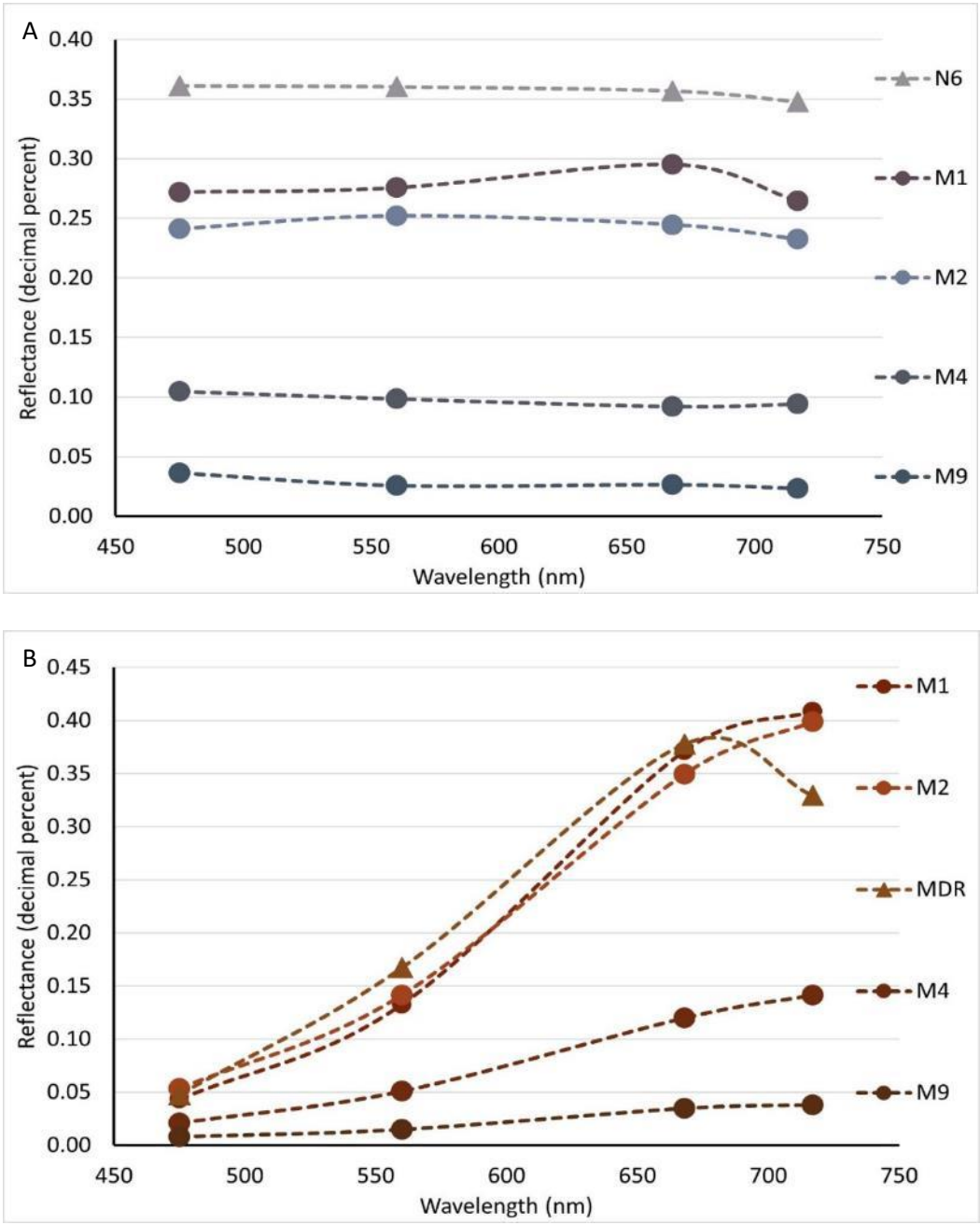

Figure 5.6 CAPSURE reference spectra for Munsell N6 (N6) (A) and Munsell 5YR 4/8 (MDR) (B) and sUAS-derived reflectance values produced from various missions (e.g., M1, M2, M4 and M9) at calibrated panel N6 (A) and natural panel MDR (B) with colors symbolized from extracted sRGB values from each mission.

5.3.3 sUAS Operational Performance

Therefore, to demonstrate a scaled version of the suggested future work, linear relationships between various mission parameters and ΔE values were developed, and simple efficiency metrics were explored. Efficiency metrics were established by assuming a study area of approximately 400,000 m^2 and applying some post-mission characteristics (e.g., flight time, required disk space, and percentage of battery consumed). The increased area provided a more apparent differentiation between parameters that were otherwise identical throughout the study (Table 5.4). M3 was the most efficient in terms of post-mission characteristics, taking approximately 80 minutes and half the next mission's storage space. Nevertheless, flight altitude heavily impacted these metrics, which was the highest (e.g., 100 m) for M3. M2 was second in terms of disk space required and ranked fourth among all missions for coverage time and battery consumption percentage (e.g., tradeoffs). The differences in efficiency between M1 (rank two) and M2 (rank four) were minimal (e.g., 15 minutes for coverage and 2.73 percent battery consumption) relative to the perceived color differences (Figure 5.5). To further demonstrate how this difference in efficiency was negligible, the linear relationships between all mission parameters and ΔE values were examined. Results of this simple exercise revealed two parameters that could describe greater than 60 percent of the variability (e.g., coefficient of determination (R^2)) in ΔE values. Both parameters have been discussed at length and were lowest for M2. These two parameters (e.g., solar elevation angles and downwelling solar irradiance) accounted for errors in color perception (ΔE values) with moderate confidence (e.g., R^2 = 0.63 and 0.61, respectively).

Table 5.4 Missions ranked by efficiency metrics from lowest to highest for each metric; developed using post-mission parameters and an assumed study area of 100 ac.

Mission	Coverage Time (min)	Mission	Storage Required (MB)	Mission	Battery Consumed (%)
M3	178	M3	8307	M3	10.00
M1	263	M2	17087	M1	11.17
M9	270	M8	20543	M7	13.33
M2	278	M6	37948	M2	13.89
M4	327	M5	38950	M5	15.78
M5	332	M9	39127	M4	17.18
M10	336	M4	45083	M9	18.03
M6	340	M1	45257	M6	19.14
M11	352	M11	45400	M10	19.46
M7	360	M7	45667	M8	20.27
M8	541	M10	65772	M11	24.64

5.4 Conclusions

Overall, this study identified the need to develop and test a standard operational procedure for environmental remote sensing via sUAS. Due to the variability in sUAS, a method for developing calibrated target objects to identify sUAS-specific mission parameters was presented. Assessment of manufacturer mission recommendations suggested the focus should shift to different operational parameters. In terms of precision, the mission (M2) with the most appropriate spatial resolution, lowest mean solar irradiance measured, and smallest change in solar angles produced the most accurate representation of color when all panels were considered. Straightforward linear relationships were developed that demonstrated changes in solar conditions throughout operations that could describe approximately 60 percent of the color identification error. In terms of tradeoffs between efficiency and precision, the most efficient mission (M3), although identified color more precisely on one occasion, the magnitude of error in all other instances was so large efficiency could be sacrificed for the level of relative precision

achieved. Clearly, a balance exists and must be further established between sUAS operational parameters, data precision, and efficiently achieving the study's goal. For environmental remote sensing with sUAS to become established, the equilibrium between all these factors must be maintained for any hope in addressing the need for widespread monitoring and evaluation of terrestrial and aquatic ecosystems worldwide.

Literature Cited

Baltsavias E. (1999) A comparison between photogrammetry and laser scanning. *ISPRS Journal of Photogrammetry and Remote Sensing,* 54(2-3): 83 -94. https://doi.org/10.1016/S0924-2716(99)00014-3.

Biber E (2013) The challenge of collecting and using environmental monitoring data. Ecology and Society 18(4):68. https://dx.doi.org/10.5751/ES-06117-180468.

ColorMine. (2014) Color Converter. https://www.nuget.org/packages/ColorMine/. (accessed 10 March 2021).

Davis W, Ohno Y. (2005) Toward an improved color rending metric. In: Ferguson I, Carrano J, Tsunemasa T, Ashdown, I (eds.) Proceedings Of the Fifth International Conference on Solid-State Lighting. Bellingham, Washington. https://doi.org/10.1117/12.615388.

Gholizadeh M, Melesse A, Reddi L. (2016) A comprehensive remote on water quality parameter estimation using remote sensing techniques. *Sensors,* 16(8): 1298 – 1341. https://doi.org/10.3390/s16081298.

Haboudane D, Miller J, Pattey E, Zarco-Tejada P, Strachan I. (2004) Hyperspectral vegetation indices and novel algorithms for predicting green LAI of crop canopies: modeling and validation in the context of precision agriculture. *Remote Sensing of Environment,* 90(3): 337 – 352. https://doi.org/10.1016/j.rse.2003.12.013.

Holzbauer-Schweitzer B, Nairn R. (2020) Spectral monitoring techniques for optically deep mine waters. In: Pope J, Wolkersdorfer C, Sartz L, Weber A, Woldersdorfer K.: Mine Water

Solutions. 110 – 117 p, Christchurch, New Zealand (International Mine Water Association).

Hsieh P, Lee L, Chen N. (2001) Effect of spatial resolution on classification errors of pure and mixed pixels in remote sensing. *IEEE Transactions on Geoscience and Remote Sensing*, 39(12): 2657-2663. https://doi.org/10.1109-36.975000.

Hu C, Feng L, Lee Z, Davis C, Mannino A, McClain C, Franz B. (2012) Dynamic range and sensitivity requirements of satellite ocean color sensors: learning from the past. *Applied Optics,* 51(25): 6045 – 6062. https://doi.org/10.1364/AO.51.006045.

Huete A, Liu H, Leeuwn W. (1997) Use of vegetation indices in forested regions: issues of linearity and saturation. In: Stein T (ed) 1997 International Geoscience and Remote Sensing Symposium. Singapore. https://doi.org/10.1109/GARSS.1991.609169.

Liu Y, Islam MA, Gao J. (2003) Quantification of shall water quality parameters by means of remote sensing. *Progress in Physical Geography*, https://doi.10.1191/0309133303pp357ra.

Mamaghani B, Salvaggio C. (2019) Multispectral sensor calibration and characterization for sUAS remote sensing. *Sensors,* 19(20): 4453 -

Mamaghani B, Saudners M, Salvaggio C. (2019) Inherent reflectance variability of vegetation. *Agriculture,* 9(11):246 - 270. https://doi.org/10.3390/agriculture3110246.

Martin P, Payton O, Fardoulis J, Richards D, Scott T. (2015) The use of unmanned aerial systems for the mapping of legacy uranium mines. *Journal of Environmental Radioactivity,* 143: 135-140. https://doi.org/10.1016/j.envrad.2015.02.004.

Mesas-Carrascosa F J, Torres-Sánchez J, Clavero-Rumbao I, García-Ferrer A, Peña J, Borra-Serrano I, López-Granados F. (2015) Assessing optimal flight parameters for generating accurate multispectral orthomosaicks by UAV to support site-specific crop management. *Remote Sensing,* 7(10) 12793 – 12814. https://doi.org/10.3390/rs71012793.

MicaSense. (2021) Best practices: collecting data with micasense sensors. https://support.micasense.com/hc/en-us/articles/224893167. (accessed 19 March 2021).

Mokrzycki W, Tatol M. (2011) Color difference delta E – a survey. *Machine Graphics and Vision,* 20(4): 383 – 411.

Mouw C, Greb S, Aurin D, Digiacomo P, Lee Z, Twardowski M, Binding C, Hu C, Ma R, Moore T, Moses W, Craig S. (2015) Aquatic color radiometry remote sensing of coastal and inland waters: challenges and recommendations for future satellite missions. *Remote Sensing of Environment,* 160: 15-30. https://doi.org/10.1016/j.rse.2015.02.001.

National Oceanic and Atmospheric Administration (NOAA), Global Monitoring Laboratory (GML). (2021) NOAA Solar Calculator. https://www.esrl.noaa.gov/gmd/grad/solcalc/ (accessed 19 March 2021).

Park S, Choi Y. (2020) Applications of unmanned aerial vehicles in mining from exploration to reclamation: a review. *Minerals,* 10(8): 663-694. https://doi.org/10.3390/min10080663.

Peter B, Messina J, Carrol J, Zhi J, Chimonyo V, Lin S, Snapp S. (2020) Multi-spatial resolution satellite and sUAS imagery for precision agriculture on smallholder farms in Malawi. *Photogrammetric Engineering and Remote Sensing*, 86(2):107-119. https://doi.org/10.14358/PERS.86.2.107.

Poppiel R, Coelho Lacera M, Rizzo R, Safanelli J, Bonfatti B, Silvero N, Demattê J. (2020) Soil color and mineralogy mapping using proximal and remote sensing in midwest Brazil. *Remote Sensing,* 12(7): 1197 – 1227. https://doi.org/10.3390/rs12071197.

Ranquist E, Steiner M, Argrow B. (2016) Exploring the range of weather impacts on UAS operations. *Proceedings of the 97th Annual American Meteorological Society Annual Meetings*. Seattle, Washington (AMS).

Ridd M. (1994) Exploring a V-I-S (vegetation-impervious surface-soil) model for urban ecosystem analysis through remote sensing: comparative anatomy for cities. *International Journal of Remote Sensing,* 16(12): 2165-2185. https://doi.org/10.1080/01431169508954549.

Rossel R, Minasny B, Roudier P, McBratney A. (2006) Colour space models for soil science. *Geoderma,* 133(3-4): 320 – 337. https://doi.org/10.1016/j.geoderma.2005.07.017.

Shah A, Deshmukh B, Sinha L.K. (2020) A review of approaches for water depth estimation with multispectral data. *World Water Policy,* 6(1): 152-167. https://doi.org/10.1002/wwp2.120029.

Small C. (2003) High spatial resolution spectral mixture analysis of urban reflectance. *Remote Sensing of Environment*, 88(1-2): 170-186. https://doi.org//10.1016/j.rse.2003.04.008.

Tang Z, Nairn R. (2021) Mine drainage residual additions to lake sediments alter phosphorus and trace metal distributions. *Water, Air, and Soil Pollution,* 232(52): 51 – 64. https://doi.org/10.1007/s11270-021-05016-3.

Torrent J, Barrón V. (2002) Diffuse reflectance spectroscopy of iron oxides. *Encyclopedia of Surface and Colloid Science* (1): 1438-1446.

Wang M. (2007) Remote sensing of the ocean contributions from ultraviolet to near-infrared using the shortwave infrared bands: simulations. *Applied Optics,* 46(9): 1535 – 1547. https://doi.org/10.1364/AO.46.001535.

Whitehead K, Hugenholtz C. (2014) Remote sensing of the environment with small unmanned aircraft systems (UASs), part 1: review of progress and challenges. *Journal of Unmanned Vehicle Systems,* 2:69-85. https://doi.org/10.1139/juvs-2014-0006.

X-Rite. (2021A) Munsell Neutral Value Gray Scales. https://munsell.com/color-products/color-standards/munsell-neutral-value-gray-scales/. (accessed 10 March 2021).

X-Rite. (2021B) CAPSURE RM200. https://www.xrite.com/categories/portable-spectrophotometers/capsure-rm200?utm_source=google&utm_medium=cpc&utm_campaign=03-GO-NA-EN-DSA&utm_content=DSA_Spectrophotometers&utm_term=&matchtype=b&device=c. (accessed 19 March 2021).

Zeng C, Richardson M, King D. (2017) The impacts of environmental variables on water reflectance measured using a lightweight unmanned aerial vehicle (UAV)-based spectrometer system. *ISPRS Journal of Photogrammetry and Remote Sensing,* 130: 217-230. https://doi.org/10.1016/j.isprsjprs.2017.06.004.

Chapter 6: Conclusions

The focus of this doctoral research was to describe shallow optically complex inland waters in terms of the relationships between observed in-situ water quality and small Unoccupied Aerial System (UAS)-derived multispectral reflectance. The goal was to develop and expand on the understanding of the light and water surface interactions to demonstrate and promote the environmental application of sUAS technologies for monitoring and evaluating complex aquatic environments. The need to quantify the benefits of sUAS technologies over traditional remote sensing methods (e.g., satellites) and to develop innovative tools to assist in monitoring complex inland waters, while identifying the technological, operational, and applicational limitations, served as motivation.

Overall, the accurate retrieval of data for traditional optically active constituents (OACs) (e.g., chlorophyll-a) in inland optically shallow waters (OSWs) is still out of reach when using a turn-key sUAS and various statistical modeling, reflectance extraction, and data transformation techniques. However, a novel multispectral imagery post-processing technique slightly improved the accuracy and precision of water quality retrieval models in inland OSWs. These model improvements suggest a simple exercise with several assumptions, and minimal ancillary data collection efforts, can improve statistically derived surface water quality models (Chapter 2).

Furthermore, exploiting physical relationships (e.g., sorption) between various mine water contaminants produced strong linear relationships ($R^2_{adj.} > 0.74$) with high confidence and allowed for the estimation of non-optical (i.e., those that did not contribute to the measured spectra) metals. When using site-specific spectra and in-situ water quality, estimates of in-situ metal concentrations were within one percent of the observed value for most parameters

examined (e.g., Fe, Li, Mn, Pb, and Zn). In the studied mine drainage passive treatment systems (PTS), the dominant optical parameter (iron-oxyhydroxides – particulate Fe) was readily estimated with models developed and validated in waters of different geologic origin. However, in optically deep waters (ODWs) impacted by mine drainage, site-specific spectra produced the most representative relationships for all other metals analyzed. The derivation of a robust exponential relationship (R = 0.73) between sUAS-derived red band reflectance and the Secchi disk depth (SDD) and actual depth (AD) ratio will assist in identifying OSWs and other remote sensing interferences in mine drainage PTS (Chapter 3).

To further understand the interactions between OACs, the impact of aquatic optical depth (OD) on remotely sensed spectra, and to determine if sUAS imagery can describe these optically complex systems, mesocosm-scale systems were studied. The shift in scale allowed for a more detailed examination of these impacts and resulted in spectra more accurately estimating OACs in ODWs compared to OSWs. sUAS-derived imagery not only assisted in identifying OSWs but could discern the effects of reflectance from the substrate on spectra collected from mesocosm-scale systems (Chapter 4).

Examining impacts on the spectra measured by altering specific flight parameters on an autonomously operated sUAS was of particular interest. Such a study provided a basis for the integration of sUAS into traditional environmental monitoring practices. Significant trade-offs existed between sUAS data quality, the operational parameters used to collect the data, and the solar conditions throughout operations. Unsurprisingly, increases in mission efficiency (e.g., decreased flight duration) proportionally decreased the sUAS-derived multispectral imagery accuracy and quality. Additionally, changes in solar conditions throughout the missions

accounted for approximately 60 percent of the spectral measurements' error. With the countless platforms and sensors currently available, the development of a standard operating procedure for environmental monitoring via sUAS must consider all platforms and sensors available, or evaluate and define which should be employed. Further efforts should also identify operational limitations and conditions, target object-specific variability, and the tradeoffs between sUAS mission efficiency and the quality of the data collected (Chapter 5).

Currently, sUAS technologies are far from replacing traditional in-situ monitoring. Due to the variability in accuracy, along with the lack of standardized sUAS operating procedures and reporting criteria, these technologies should only be used as exploratory tools. If integrated into regular monitoring activities, environmental monitors could use these technologies to identify *hotspots* at much finer temporal and spatial scales than conventional monitoring, which could substantially decrease the amount of time, money, human-hours, and laboratory analyses required to sufficiently characterize the extent of environmental issues. This dissertation also expands on the current OACs that can be estimated remotely and demonstrates the benefits of incorporating sUAS technologies into traditional environmental monitoring efforts. However, a balance exists and must be further established between sUAS operational parameters, data precision, and efficiently achieving the study's goal. For environmental remote sensing with sUAS to become widely established, the equilibrium between all these factors must be maintained for any hope in addressing the need for monitoring and evaluation of terrestrial and aquatic ecosystems worldwide. Together the chapters in this dissertation provide insight into the capabilities and limitations of remote monitoring with sUAS in optically complex inland waters.

Appendix: Data Availability

The information in Table A.1 summarizes the data used to complete this dissertation that is available from the author upon request.

Table A.1 Data available upon request from author used to complete the studies included in this dissertation; small Unoccupied Aerial System (sUAS); Multispectral (MS); Chlorophyll-a (Chl-a); Total Suspended Solids (TSS); Secchi Disk Depth (SDD); Dissolved Oxygen (DO); Specific Conductance (Sp. Cond.); MissionPlanner Waypoint File Format (.WP); Tag Image File Format (.TIFF); Georeferenced Tag Image File Format (.GEOTIFF); Microsoft Excel File Format (.XLS); Text File Format (.TXT).

Dissertation Chapter	Data Type	Parameters	Format
Chapter 2			
	sUAS Mission Plans/Flight Logs	Operational Characteristics	.WP
	Unprocessed sUAS images	Digital Number	.TIFF
	Processed sUAS MS imagery	Relative Reflectance	.GEOTIFF
	In-situ water quality	Chl-a; TSS; SDD; Turbidity; DO; pH; Sp. Cond.	.XLS
Chapter 3			
	sUAS Mission Plans/Flight Logs	Operational Characteristics	.WP
	Unprocessed sUAS images	Digital Number	.TIFF
	Processed sUAS MSimagery	Relative Reflectance	.GEOTIFF
	In-situ water quality	Total and dissolved metals; Turbidity; SDD: DO; pH; Sp. Cond.	.XLS
Chapter 4			
	sUAS Mission Plans/Flight Logs	Operational Characteristics	.WP
	Unprocessed sUAS images	Digital Number	.TIFF
	Processed sUAS MSimagery	Relative Reflectance	.GEOTIFF
	In-situ water quality	Chl-a; TSS; SDD; Turbidity; Total and dissolved metals; Color; Alkalinity; DO; pH; Sp. Cond.	.XLS
Chapter 5			
	sUAS Mission Plans/Flight Logs	Operational Characteristics	.WP
	Unprocessed sUAS images	Digital Number	.TIFF
	Processed sUAS MSimagery	Relative Reflectance	.GEOTIFF
	Down dwelling irradiance	Solar Irradiance	.TXT
	Colorimetric measurements	Munsell Colors	.XLS